

**Alma Mater Studiorum – Università di Bologna**

**DOTTORATO DI RICERCA IN**

**MECCANICA E SCIENZE AVANZATE  
DELL'INGEGNERIA**

**Ciclo XXX**

**Settore Concorsuale di afferenza: 09/A3**

**Settore Scientifico disciplinare: ING-IND/14**

**ANALYSIS OF DRILLING OF COMPOSITE LAMINATES**

**Presentata da: NAVID ZARIF KARIMI**

**Coordinatore Dottorato**

**Prof. Marco Carricato**

**Supervisore**

**Prof. Giangiacomo  
Minak**

**Esame finale anno 2018**

## **DECLARATION**

I hereby declare that except where specific reference is made to the work of others, the contents of this dissertation are original and have not been submitted in whole or in part for consideration for any other degree or qualification in this, or any other university. This dissertation is my own work and contains nothing which is the outcome of work done in collaboration with others, except as specified in the text and acknowledgements.

Navid Zarif Karimi

December 2017

*To my wife who has always support me during the past three years of my doctoral journey.*

*To my parents for their endless support and encouragement and for making it all worthwhile.*

## ACKNOWLEDGEMENTS

I would like to extend my special thanks and appreciation to Professor *Giangiacomo Minak*, my academic advisor during the doctoral study period. His personal interest, patience, guidance and support helped refine the ideas presented in this thesis and provided me with rewarding academic and research experience. He has been very supportive and caring, not only in regard to my academic progress, but also about many other issues that I was involved with besides my Ph.D. study.

Many thanks to the reviewers for agreeing to serve on my committee. Their thoughtful evaluation, constructive suggestions, and criticism were helpful in keeping this work on purpose.

I wish to extend my sincere thanks to Dr. *Hossein Heidary* for his assistance in refining the ideas for this research and close involvement in expediting my research activities. Many of my accomplishments would not have been realized without his help.

I am most grateful to Professor *Michael Wisnom*, director of the advanced composite centre for innovation and science, for inviting me as a visiting researcher at University of Bristol. I also would like to extend gratitude to Dr. *Mohamad Fotouhi* and Dr. *Meisam Jalalvand* for their support during this period.

I would also like to thank Mr. *Paolo Proli* for his technical advice and assistance in accessing resources, material preparation and testing. Assistance of Mr. *Ruggero Maria Vittori* throughout the experimental work is appreciated.

My special appreciation goes to my parents; their faith in me has been and will always be my drive to excel. This doctoral degree is a manifestation of many years of ambition and sacrifice that my parents have undergone for me to achieve; without their tender loving care and support, my education in Italy would not have been possible. I owe them everything and wish I could show them just how much I love and appreciate them.

Above all, my deep appreciation and love goes to my wife, *Parnian Kianfar*. She has been devoted herself full time to support me during the last three years. She is the single person who has experienced the greatest hardship during this period, even so she has cheered me on when I was discouraged. I would like to thank her for being patient and firm, a pillar of strength and moral support throughout, often more determined than I.

## SOMMARIO

I materiali compositi avanzati sono caratterizzati dalla combinazione di alte rigidezza e resistenza specifiche. Di conseguenza i compositi hanno attirato un'attenzione crescente per varie applicazioni industriali. L'espansione dell'utilizzo di materiali compositi richiede l'impiego di differenti tipologie di lavorazione di macchina utensile. Una delle più comuni è la foratura, usata per favorire l'assemblaggio di sotto componenti in composito. Lo scarto di parti in composito allo stadio del montaggio a causa della scarsa qualità dei fori che presentano danni indotti dalla foratura è una seria preoccupazione per le industrie manifatturiere. Non è né pratico né economico interrompere il processo di foratura per controllare eventuali danni, perciò c'è grande necessità di un controllo continuo senza interruzione del processo. Questa Tesi affronta il problema della caratterizzazione, della modellazione e del controllo continuo del processo di foratura attraverso differenti metodologie sperimentali e analitiche.

Sono stati sviluppati modelli analitici che predicono la spinta critica e l'avanzamento critico, valori oltre i quali la delaminazione inizia a propagare durante la foratura di compositi multidimensionali. L'area delaminata è stata modellata come una piastra circolare con i bordi incastriati e soggetta a differenti profili di carico in corrispondenza dei taglienti e della punta del trapano. Utilizzando la meccanica della frattura e la teoria classica dei laminati sono state ottenute delle espressioni analitiche per la spinta critica e l'avanzamento in differenti posizioni della lamina. Una strategia ad avanzamento variabile  $p$  stata suggerita al fine di ridurre la delaminazione in maniera da ottimizzare i tempi di foratura. I modelli proposti sono stati verificati sperimentalmente e paragonati con i modelli disponibili in letteratura. I valori predetti dal modello mostrano un accordo soddisfacente con quelli misurati. Si è visto che i nuovi modelli forniscono risultati più accurati dei precedenti.

La qualità dei fori ed il danno indotto dal processo di foratura di laminate composite è stato studiato sperimentalmente. L'influenza dei parametri di foratura, della geometria dell'utensile e del materiale da forare è stata studiata attraverso misurazione e esami qualitativi. Molti indici di qualità della foratura sono stati misurati, come la forza di spinta, l'area delaminata, la resistenza residua a compressione e a flessione. L'effetto dei parametri principali di foratura su questi indici è stato analizzato statisticamente e sono state identificate le condizioni ottimali di foratura per avere ottime prestazioni e fori non danneggiati. I risultati sperimentali hanno mostrato che la scelta delle condizioni di foratura è critica per le prestazioni del foro, specialmente nel caso di materiali con funzione strutturale.

Inoltre, è stato eseguito studio sperimentale basato sulle Emissioni Acustiche come strumento di controllo in linea e di valutazione non distruttiva della foratura dei compositi. Le Emissioni Acustiche sono state usate per esaminare la relazione tra segnale di risposta e danno da foratura. Diverse quantità caratteristiche delle EA sono state misurate, tra cui ampiezza, frequenza media, energia, conteggi, tempo di salita e durata del segnale. È stata presentata una procedura per la discriminazione e l'identificazione di differenti meccanismi di danneggiamento che è basata su

differenti sistemi di acquisizione e analisi del segnale. I risultati hanno consentito di determinare lo spettro e il contenuto energetico dei meccanismi di danneggiamento più importanti durante la foratura. Infine si è concluso che le Emissioni Acustiche hanno un grande potenziale per il controllo in linea e la caratterizzazione del danno da foratura.

**Parole Chiave:** Foratura, Laminati Compositi, Delaminazione, Modellazione Analitica, Controllo mediante Emissioni Acustiche.

## ABSTRACT

Advanced composite materials are characterized by having a combination of high specific strength and stiffness. As a result of these remarkable properties, composites have attracted increasing attention for use in many industries. The application expansion of composite materials calls for the use of different types of machining operations; of which drilling is one of the most commonly used processes in the assembly of composite sub-components. Rejection of composite parts at the assembly stage due to the poor-quality hole with drilling induced damages is a serious concern for manufacturing industries. It is neither practical nor economical to interrupt the drilling process and inspect these damages; therefore, there is a great need for online monitoring method without interrupting the process. This dissertation deals with the characterization, modeling, and monitoring of drilling process of composite materials through various experimental and analytical investigations.

Analytical models were developed which predicts critical thrust force and critical feed rate above which the delamination crack begins to propagate in the drilling of multi-directional laminated composites. The delamination zone was modeled as a circular plate, with clamped edge and subjected to different load profiles for cutting lips and chisel edge regions. Based on fracture mechanics, classical laminate theory and orthogonal cutting mechanics, expressions were obtained for critical thrusts and critical feed rates at different ply locations. A variable feed rate strategy was then suggested with the aim of avoiding delamination while drilling in a time-optimal fashion. The proposed models have been verified by experiments and compared with the existing models. Based on the results, the predicted values by the proposed models show satisfactory agreement with the experimentally measured values. It was found that the new developed models provide more accurate and rigorous results than the formers.

Quality of holes and drilling-induced damage when drilling fiber reinforced composite laminates were experimentally studied. The influence of drilling parameters, tool geometry, and workpiece material on the resulting quality of the produced hole and damage were studied through qualitative measurements and examinations. Several quality responses were measured as indices of drilling performance, including thrust force, delamination size, residual compression strength, and residual flexural strength. Effects of key drilling parameters on these responses were statistically analyzed, and optimal drilling conditions for high performance and free-damage drilling were identified. Experimental results revealed that the choice of drilling conditions is critical to hole performance especially when these materials are subjected to structural loads.

An experimental study of acoustic emission as a tool for in-process monitoring and nondestructive evaluation of drilling of composites was conducted. Acoustic emission was used to examine the relationship between signal response and drilling induced damages. A number of AE features were measured to characterize the process, including amplitude, average frequency, energy, counts, rise time, and duration of the signals. A procedure for discrimination and identification of different damage mechanisms was presented utilizing different signal acquisition systems and signal

analysis tools. Based on the results, frequency distribution and energy percentage of most important damage mechanisms occurring during drilling were determined. Finally, it was concluded that acoustic emission has a great potential for the application of online monitoring and damage characterization in the drilling of composite structures.

**Keywords:** Drilling, Laminated Composites, Delamination, Analytical Modeling, Acoustic Emission Monitoring

# Table of Contents

<b>ACKNOWLEDGEMENTS.....</b>	<b>v</b>
<b>SOMMARIO .....</b>	<b>vi</b>
<b>ABSTRACT .....</b>	<b>viii</b>
<b>List of Figures.....</b>	<b>xiii</b>
<b>List of Tables .....</b>	<b>xvi</b>
<b>Nomenclature.....</b>	<b>xviii</b>
<b>1 INTRODUCTION .....</b>	<b>1</b>
1.1    Composite materials .....	1
1.2    Problem statement .....	3
1.3    Motivation and research objectives .....	4
1.4    State of the work.....	5
<b>2 ANALYSIS OF DELAMINATION .....</b>	<b>7</b>
2.1    Delamination mechanism.....	7
2.1.1    Delamination at the hole entry .....	8
2.1.2    Delamination on the hole exit .....	9
2.2    Supported and unsupported drilling.....	9
2.3    Factors affecting delamination .....	12
2.4    Assessment of delamination.....	15
2.5    Modeling delamination propagation.....	17
2.5.1    Analytical model for push-out delamination.....	19
2.5.2    Analytical model for peel-up delamination .....	21
2.5.3    Analytical model for orthotropic materials.....	21
2.6    Drilling thrust force and torque .....	22
2.6.1    Influence of drilling parameters on thrust and torque .....	23
2.7    Approaches to prevent delamination .....	27
2.7.1    Back-up plate .....	27
2.7.2    Special drill bits.....	28
2.7.3    Pre-drilled pilot holes .....	29
2.7.4    Variable feed rate strategy .....	29

2.7.5	Two-side drilling.....	30
2.7.6	High speed drilling.....	30
2.8	Delamination and residual mechanical properties.....	31
<b>3</b>	<b>ANALYTICAL ANALYSIS .....</b>	<b>32</b>
3.1	Cutting force models for drilling.....	32
3.1.1	Formulation of cutting force model.....	33
3.2	Analytical model for delamination propagation.....	37
3.2.1	Physical model .....	37
3.2.2	Loading models.....	39
3.3	Experimental validation and comparison with existing models.....	48
<b>4</b>	<b>EXPERIMENTAL PROCEDURE.....</b>	<b>51</b>
4.1	Material preparation .....	51
4.1.1	GFRP composites.....	51
4.1.2	Nano filled GFRP composites.....	51
4.2	Experimental setup .....	52
4.2.1	Drilling tests.....	52
4.2.2	Drill tools.....	53
4.2.3	Drilling fixture .....	53
4.2.4	Drilling force measurement .....	54
4.2.5	Post-drilling mechanical test.....	55
4.2.6	Microstructure observation .....	56
4.2.7	Acoustic emission measurement .....	56
4.3	Plan of experiments .....	57
4.3.1	Full factorial design.....	57
4.3.2	Taguchi method.....	57
4.4	Statistical analysis methods .....	59
4.4.1	Analysis of variance .....	59
4.4.2	Taguchi S/N ratio analysis.....	59
4.4.3	Multi-objective optimization: Grey relational analysis .....	60
<b>5</b>	<b>Analysis, Results and Discussion .....</b>	<b>62</b>
5.1	Thrust force .....	62

5.2	Delamination.....	67
5.3	Effects of drilling parameters on mechanical strength .....	72
5.3.1	Residual compression strength.....	72
5.3.2	Residual flexural strength.....	77
<b>6</b>	<b>ACOUSTIC EMISSION MONITORING .....</b>	<b>85</b>
6.1	Historical background.....	85
6.2	Theoretical considerations .....	86
6.3	Evaluation of acoustic emission signals .....	86
6.4	Application to monitor machining of composites .....	88
6.5	Literature review .....	88
6.6	Clustering methodology.....	90
6.6.1	Fuzzy c-means clustering.....	90
6.6.2	Principal component analysis.....	93
6.6.3	Wavelet Analysis.....	95
6.7	Damage characterization.....	96
6.7.1	Multivariable analysis of AE data.....	96
6.7.2	Wavelet-based methodology for AE analysis.....	101
<b>7</b>	<b>CONCLUSIONS AND FUTURE WORK .....</b>	<b>106</b>
7.1	Conclusions.....	106
7.2	Recommendations for future works.....	108
<b>Bibliography .....</b>	<b>109</b>	
<b>List of Publications .....</b>	<b>119</b>	
International Journals .....	119	
Conferences .....	119	
<b>Appendix A: Calculating reduced bending stiffness matrix .....</b>	<b>121</b>	
<b>Appendix B: Solution of the governing equation for circular plates .....</b>	<b>122</b>	

## List of Figures

Figure 1.1. Schematic representation of common drilling induced damage.....	3
Figure 2.1. SEM images of delamination; (a) intersection image of GFRP, and (b) surface image of CFRP [5].....	7
Figure 2.2. Schematic of peel-up delamination at the hole entry side in drilling of laminated composites.....	8
Figure 2.3. Schematic of push-out delamination on the hole exit in drilling of laminated composites.....	9
Figure 2.4. Schematics of supported and unsupported drilling [7] .....	10
Figure 2.5. Thrust force and cutting torque in supported and unsupported drilling [7] .....	11
Figure 2.6. Graph of relative drill point-workpiece speed during unsupported drilling [7] .....	11
Figure 2.7. Mechanism of indentation during unsupported drilling [7] .....	11
Figure 2.8. Schematic of the measurement of the delaminated area $Ad$ and the maximum diameter $D_{max}$ .....	15
Figure 2.9. Critical cases when drilling FRP laminates; (a) fine cracks, and (b) uniform damage area [35] .....	16
Figure 2.10. Circular plate model for delamination analysis [50].....	20
Figure 2.11. Schematic shape of the delamination zone in a unidirectional laminate [44].....	21
Figure 2.12. forces when drilling composite laminates using a back-up plate.....	28
Figure 2.13. Different drill bits; (a) standard twist drill, (b) candle stick drill, (c) multifaceted drill, (d) straight flute drill. ....	29
Figure 2.14. Drilling hole in a pre-drilled laminate.....	29
Figure 2.15. Variable feed rate strategy for delamination free drilling; staircase type and a continuous variation of feed rate along the depth of workpiece .....	30
Figure 3.1. Cutting forces in orthogonal and oblique models.....	34
Figure 3.2. The nomenclature of the twist drill features.....	34
Figure 3.3. The forces exerted on main cutting lip and the drilling rake angle. ....	36
Figure 3.4. Axisymmetric circular plate subjected to rotationally axisymmetric loads. ....	39
Figure 3.5. Concentrated central load model for delamination analysis. ....	40
Figure 3.6. Correlation between critical feed rate and uncut depth under drill tool. ....	42
Figure 3.7. Equivalent uniformly distributed load model for delamination analysis.....	42

Figure 3.8. Uniformly distributed loads model for delamination analysis.....	45
Figure 3.9. Equivalent loading system of Figure 3.8 .....	45
Figure 3.10. Effect of chisel edge radius on critical thrust force predicted by Eq. (3.58a).....	48
Figure 3.11. Critical thrust force, $F_{th}$ , varying with the ply number, $n$ , from the bottom side..	50
Figure 4.1. Experimental setup of drilling.....	53
Figure 4.2. HSS twist drill bit used in the experiments.....	53
Figure 4.3. Fixture of experimental drilling tests.....	54
Figure 4.4. Measurement of drilling thrust force.....	54
Figure 4.5. Schematic of test specimen and instrumentation for compression test.....	55
Figure 4.6. Schematic of experimental setup for three-point bending test on dilled specimens...	56
Figure 4.7. Acoustic emission monitoring during the drilling process. ....	57
Figure 5.1. Load versus displacement in static test (a) flat cylindrical indenter [113] (b) conical indenter [114, 115]. .....	63
Figure 5.2. The thrust force plot during drilling at feed rate of $f = 63$ mm/min and spindle speed of $S = 630$ rpm. ....	64
Figure 5.3. SEM images showing (a) matrix cracking and delamination during entry stage and (b) fiber failure during cutting stage.....	64
Figure 5.4. Contribution percent of input variables on thrust force.....	66
Figure 5.5. Main effects plot for S/N ratios of thrust force. ....	67
Figure 5.6. Measurement of the delaminated area ( $A_d$ ) of specimens at the exit side. ....	68
Figure 5.7. Pareto chart of process parameters for delamination factor.....	69
Figure 5.8. Main effects plot for S/N ratios of delamination factor.....	70
Figure 5.9. The interaction plots for mean values of measured delamination factors.....	71
Figure 5.10. Positive linear relationship between thrust force and adjusted delamination factor.	71
Figure 5.11. A typical specimen during compression test.....	72
Figure 5.12. Residual compressive strength for different drilling conditions vs. (a) displacement, (b) delamination factor.....	73
Figure 5.13. Main effects plot for residual compressive strength.....	74
Figure 5.14. Residual plots for residual compressive strength. ....	75
Figure 5.15. Plots of standardized residuals versus (a) feed rate, (b) spindle speed.....	76

Figure 5.16. (a) The interaction plot and, (b) the contour plot of the residual compressive strength.....	76
Figure 5.17. The response surface of the polynomial regression model for residual compressive strength.....	77
Figure 5.18. A typical drilled specimen during the bending test. ....	78
Figure 5.19. Contribution percent of input variables on residual flexural strength. ....	79
Figure 5.20. Main effects plot for S/N ratios of residual flexural strength.....	80
Figure 5.21. Response graph for the grey relational grade. ....	83
Figure 6.1. The two typical types of acoustic emission signals; Continuous emission and Burst emission. ....	86
Figure 6.2. The definitions for a typical acoustic emission signal during drilling process. ....	87
Figure 6.3. Fuzzy c-means clustering algorithm. ....	93
Figure 6.4. Wavelet packet transform tree.....	96
Figure 6.5. The percent of the total variability explained by each principal component. ....	97
Figure 6.6. Clustering procedure of AE signals collected during drilling process. ....	98
Figure 6.7. PCA visualization of the fuzzy c-means clustering. ....	98
Figure 6.8. Time-based features of AE signals collected during drilling process; Cumulative count, Mean power, amplitude, cumulative energy, RMS, average frequency. ....	99
Figure 6.9. Thrust force and AE amplitude variation versus time in drilling process. ....	99
Figure 6.10. Regenerated amplitude distribution after first classification.....	100
Figure 6.11. Regenerated amplitude distribution after second classification. ....	100
Figure 6.12. Energy percentage of each component of level 3, energy (%) vs. waveform number. ....	102
Figure 6.13. FFT of the decomposed components of level 3, FFT amplitude ( $\text{mV}^2/\text{Hz}$ ) vs. frequency (Hz).....	103
Figure 6.14. SEM images showing (a) matrix cracking and delamination during entry stage and (b) fiber failure during cutting stage.....	104

## List of Tables

Table 2.1. Empirical models for delamination factor in drilling fiber reinforced plastics .....	13
Table 2.2. Analytical models for predicting critical thrust force at the onset of delamination in drilling process .....	18
Table 2.3. Empirical models for thrust force in drilling FRPs.....	25
Table 3.1. Material properties of 914/T300 carbon/epoxy composite laminate.....	49
Table 3.2. Variation of critical thrust force with ply number.....	50
Table 4.1. Properties of matrix and fibers used for GFRP composites .....	51
Table 4.2. Properties of functionalized multi-walled carbon nanotubes .....	52
Table 4.3. Specification of the drill bits used in the experiments .....	53
Table 4.4. Factors and levels selected for drilling of compression specimens .....	57
Table 4.5. Factors and levels selected for drilling of bending specimens .....	58
Table 4.6. The L <sub>16</sub> orthogonal array layout.....	58
Table 5.1. Measured experimental results for thrust force .....	65
Table 5.2. Analysis of variance table for thrust force .....	66
Table 5.3. Response table for signal to noise ratios for thrust force .....	67
Table 5.4. Measured experimental results for delamination factor.....	68
Table 5.5. Analysis of variance table for delamination factor .....	69
Table 5.6. Response table for signal to noise ratios for delamination factor.....	70
Table 5.7. The design matrix and measured experimental results .....	73
Table 5.8. Analysis of variance for residual compressive strength .....	74
Table 5.9. The L <sub>16</sub> orthogonal array layout and measured experimental results .....	78
Table 5.10. Analysis of variance table for residual flexural strength.....	79
Table 5.11. Response table for signal to noise ratios for residual flexural strength .....	80
Table 5.12. Data preprocessing of the experimental results, the reference sequence is 1.....	81
Table 5.13. The calculated grey relational coefficient, grey relational grade, and the corresponding order.....	82
Table 5.14. Response table for grey relational grade .....	83
Table 5.15. Results of drilling performances using the initial and optimal machining parameters.	84

Table 6.1. Frequency range and energy percentage for eight components of level 3 ..... 103

## Nomenclature

$A_0$	Nominal hole area
$A_d$	Delaminated area
$A_{\max}$	Maximum area of delamination zone
$a$	Crack radius
$D$	Bending rigidity
$D'$	Effective bending rigidity
$D_0$	Nominal hole diameter
$D_{\max}$	Maximum diameter of delamination zone
$E$	Modulus of elasticity
$F_d$	Delamination factor
$F_{da}$	Adjusted delamination factor
$F_h$	Projection of force on drill axis
$F_{hu}$	Horizontal force
$F_{vu}$	Vertical force
$F_A^*$	Critical thrust force
$F_P^*$	Critical peeling force
$f$	Feed rate
$G$	Geometrical parameter
$G_{IC}$	Critical strain energy release rate in mode I
$h$	Uncut thickness
$h_d$	Cutting depth
$H$	Plate thickness
$i$	Inclination angle
$K_n$	Specific energy for vertical force
$K_{n,chisel}$	Specific energy at chisel edge
$k_p$	Peeling factor
$N$	Spindle speed

$n$	Number of plies
$q$	Uniform distributed load
$q_L$	Uniform distributed load exerted on cutting lips
$q_C$	Uniform distributed load exerted on chisel edge
$R$	Nominal drill radius
$r$	Radial coordinate
$r_c$	Chisel edge radius
$F_{th}$	Thrust force
$F_{th}^L$	Thrust force exerted on cutting lips
$F_{th}^C$	Thrust force exerted on chisel edge
$T_{exp}$	Experimental thrust force
$t$	Cutting depth
$t_c$	Half the thickness of the chisel edge
$U$	Stored strain energy
$U_d$	Strain energy absorbed by crack growth
$V_c$	Cutting speed
$W$	Work done
$w$	Deflection of plate
$\gamma$	Rake angle
$\gamma_c$	Chisel edge rake angle
$\gamma_d$	Dynamic portion of rake angle
$\gamma_m$	Average rake angle
$\gamma_s$	Static portion of rake angle
$\varepsilon$	Drill point angle
$\rho$	Normalized radius
$\varphi$	Chisel edge angle
$\psi$	Helix angle

# CHAPTER 1

## 1 INTRODUCTION

As composite materials become more and more popular, a growing emphasis is placed on manufacturing and fabricating them better, cheaper and faster. Several non-traditional machining processes such as laser cutting, water-jet cutting, ultrasonic cutting, electro-discharge machining, etc. have been developed to machine the composite materials. However, conventional machining processes such as drilling continue to be widely in use. When compared to conventional metallic materials, drilling composites pose additional difficulty due to their unique nature, microscopical inhomogeneity, anisotropy and laminate structure. Therefore, it is important to push the existing technologies to the limit so as to optimally exploit them as well as to develop more advanced drilling processes for composites. The present study embodies both of these aspects.

First part of this chapter discusses composite materials, their applications, fabrication methods, and the problems associated with machining of them. In the second part, the motivations, objectives, and organization of the dissertation are described.

### 1.1 Composite materials

Composite materials are multi-phase materials obtained through the artificial combination of different materials in order to attain properties that the individual components by themselves cannot attain. In contrast to metallic alloys, each material retains its separate chemical, physical, and mechanical properties. The primary reason for using composite materials is their high strength and stiffness, combined with low density, when compared with conventional engineering materials. Additionally, by deliberately designing the constituent materials, their proportions, and the orientation of each ply in the laminate, one can tailor material properties to fit specific needs.

Composite materials are usually composed of a reinforcing material embedded in a base material. In most cases, the reinforcement is harder, stronger, and stiffer than the base phase, hence it provides the key structural properties of the material; high specific strength and modulus. The reinforcing phase is typically in the form of particulates or fibers. Particulate composites tend to be weaker and less stiff than fibrous composites, but they are usually cheaper [1] .

#### *Fibers*

The primary function of the fibers is to carry the loads along their longitudinal directions. Generally, fibers are classified into two division by fiber length; continuous fibers, and short fibers. Continuous fiber composites normally have a preferred orientation, while discontinuous or short fiber composites generally have a random orientation. Continuous fiber composites are used where higher strength and stiffness are required, at a higher cost, and discontinuous fiber composites are used where cost is the main driver and strength and stiffness are less important. Examples of

continuous reinforcements include unidirectional, woven, and helical winding. While examples of short reinforcements are chopped fibers and random mat.

Although a wide variety of fiber materials are available today, carbon fiber reinforced polymers (CFRPs) and glass fiber reinforced polymers (GFRPs) are by far the most common fiber reinforced composites in many industries in view of their specific mechanical properties. Glass fiber reinforced polymers have comparatively lower cost to carbon base composites results in more applications of GFRPs. Carbon fiber reinforced polymers are relatively expensive construction materials and therefore used when their properties of lightness and strength are of paramount importance, such as aerospace applications.

### ***Matrix***

The base phase is the matrix that performs three main functions; to hold the fibers in the proper orientation and spacing, to distribute the load between the fibers, and to protect the fibers from abrasion and the environment. In order to fulfill these tasks, an ideal matrix material should possess the following properties; it should initially be a low-viscosity liquid that is converted to a tough durable solid, it should wet the fibers and form a strong interface, and it should exhibit a high shear strength. The matrix can be a polymer, metal, or ceramic. Polymers have low strength and stiffness, metals have intermediate strength and stiffness while high ductility, and ceramics have high strength and stiffness but are brittle.

Polymer-matrix composites offer very high strength-to-weight and stiffness-to-weight ratios, and the aerospace industry is making a major effort to incorporate an increasing number of fiber reinforced polymer (FRP) laminates into various components and structures. Among polymers used for structural composites, epoxy is being used extensively which is also utilized in the current work. It has the advantageous of non-volatility, good thermal and dimensional stability, and high bond strength.

### ***Applications***

Most fiber reinforced polymers for structural use are laminated. FRP laminates can be tailored for various properties by appropriately choosing their components, their proportions, their distributions, their morphologies, their degrees of crystallinity, crystallographic textures, as well as the structure and composition of the interface between components. Owing to this strong tailorability, composite laminates can be designed to satisfy the needs of technologies relating to the aerospace, automobile, electronics, construction, energy, biomedical and other industries. As a result, composite materials constitute most commercial engineering materials.

### ***Fabrication and manufacturing process***

As FRPs have gained great importance in various applications, several processing techniques have been developed to fabricate them with a uniform fiber distribution and high degree of alignment. Each process has its own usefulness for combining different kinds and amounts of fibers and resins. The basic processes can be categorized into two classes: open mould and closed mould processes.

The open mould processes include hand lay-up, spray-up, vacuum pressure bag, autoclave, filament winding and continuous pultrusion. Closed mould processes include matched die moulding, injection moulding and resin transfer moulding [2].

## 1.2 Problem statement

### ***Machining metals and composites***

Although a near-net shape can be obtained in the production of components made of fiber-reinforced polymer laminates, machining processes are still required for dimensional accuracy, surface finishing and assembly with other parts [3]. The machining characteristics of composites are different from that of metals, which are well established and standardized on validated machining practices and quality requirements. Machining of composites is one of the most difficult and least understood areas in advanced manufacturing science. Poor machined quality will result in poor assembly tolerance, poor finish quality, and long-term performance deterioration.

### ***Drilling process and challenges***

Among the machining processes, drilling is the most frequently applied for composites due to the need for fastening in mechanical structures [4]. For bolted joints and assemblies, damage-free and precise holes must be drilled in the components to ensure high joint strength and precision. Furthermore, repairs in the field often require the drilling of holes in composite laminates. The great difference between the drilling of conventional materials, basically metals, and the drilling of composite materials lies in the very unlike nature of material. Composite materials are anisotropic, locally inhomogeneous, and are mostly prepared in laminate form before they undergo the drilling process. Due to anisotropy and inhomogeneity, metal cutting techniques have to be modified considerably when applied to composite materials to avoid creating drilling induced damage, which is the subject of the current work. A schematic representation of common drilling induced damage during drilling of FRP composite laminates is shown in Figure 1.1.

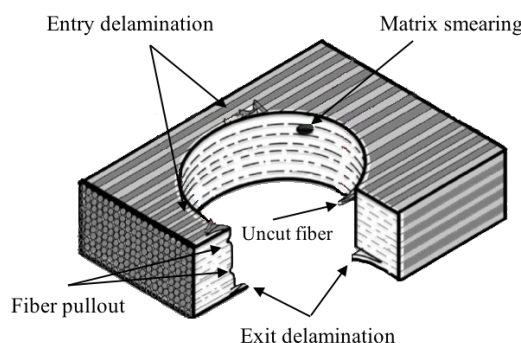


Figure 1.1. Schematic representation of common drilling induced damage.

### ***Delamination***

The typical damage encountered during the drilling of composite laminates consists of delamination of layers due to the relatively poor strength of these materials in the thickness

direction. Such damage is generally initiated when the drilling force exceeds a threshold value at critical stages. The presence of delamination reduces the stiffness and strength of a laminate and thus degrades its load carrying capacity. Delamination can often be the limiting factor in the use of composite laminates for structural applications, particularly when subjected to compression, bending and fatigue loads and when exposed to moisture and other aggressive environments over a long period of time. As delamination is so detrimental, an attempt should be made to avoid delamination in the first place.

### **1.3 Motivation and research objectives**

The drilling of FRP composite laminates is a relatively new practice, and unlike the well-established practices of metal drilling, it is still in the development stages. Regardless of the fact that ample research work has been published in the past years, many issues associated with drilling of composite materials still need further examination. The lack of comprehensive theoretical and empirical investigations is the primary motivation for this thesis study. Such investigations will provide a platform for high performance and productivity machining which is an interesting subject for manufacturing industries.

The objective of this dissertation is to study some of the challenges encountered in the production of good quality hole when drilling fiber reinforced composite laminates, and to develop a theoretical model with the goal of avoiding delamination. This model should provide reasonable correlation between cutting condition, material properties, and the occurrences of delamination. The interactions between cutting parameters, such as feed rate and cutting speed, and cutting force should be also illustrated. Additionally, residual properties of drilled composite laminates is desired. The evolution of delamination and its effect on the residual properties of drilled composite laminates requires extensive investigation. Several complimentary mechanical tests are conducted for this purpose. Last but not the least, online monitoring the drilling process is desired. Acoustic emissions of composite materials during drilling are collected for this purpose. In summary, the specific objectives of the thesis are:

- 1. Investigation on drilling performance of composite laminates**

A parametric study of drilling composite laminates is the primary objective of this thesis to identify optimum tool and process parameters for high performance drilling. In this study, a large number of experiments will be conducted to explore the influence of different input parameters such as spindle speed, feed rate, drill bit geometry and materials on output parameters such as drilling thrust force, delamination, and residual strength. The relationship between drilling induced damages and drilling conditions and parameters will be investigated experimentally. Additionally, a series of damage tolerance tests will be performed to investigate the influence of drilling induced damages on residual strength of laminates.

- 2. Developing an analytical model for delamination propagation**

Laminated fiber reinforced composites under cutting forces are subject to the risk of interlaminar crack propagation, or delamination, which threatens structural reliability. Such damage imposes a limiting factor to the machinability of composites and need new tools of analysis; therefore, is a major damage mechanism to be predicted. The present study will provide an analytical model using classical plate theory and linear elastic fracture mechanics to predict the critical cutting force and feed rate responsible for the onset of the delamination.

### 3. Online detection and monitoring of drilling process

Rejection of composites parts at the assembly stage due to poor quality hole with drilling induced damages is a serious concern for manufacturing industries. It is neither practical nor economical to interrupt the drilling process and inspect these damages; therefore, there is a great need for online monitoring method without interrupting the process. This study will address a new approach utilizing acoustic emission technique together with signal processing method to examine the relationship between signal response and drilling induced damages.

## 1.4 State of the work

The present study attempts to address some problems associated with the drilling of fiber-reinforced composite laminates and to solve those problems. It consists of analytical investigations as well as their experimental verifications. The following paragraphs provide an overview of the content of each chapter in the manuscript.

Chapter 1 discusses briefly what fiber-reinforced composite laminates are and how such materials are manufactured. It is then followed by a statement of the issues associated with machining and particularly drilling of composite materials, research motivations and objectives, and thesis outline.

Chapter 2 states the problem of delamination which composite materials exhibit during conventional machining processes. The mechanisms of the formation delamination cracks, factors affecting delamination, visualization and assessment techniques, and approaches to prevent delamination propagation are addressed. Additionally, primary analytical models for delamination mechanisms based on the theory of fracture mechanics are presented. It also includes a review of the state-of-the-art in the machinability of holes in composite laminates, incorporating a discussion of the drilling process and quality criteria currently applied to composites.

Chapter 3 describes the theories of orthogonal and oblique cutting and the mechanics of drilling operation. A modeling of the formation of delamination cracks using linear elastic fracture mechanics and classical laminated theory is then presented. Theoretical models for thrust force and feed rate are developed for a variety of loading conditions. These models are able to predict the critical values for thrust force and feed rate at the onset of delamination as a function of material properties, tool geometries, and specimen configuration. The validity of the model is confirmed experimentally.

Chapter 4 is concerned with the experimental procedure. Workpiece material preparation, experimental setups, machine tools, test procedures, and measurement techniques are covered in this chapter. Methods employed to design the experiments, selection of input factors, corresponding levels, their ranges, and selection of the quality responses are outlined. Furthermore, statistical and analytical methods used to analyze the experimental data on the hole quality responses are described.

In Chapter 5, experimental investigations on the drilling thrust force, delamination and residual properties of the drilled specimens are carried out. The effects of cutting parameters and tool geometry as well as material properties are evaluated and discussed in details.

Chapter 6 explores the feasibility of using acoustic emission (AE) in monitoring the drilling of composite materials. It is demonstrated that AE shows a promising potential for the application of online monitoring and damage characterization. Furthermore, signal processing is expected to promote the effectiveness of the technique.

Finally, in Chapter 8, the results are summarized and specific conclusions are drawn. Recommendations for the future research in this area are also given.

# CHAPTER 2

## 2 ANALYSIS OF DELAMINATION

The principal mode of failure of composite laminates is the separation along the interfaces of the layers, which is called delamination. In layered composites, the adjacent layers are bonded together by a thin layer of resin between them. The interface layer transfers the force from one layer to another one. If this interface weakens or damages, it causes the adjacent layers to separate. Delamination is induced by interlaminar tension and shear that develops because of various factors including free edge effects, structural discontinuities, localized disturbances during manufacturing and in working condition, such as impact of falling objects, drilling operation, moisture and temperature variations and internal failure mechanisms like matrix cracking.

Hidden from superficial visual inspection, delamination usually lies buried between the layers, and began to propagate in response to an appropriate mode of loading. Delamination drastically reduces the strength and stiffness and thus limits the life of the structure. Moreover, it causes stress concentration in load bearing plies and a local instability which leads to a further growth of interlaminar cracks, resulting in a compressive failure of the laminate. Hence, delamination is known as the most prevalent life-limiting damage growth mode.

In this chapter, the mechanisms of the formation delamination cracks, factors affecting, assessment of delamination, methods to avoid delamination propagation, and some basic theoretical models for delamination onset are described.

### 2.1 Delamination mechanism

Drilling induced delamination has been recognized as a major concern in machining of fiber reinforced polymer laminates because it may adversely affect the structural integrity and long-term reliability of the machined component. Figure 2.1 shows several scanning electron microscopy (SEM) images of delamination damage.

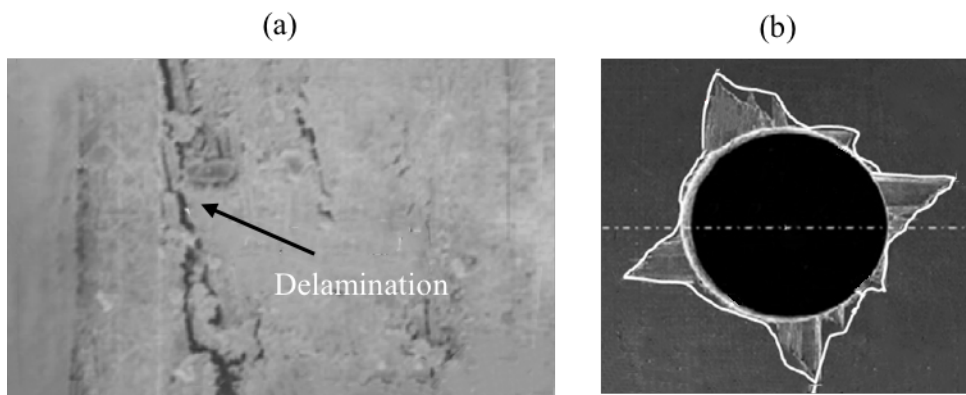


Figure 2.1. SEM images of delamination; (a) intersection image of GFRP, and (b) surface image of CFRP [5].

By design, each composite lamina possesses large strength and modulus along the fiber direction and low strength and stiffness in the transverse direction. As per strength requirements, several of these laminas or plies should be stacked together to possess large in-plane strength, but their out-of-plane strength is very poor. Depending on the tool geometry, material being drilled, machining parameters (such as feed rate and spindle speed), a thrust force, axial component of cutting forces, is developed during the drilling operation. This transverse thrust force is responsible for the occurrence of delamination during drilling.

El-Sonbaty *et al.* [6] identified two forms of delamination called “peel-up” at the drill entry point and “push-out” on the exit side of the workpiece. In practice, it has been found that the delamination associated with push-out is more severe than that associated with peel-up. The mechanisms of delamination at the entry and exit of the drilled holes periphery are discussed in the following sections.

### 2.1.1 Delamination at the hole entry

Delamination at the drill entry hole is called peel-up which is shown schematically in Figure 2.2. At the very beginning of drilling, the cutting edge of the drill abrades the laminate. It then, by moving forward, tends to pull the abraded material away along the flutes. The material spirals up before it is machined completely, see Figure 2.2. This spiraling action implies a peeling force upwards, which is responsible for separating the upper laminates from the uncut portion held by the compressively acting thrust force. Such peeling force results from a tensile stress filed near the cutting edge, which is produced by the cutting action. This phenomenon has been reported in the study of metal cutting, which discusses the opening of micro-cracks and separation of materials beneath the tool edge. As a result, the cutting force, which abrades the laminate, is actually what drives the structure to delaminate. The transformation from the peripheral cutting force to the axial peeling force is a complex function of drill geometry and friction between the tool and workpiece. Further work is needed to investigate this transfer function.

The first ply is most vulnerable to delamination since it has the weakest back-up support against bending. Peel-up delamination becomes progressively more difficult as drilling proceeds since the thickness resisting the lamina bending becomes greater.

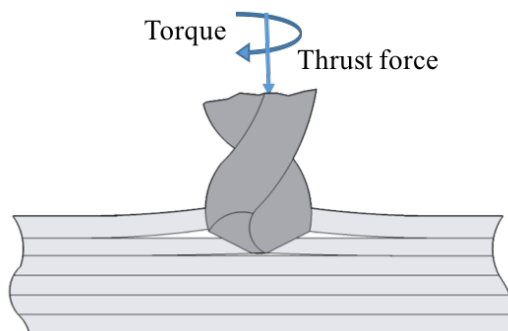


Figure 2.2. Schematic of peel-up delamination at the hole entry side in drilling of laminated composites.

### 2.1.2 Delamination on the hole exit

Push-out is the delamination mechanism occurring as the drill reaches the exit side of the material, where the uncut thickness is smaller and the resistance to deformation decreases. In drilling, the drill always exerts a compressive thrust force on the workpiece. In the case of composites, the laminae under the drill are subjected to bending deformation and tend to be pushed away from the interlaminar bond around the machined hole. As the drill approaches the exit, the uncut thickness becomes smaller and the resistance to deformation decreases. At a critical thickness, the interlaminar bond fails by the action of thrust force and an interlaminar crack is initiated around the hole. Further pushing down by the drill point causes the crack to propagate and the flexural rigidity of the supporting plies becomes weaker. This leads to fracturing the material below the drill point as the chisel edge proceed exiting the laminate. The fracture of the bottom surface plies occurs by both Mode I and Mode III fracture.

The last lamina is most frequently found delaminated within the laminate since it is the weakest in resisting bending deformation. Delamination often happens before the laminate is completely penetrated by the drill, as shown in Figure 2.3, leaving a damaged zone around the hole.

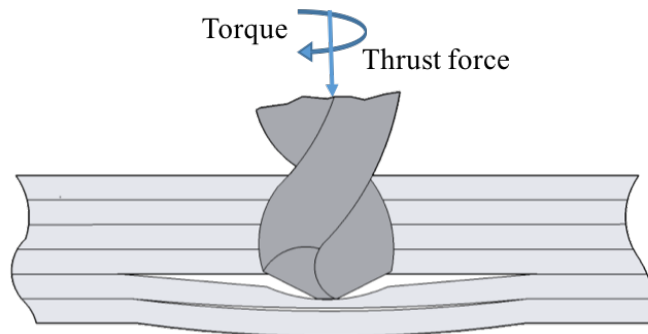
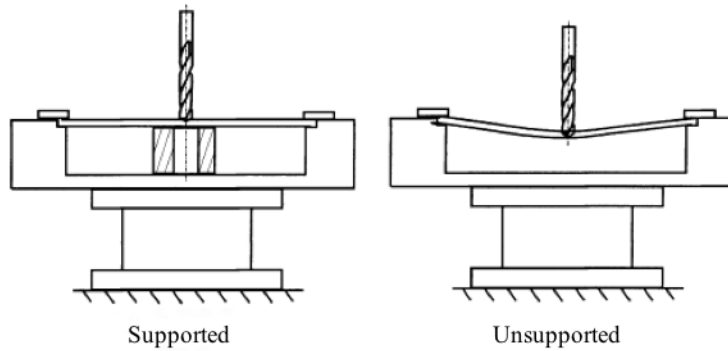


Figure 2.3. Schematic of push-out delamination on the hole exit in drilling of laminated composites.

## 2.2 Supported and unsupported drilling

The mechanism of delamination during unsupported drilling is completely different from that above is described for supported drilling. In supported drilling, a sacrificial plate or a support plate which is usually pre-drilled is placed under the workpiece. However, in unsupported drilling, there is nothing under the workpiece, hence it is free to bend due to the applied thrust force. Figure 2.4 depicts a schematic of supported and unsupported drilling.

For the better understanding of the delamination mechanism, it is helpful to analyze and compare these two drilling cases. For this purpose, the graphs of the drilling thrust force and torque as a function of the drill bit displacement are shown in Figure 2.5. The analyses of the graphs are given in the following paragraphs.



*Figure 2.4. Schematics of supported and unsupported drilling [7].*

During supported drilling, the thrust force increases drastically at the beginning of the process, as the chisel edge of the drill penetrates the laminate. The torque increases more slowly due to the smaller cutting forces at the chisel edge and the proximity of these forces to the center of the drill. The torque starts to increase as the cutting edges engage in cutting the laminate. The axial force increases with the entrance of the cutting lips and then oscillates around a constant mean value until delamination occurs. The thrust force and torque decrease rapidly as the drill emerges out of the laminate. The thrust force reaches zero when the drill bit fully emerges out of the laminate but the torque reaches a nonzero value as the flutes of the drill are still engaged in the workpiece.

Unlink supported drilling, during unsupported drilling, the thrust force increases gradually as the workpiece begins to bend under the advancing drill bit, making the relative speed between drill and workpiece low. In fact, the actual feed rate is considerably lower than the nominal feed rate, and the overall progress of the drill tool in the laminate becomes slow. As the drill bit approaches the last uncut plies, the stress due to the thrust force exceeds its critical value and all the uncut materials are burst open. At this stage, the deflected workpiece is released and it regains its initial straight position, causing the actual feed rate increases rapidly. Figure 2.6. clearly reveals the sudden increase in the relative workpiece-drill bit speed. Moreover, the cutting torque graph shows a peak in correspondence of this phenomenon.

The thrust force has been cited as the main cause of delamination by several researchers and it is believed that higher thrust force introduces more extensive delamination to the workpiece. However, Capello [7] showed that this is not always true when drilling composite laminates. In fact, during unsupported drilling, the thrust force is smaller than in supported drilling, while the delamination is more extensive. This suggests that in unsupported drilling a different mechanism is in play and other factors should be considered.

In unsupported drilling, the actual feed rate increases from very low values at the beginning of cutting process to very high during the release movement. By increasing the feed rate, the time required for cutting operation and chip formation decreases, and instead of cutting, the drill bit penetrates the laminate by punching, which obviously cause more delamination to propagate. When the feed rate becomes high enough, the whole drill point acts as a punch on the laminate

which leads to a higher tendency for delamination. Figure 2.7 depicts how the increase in feed rate changes the cutting mechanism of the drill bit.

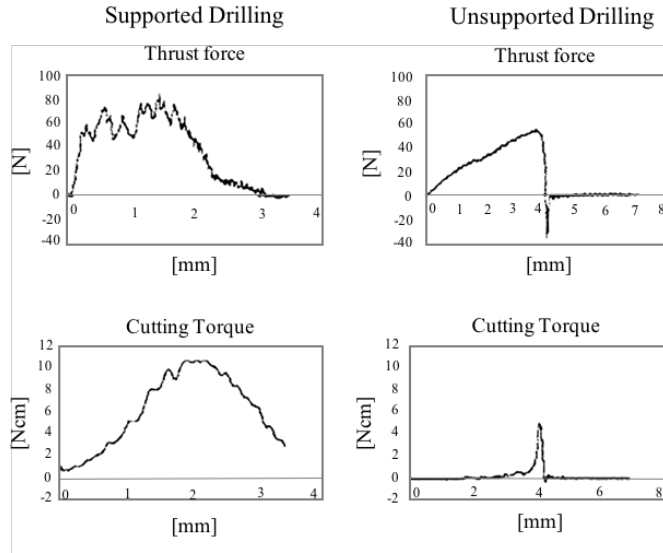


Figure 2.5. Thrust force and cutting torque in supported and unsupported drilling [7].

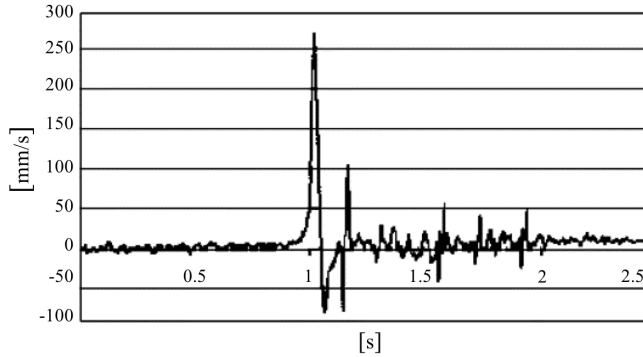


Figure 2.6. Graph of relative drill point-workpiece speed during unsupported drilling [7].

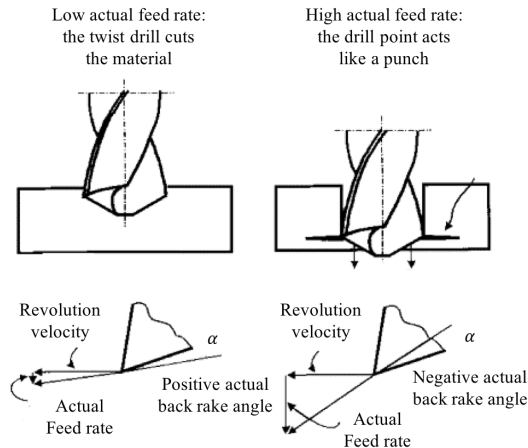


Figure 2.7. Mechanism of indentation during unsupported drilling [7].

### 2.3 Factors affecting delamination

The onset of delamination and the extent of damage are influenced by several factors including feed rate, spindle speed, drill geometry, and material properties. In order to reduce delamination, it is necessary to develop procedures to select appropriate cutting parameters, because an unsuitable choice could lead to unacceptable material degradation.

Several researchers investigated the effects of input variables, feed rate, cutting speed, point angle of twist drill bit, etc. on drilling induced delamination. Most studies show that feed rate is the most influential parameter to control delamination as it directly affects the thrust force [8-13]. Davim and Reis *et al.* [14, 15] conducted a series of experiments on different composite materials including GFRPs, CFRPs, and metal matrix composites to understand the effects of drilling parameters on delamination and other characteristics of these materials. Their results show that delamination increases with increasing feed rate and cutting speed. The effect of feed rate on delamination is more than that of the cutting speed. In contrast, the works conducted by Khashaba *et al.* [13, 16], Karnik *et al.* [17], and Rubio *et al.* [18], show that delamination decreases with increasing cutting speed during drilling of woven-ply GFRP composite laminates. Gaitonde *et al.* [11, 17] also reported that delamination decreases with cutting speed during high-speed drilling of thin woven-ply CFRP composite laminates. They also observed that delamination increases with increasing drill point angle. By contrast, Kilickap [19] observed that the delamination tendency decreases with increasing point angle of twist drill during conventional drilling of UD-ply GFRP composite laminates. To summarize, almost all researchers reported that drilling induced delamination increases with increasing feed rate at any different cutting speeds using various drill bits, while two different behavior for cutting speed and drill point angle effects were reported.

A number of empirical models has been presented for several drill geometries to relate the delamination factor and drilling parameters. Table 2.1 gives a summary of these models. These models show the influences of feed rate, drilling speed, drill diameter, and drill type on delamination damage. Statistical analysis of the experimental results pointed out that feed rate has the greatest statistical and physical significance on delamination damage, followed by cutting speed. Additionally, the type of drill bit plays a key role in introduction of delamination. The Brad and Spur carbide drill causes the lowest delamination damage around the hole, which is followed by the helical flute carbide drill, the straight flute carbide drill, and the high-speed steel (HSS) twist drill. The reason is that delamination is closely dependent on thrust force, which in turn depends on the drill point geometry. The conventional twist drill has a large chisel edge as compared to the Brad and Spur drill, or candle stick drill, and the straight flute drill. Therefore, it produces higher thrust force and consequently higher tendency for delamination. Furthermore, HSS twist drill wears much faster than carbide twist drill, resulting in higher thrust force. Ultrasonic C-scan inspection specified that feed rate and drill diameter make the greatest contribution to drilling induced delamination. The candle stick drill and saw drill were found to cause smaller delamination factor than the twist drill [20].

Table 2.1. Empirical models for delamination factor in drilling fiber reinforced plastics.

No.	Reference	Cutting conditions	Model
1	Davim [14]	Woven-ply CFRP  $t$ : 3 mm $V_c$ : 30-50 m/min $f$ : 0.05-0.20 mm/rev $d$ : 5 mm	Standard twist drill bit (carbide) $F_d = 0.923 + 3.463 \times 10^{-3}V_c + 1.559f$ (entrance) $F_d = 0.966 + 1.085 \times 10^{-3}V_c + 0.134f$ (exit) Brad and Spur drill bit (carbide) $F_d = 0.991 + 4.65 \times 10^{-4}V_c + 0.097f$ (entrance) $F_d = 1.006 + 1.980 \times 10^{-4}V_c + 0.021f$ (exit)
2	Reis [21]	Woven-ply CFRP  $t$ : 3 mm $V_c$ : 16-32 m/min $f$ : 0.04-0.15 mm/rev $d$ : 5 mm $\theta$ : 118°	Standard twist drill bit (HSS) $F_d = 1.021 + 1.31 \times 10^{-3}V_c + 0.117f$ Helical flute drill (Carbide) $F_d = 1.010 - 1.16 \times 10^{-4}V_c + 0.097f$ Straight flute drill (Carbide) $F_d = 1.037 - 1.0 \times 10^{-3}V_c + 0.158f$
3	Tsao [20]	Woven-ply CFRP  $t$ : 3 mm $N$ : 800-1200 rpm $f$ : 0.01-0.03 mm/rev $d$ : 6, 8, 10 mm	Standard twist drill bit (HSS) $F_d = 1.961 - 1.81 \times 10^{-4}N - 10.955f - 1.77 \times 10^{-2}d$ Brad point drill bit (HSS) $F_d = 1.539 - 7.81 \times 10^{-6}N - 2.274f - 1.7 \times 10^{-2}d$ Slot drill bit (HSS) $F_d = 1.508 + 8.681 \times 10^{-6}N - 3.385f - 1.49 \times 10^{-2}d$
4	Sardinas [15]	UD-ply CFRP  $t$ : 4 mm $V_c$ : 30-50 m/min $f$ : 0.05-0.20 mm/rev $d$ : 5 mm	Standard twist drill bit (Carbide) $F_d = 1.93 f^{0.1429} V_c^{0.1022}$
5	Gaitonde [11]	Woven-ply CFRP  $t$ : 2.5 mm $V_c$ : 60-600 m/min $f$ : 1-6 m/min $d$ : 5 mm $\theta$ : 85-130°	Standard twist drill bit (carbide) $F_d = -0.810444 - 0.001889V_c - 0.109957f + 0.03454\theta + 0.000011V_cf - 0.000009V_c\theta + 0.00167f\theta + 0.000003V_c^2 + 0.00553f^2 - 0.000115\theta^2$

---

6	Khashaba [22]	Woven-ply CFRP	Standard twist drill bit (carbide)
		$t$ : 8.3 mm	$F_d = 1.482 + 1.44 \times 10^{-3}V_c + 3.143f + 0.0193W$
		$V_c$ : 6.5-50.5 m/min	
		$f$ : 0.056-0.45 mm/rev	
		$d$ : 8 mm	
		$W$ : 0-34×10 <sup>-4</sup> g	

---

$t$ : laminate thickness,  $f$ : feed rate,  $N$ : spindle speed,  $V_c$ : cutting speed,  $d$ : drill diameter, and  $W$ : tool pre-wear.

## 2.4 Assessment of delamination

The visualization and assessment of delamination damage is a difficult and challenging task since damage is internal and hidden. Obtaining the size, shape, and location of delamination is essential for the assessment of machining damage. Several non-destructive inspections are frequently used to observe drilling induced delamination damage in composite laminates, including optical microscope [19, 23-25], stereomicroscope [26], ultrasonic C-scan [20, 27-30], digital photography technique [13, 16, 22], shadow moiré laser based imaging technique [31], and X-ray computerized tomography (CT) [9, 32-34].

There exist several major methods used to assess the level of delamination damage around the drilled holes. In order to quantitatively measure the amount of delamination, Chen [34] proposed a method to obtain the value of the conventional delamination factor which is defined as the ratio of the maximum diameter  $D_{max}$  of the observed delamination zone to the nominal diameter  $D_{nom}$  of the drilled hole, as shown in Figure 2.8. Mathematically, this can be expressed as:

$$F_d = \frac{D_{max}}{D_{nom}} \quad (2.1)$$

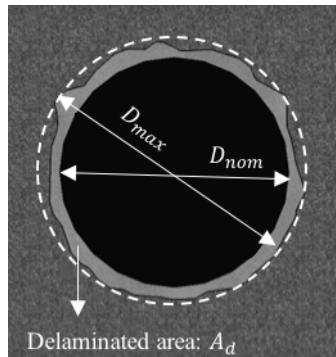


Figure 2.8. Schematic of the measurement of the delaminated area  $A_d$  and the maximum diameter  $D_{max}$ .

Conventional delamination factor presents satisfactory results when delamination possesses a regular pattern, as in glass fiber reinforced polymer laminates [10]. Nevertheless, when carbon fiber reinforced composite materials are drilled, delamination has an irregular form, containing breaks and cracks at the hole entry and exit. In this case, the conventional delamination factor is not an appropriate representation of the damage magnitude. Furthermore, this procedure does not take into account the damage area, as shown in Figure 2.9, where the same delamination factor is recorded for two distinct conditions. Hence, a novel approach is proposed in [35], namely adjusted delamination factor, and calculated through Eq. (2.2). The first part of this equation denotes the size of the crack contribution (conventional delamination factor), and the second part denotes the damage area contribution.

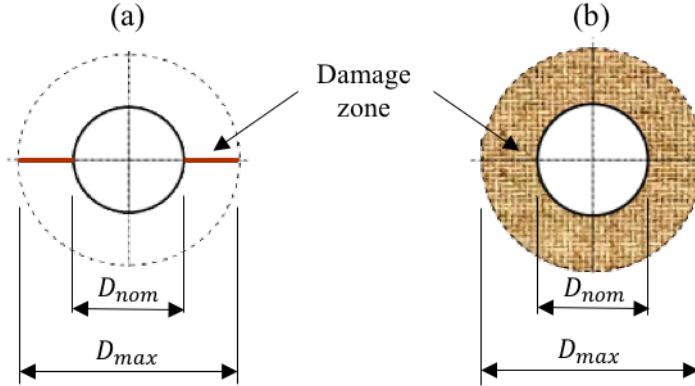


Figure 2.9. Critical cases when drilling FRP laminates; (a) fine cracks, and (b) uniform damage area [35].

$$F_{da} = \alpha \frac{D_{max}}{D_{nom}} + \beta \frac{A_{max}}{A_{nom}} \quad (2.2)$$

Where  $A_{max}$  is related to the maximum diameter of the delamination zone ( $D_{max}$ ), and  $A_{nom}$  is the area of the nominal hole ( $D_0$ ). The parameters  $\alpha$  and  $\beta$  are used as weights in the parts of Eq. (2.2). Therefore:

$$A_{max} = \pi \frac{D_{max}^2}{4} \quad (2.3)$$

$$A_{nom} = \pi \frac{D_{nom}^2}{4} \quad (2.4)$$

Substituting Eqs. (2.1), (2.3), and (2.4) into Eq. (2.2), gives:

$$F_{da} = \alpha F_d + \beta F_d^2 \quad (2.5)$$

In Eq. (2.5),  $\beta$  is considered as the ratio of the damage area  $A_d$  to the area corresponding to  $D_{max}$  ( $A_{max}$ ) minus the nominal hole area ( $A_{nom}$ ). The parameter  $\alpha$  is the complement of  $\beta$ , that is,  $\alpha = 1 - \beta$ . Hence, Eq. (2.5) can be rewritten as:

$$F_{da} = (1 - \beta) F_d + \beta F_d^2 \quad (2.6)$$

$$F_{da} = F_d + \frac{A_d}{A_{max} - A_{nom}} (F_d^2 - F_d) \quad (2.7)$$

Thus,

$$\text{If } \begin{cases} A_d \rightarrow (A_{max} - A_{nom}) \Rightarrow F_{da} \rightarrow F_d^2 \\ A_d \rightarrow 0 \Rightarrow F_{da} \rightarrow F_d \end{cases}$$

This indicates that if the trend is a delamination area equal to the crow area embody of maximum diameter ( $D_{max}$ ) of the delamination zone, the adjusted delamination factor presents a value equal to the square of the conventional delamination factor, uniform behavior without isolated crack. Nevertheless, if the delamination area is minimal, the adjusted delamination factor presents a value tending to the convention factor, see Figure 2.9.

## 2.5 Modeling delamination propagation

Drilling induced delamination is directly related to the component of cutting force along the drill axis known as thrust force. Thrust force has been considered as the main cause of delamination by several researchers and it is generally believed that there is a critical thrust force below which no damage occurs [36-41]. Analytical study of this thrust force is thus interesting in order to avoid delamination.

Several researchers attempted to model critical thrust force for delamination propagation. The first analytical model was proposed by Hocheng and Dharan [42]. They employed linear elastic fracture mechanics (LEFM) and classical plate theory to formulate an analytical expression to predict the critical thrust force at the onset of delamination during drilling of composite materials. The proposed model predicts the threshold load (the minimum force above which delamination is initiated) as a function of material properties and uncut-plies thickness under drill bit, as described in Section 2.5. The isotropic behavior and pure bending of laminate are assumed in their model. Jain and Yang [43, 44], developed this model, considering the anisotropy of the material and hypothesizing that the cracks are elliptical. In their model, the drilling thrust force is simplified by a representative single concentrated central load. Nevertheless, the thrust force in drilling operation does not come through the center of twist drill bit as a concentrated force, rather it is spread over the whole length of the cutting lips and the chisel edge. Upadhyay *et al.* [45] developed this model by assuming the thrust force as a uniformly distributed load over the drill bit diameter instead of a concentrated load.

Lachaud *et al.* [46] determined critical thrust force for two cases, concentrated and uniformly distributed, considering an embedded small-diameter circular plate and non-propagated cracks. Hocheng and Tsao [29] extended these models, taking into consideration a series of loading types such as circular load, concentrated centered load associated with circular load, distributed circular load, and stepwise distributed circular load for various drill types including saw drill, candle stick drill, core drill, and step drill, respectively. Table 2.2 summarized the most important analytical models proposed so far.

A positive linear correlation between delamination size and thrust force for various drill bits was observed when the applied force exceeds the critical value [13, 20, 26, 29]. This result confirms that the key for overcoming delamination when drilling FRP laminates lies in reducing the thrust force associated with drilling process through optimizing input variables.

Table 2.2. Analytical models for predicting critical thrust force at the onset of delamination in drilling process.

No.	Reference	Cutting conditions	Model
1	Hocheng and Dharan [42]	Twist drill Concentrated central load Isotropic Circular zone	$F_C = \pi \sqrt{\frac{8G_{IC}Eh^3}{3(1-v^2)}}$
2	Jain and Yang [44]	Twist drill Concentrated central load Anisotropic elliptical zone	$F_C = 3\pi^4 \sqrt{\frac{D_{22}}{D_{11}}} \sqrt{2G_{IC}D_c^*}$
3	Upadhyay [45]	Twist drill Uniformly distributed load Isotropic Circular zone	$F_C = \pi \sqrt{\frac{32G_{IC}D}{1 - \frac{c^2}{2a^2}}}$
5	Lachaud [46]	Twist drill Uniformly distributed load Orthotropic elliptical zone	$F_C = 8\pi \sqrt{\frac{G_{IC}}{\frac{1}{3} - \frac{D'}{8D}}}$
6	Zhang [47]	Twist drill Concentrated central load Orthotropic elliptical zone	$F_C = \sqrt{\frac{\pi G_{IC}}{\xi(C_3 - K)}}$
7	Gururaja [48]	Twist drill Uniformly distributed load Orthotropic elliptical zone	$F_C = 8\pi \sqrt{\frac{G_{IC}}{\frac{1}{3} - \frac{D'}{8D}}}$
8	Hocheng and Tsao [29]	a. Slot drill bit b. Brad point drill bit c. Core drill bit d. Step drill bit	$F_a = \frac{\pi}{\sqrt{1 - 2s^2 + s^4}} \sqrt{\frac{8G_{IC}Eh^3}{3(1 - v^2)}}$ $F_b = \frac{(1 + \alpha)\pi}{\sqrt{1 + \alpha^2(1 - 2s^2 + s^4)}} \sqrt{\frac{8G_{IC}Eh^3}{3(1 - v^2)}}$

$$F_c$$

$$= \frac{\beta(2-\beta)\pi}{\sqrt{[1-(1-\beta)^4] - \frac{s^2[1-(1-\beta)^6]}{2}}} \sqrt{\frac{8G_{IC}Eh^3}{3(1-v^2)}}$$

$$F_d = \frac{\sqrt{2}\pi k}{1-v^2} \sqrt{\frac{8G_{IC}Eh^3}{3(1-v^2)}}$$

$$= \frac{k}{[2(1-v)(1+2v^2) - 12(12-4v+3v^2+3v^3)\xi^2 - 8(1+3v)\xi^2 \ln \xi]}$$

### 2.5.1 Analytical model for push-out delamination

A linear elastic fracture mechanics model for predicting the onset of delamination due to the applied thrust force was developed by Hocheng and Dharan [42]. Hocheng stated that the following assumptions have to be made for the applicability of LEFM to composite materials:

1. Crack propagation must be coplanar,
2. The crack must lie in a plane of material symmetry,
3. The plastic zone at the crack tip must be very small.

Figure 2.10 depicts a twist drill and the induced delamination. In this figure, the center of the circular plate is loaded by a twist drill of diameter  $D$ ,  $F_A$  is the applied thrust force,  $x$  is the tool displacement,  $H$  is the thickness of the laminate,  $h$  is the uncut depth under the tool, and  $a$  is the assumed size of an existing crack. As the drill proceeds, the uncut laminates under the tool are pushed and deformed elastically by the thrust force. If the resulting strain at the top of the existing crack goes beyond the critical value, crack propagation occurs. The equation of energy balance can be expressed as follows using linear elastic fracture mechanics:

$$G\pi(d+2a)da = F_A dx - dU \quad (2.8)$$

Where  $G$  is the energy release rate per unit area. In Eq. (2.8), the term on the left side represents the energy required to extend the crack by a distance  $da$ . The term on the right side is the work done by the thrust force as it moves a distance  $dx$  and the second term is the stored strain energy. To find the relation between  $F_A$ ,  $x$ , and  $U$ , classical plate theory for a clamped circular plate subjected to a concentrated load in the center is used in this model. This gives [49]:

$$U = \frac{8\pi Mx^2}{\left(a + \frac{d}{2}\right)^2} \quad (2.9)$$

Where  $M$  is the flexural rigidity of the plate expressed as:

$$M = \frac{Eh^3}{12(1 - v^2)} \quad (2.10)$$

Where  $E$  is the modulus of elasticity and  $v$  is Poisson's ratio. The displacement  $x$  is:

$$x = \frac{F_A \left(a + \frac{d}{2}\right)^2}{16\pi M} \quad (2.11)$$

Eq. (2.8) can, therefore, be rewritten as:

$$\begin{aligned} 2G\pi \left(a + \frac{d}{2}\right) &= F_A \frac{dx}{da} - \frac{dU}{da} \\ &= F_A \frac{d}{da} \frac{F_A \left(a + \frac{d}{2}\right)^2}{16\pi M} - \frac{d}{da} \frac{F_A^2}{32\pi M} \\ &= \frac{F_A^2 \left(a + \frac{d}{2}\right)}{16\pi M} \end{aligned} \quad (2.12)$$

Substituting Eq. (2.10) into Eq. (2.12) and solving for  $F_A$ , the critical load at the onset of crack propagation can be obtained as:

$$F_A^* = \pi \left( \frac{8G_{IC} Eh^3}{3(1 - v^2)} \right)^{1/2} \quad (2.13)$$

It should be noted that, in this model, critical strain energy release rate in Mode I fracture,  $G_{IC}$ , is used for  $G$  since it can be easily measured, although plane strain conditions may not always be fulfilled. Nevertheless, this value, which is lower than that for the plane strain case, gives conservative predictions for the critical load. Moreover, the highest  $E$ , in the 1-direction or principal direction, is used overall for the adopted isotropic calculation instead of using a complicated derivation for the anisotropic case. This also provides a conservative prediction for the critical load.

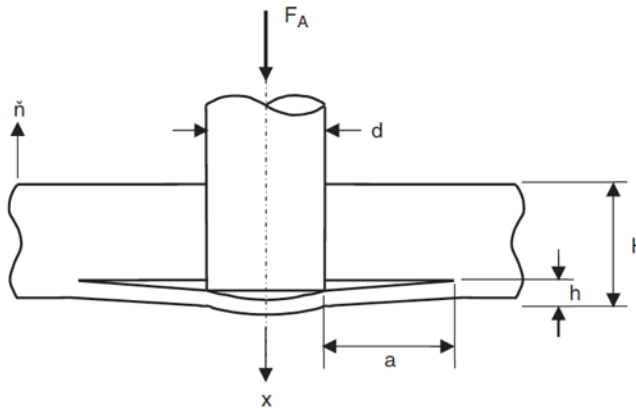


Figure 2.10. Circular plate model for delamination analysis [50].

## 2.5.2 Analytical model for peel-up delamination

In the case of peel-up delamination, it is assumed that the critical peeling force  $F_p^*$  is related to the critical thrust force by a peeling factor expressed as:

$$k_p = \frac{F_A^*}{F_P^*} \quad (2.14)$$

Where  $k_p$ , the peeling factor, is a function of tool geometry and friction between the tool and workpiece.

Using the same analysis of push-out model and replacing the uncut depth  $h$  by the cut thickness  $h_d = H - h$ , the critical peeling force is obtained as:

$$F_P^* = \pi \left( \frac{8G_{IC}Eh_d^3}{3(1-v^2)} \right)^{1/2} \quad (2.15)$$

## 2.5.3 Analytical model for orthotropic materials

In spite of the fact that the analytical model developed by Hocheng and Dharan was a good start, it has some limitations. Several assumptions are not always correct in drilling of composite laminates. For instance, the layers are assumed to be isotropic. However, each layer is highly anisotropic and a realistic shape of delamination should be taken into account. Accordingly, Jain and Yang developed a realistic model for correlating thrust force with the onset of delamination [44]. As illustrated in Figure 2.11, the delamination zone for unidirectional composites is modeled as an elliptical plate, with clamped edges and subjected to a central load. In this figure,  $a$  and  $b$  are respectively half the delamination sizes along the fiber and transverse directions. Based on fracture mechanics and laminated plate theory, expressions are developed for critical thrust force at which delamination is initiated at different ply location.

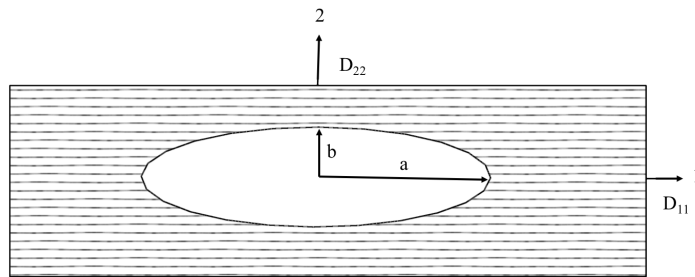


Figure 2.11. Schematic shape of the delamination zone in a unidirectional laminate [44].

From LEFM, the energy balance gives:

$$F_{th}dw = GdA + dU \quad (2.16)$$

Where  $G$  is the energy release rate per unit area,  $U$  is the stored strain energy,  $F_{th}$  is the force applied, and  $w$  is the distance moved by the drill. Using laminated plate theory, the deflection for

an elliptical plate of dimensions  $a$  and  $b$ , clamped and subjected to a central concentrated load can be expressed as:

$$w = \frac{F_{th}}{\pi ab \left[ \frac{6D_{11}}{a^4} + \frac{4(D_{12} + 2D_{66})}{a^2 b^2} + \frac{6D_{22}}{b^4} \right]} \quad (2.17)$$

Where  $D_{ij}$  are the coefficients of the stiffness matrix of the plate in bending, see Appendix A.

The expression for strain energy in on-axis, U.D. laminate is:

$$U = 4\pi w^2 \left[ \frac{D_{11}}{a^4} + \frac{2(D_{12} + 2D_{66})}{3a^2 b^2} + \frac{D_{22}}{b^4} \right] \quad (2.18)$$

Substituting  $dw$ ,  $du$ , and  $dA$  into the energy balance equation and solving for  $F_{th}$ , the critical thrust force is obtained as:

$$F_{th}^* = 3\pi \left( \frac{b}{a} \right) \sqrt{2G_{IC} D^*} \quad (2.19)$$

Where:

$$D^* = D_{11} + \frac{2(D_{12} + 2D_{66})}{3} \left( \frac{a}{b} \right)^2 + D_{22} \left( \frac{a}{b} \right)^4 \quad (2.20)$$

Eq. (2.20) indicates that the critical load is a function of elasticity ratio  $a/b$ . The minimum critical load corresponds to a value of  $a/b = (D_{11}/D_{22})^{1/4}$ . Since the delamination zone is free to have any shape the smallest value of critical thrust force should be used to avoid delamination. Substituting the value of  $a/b$  into Eq. (2.20) gives:

$$F_{th}^* = 3\pi^4 \sqrt{\frac{D_{22}}{D_{11}}} \sqrt{2G_{IC} D_c^*} \quad (2.21)$$

Where:

$$D_c^* = 2D_{11} + \frac{2(D_{12} + 2D_{66})}{3} \sqrt{\frac{D_{11}}{D_{22}}} \quad (2.22)$$

The applied thrust force must not exceed the values obtained above, Eqs. (2.15), (2.13), and (2.21), which is a function of the material properties and the uncut thickness, to avoid delamination.

## 2.6 Drilling thrust force and torque

The cutting forces generated during drilling process are referred to as thrust force, or axial force along the direction of the feed, and torque, or rotational momentum. In drilling of metals, these forces are uniform with time because of the uncut chip thickness is constant. In drilling composite materials, by contrast, the drilling forces are cyclic because of the instantaneous changes in the fiber orientation. The maximum value of the thrust force is an interesting parameter as delamination propagates due to the thrust force. This force generated by the cutting action of the

two cutting lips and the chisel edge of the drill tool. It is observed that the chisel edge is a major contributor to the thrust force [44]. Moreover, the amplitude of the thrust force is highly decreased and its frequency is increased when the number of flutes is increased or when drilling cross-ply and quasi-isotropic laminates [43].

The drilling torque is caused by the cutting force couple acting on the cutting lips and its magnitude is determined by the product of the cutting force and the drill diameter expressed as below:

$$T = 2F_c \frac{r}{2} = F_c \frac{d}{2} \quad (2.23)$$

Where  $F_c$  is the cutting force on the cutting lip,  $r$  is the drill radius, and  $d$  is the drill diameter. It is assumed that  $F_c$  is an equivalent cutting force that acts at the center of the uncut chip area and that the chisel edge width is negligible.

### **2.6.1 Influence of drilling parameters on thrust and torque**

Thrust force and torque have a significant effect on the quality of a machined hole. The drilling thrust force and torque are themselves influenced by the cutting variables, tool geometry, tool type, tool material, and workpiece material.

#### ***Feed rate and cutting speed***

The effects of cutting parameters, i.e. feed rate and cutting speed, on the thrust force and torque were investigated by several researchers. Most studies show that both thrust force and torque increase with increasing the feed rate [50-60]. This is mainly because of the increasing of the uncut chip cross sectional area, which leads to increasing the resistance of chip formation and, accordingly, the cutting forces. Unlike feed rate, the effect of cutting speed on thrust force is insignificant, whereas torque increase with cutting speed [61, 62]. However, Khashaba *et al.* [22] found that the effect of cutting speed on thrust force in drilling woven GFRP composite laminates varies with tool wear.

#### ***Twist drill geometry***

The drill geometry parameters that influence the thrust force and torque include drill point angle, chisel edge width, web thickness, and drill diameter. The effect of these parameters has been presented by many investigators [17, 30, 34, 52, 63]. An increase in the drill point angle leads to an increase in the thrust force due to the increase of shear area and a decrease in the torque. The torque decrease is associated with the increase of the orthogonal rake angle at each point on the primary cutting edge with the increase in point angle. Furthermore, an increase in web thickness leads to an increase in both thrust and torque. This is because the larger web thickness, the longer the chisel edge length and the smaller the orthogonal rake angle at each point on the primary cutting edge. The chisel edge was found to contribute 40-60% of the total thrust force under normal feed rates [44, 64, 65]. In order to investigate the effect of the drill diameter on the thrust force and torque, El-Sonbaty *et al.* [6] used conventional HSS twist drills with different diameters from 8 to 13 mm to drill GFRP composites using a constant spindle speed and feed rate. The results indicate

that both thrust force and torque increase with increasing drill diameter. Mohan *et al.* [66] also investigated the effect of drill size on thrust and torque and observed similar behavior.

### **Tool type**

The effect of drill type on thrust force and torque were found to be very significant [67]. Several investigations were carried out to reduce drilling thrust force using custom-designed drill bits. Latha *et al.* [68] studied the influence of three different drills, namely brad and spur, multifaceted and step drill, on thrust force in drilling GFRP composites. The highest thrust force generated during drilling process was observed for Brad and Spur drill, and the least thrust force is observed for step drills. Grilo *et al.* [69], by contrast, found that Spur drill produce the least amount of delamination among three drills, namely an helical drill with a 140° point angle, a four-flute drill, and a Spur drill. Piquet *et al.* [70] designed a new drill tool with a specific tool geometry consisting of three cutting edges which gave an excellent drilling quality in thin carbon/epoxy composites, compared to conventional twist drills. Durao *et al.* [71] also studied the effect of drill type on the thrust force in drilling CFRP laminates. They employed five tungsten carbide drills with 6 mm diameter and different geometries including twist drill with 120° point angle, dagger drill, twist drill with 85° pony angle, Brad drill, and special step drill. The results show that the thrust forces of the latter three drill are, respectively, on average of 18 %, 22 %, and 36 % of the former drill.

### **Tool materials**

Traditionally, cutting materials including high speed steel [72], cemented carbides [73], coated carbides [74], and polycrystalline diamonds (PCDs) [75] are used in conventional drilling process of composite materials. Arul *et al.* [76] compared three different tool materials (i.e. HSS, TiN coated HSS, and tipped tungsten carbide drills) in drilling of GFRP composites. The results show that cemented tungsten carbide tipped drills excel over the other two materials in terms of lower thrust, lower flank wear, and better hole quality. It was also found that coating techniques yield only a very limited improvement in drilling performance, because the coated layer on the cutting edges was easily peeled off under the cyclic compressive and tensile forces. Ramesh *et al.* [77] studied the influence of tool materials on thrust force and delamination of S-GFRP composites by using different tool materials including solid carbide, TiN coated solid carbide, and HSS. The drilling operation with HSS leads to maximum thrust force and delamination, while solid carbide drill bits results in the minimum thrust force and delamination. The works conducted by Spur and Wunsch [78], revealed that polycrystalline diamond tools outperform many conventional tools (e.g. HSS, WC, etc.) because of the fact that their ceramic bonds excel the metallic bonds in conventional tools in terms of bond strength. In spite of the outstanding performance of diamond tools, survey results presented by Abrao *et al.* [63] show that HSS and tungsten carbides are equally used as tool materials while PCD is seldom used. The reason for the small market share of PCDs may result from the high cost and difficulty to fabricate PCD tools with sophisticated geometries. The unit cost of a PCD tool is 3-5 times the unit cost of a chemical vapor deposition diamond coated carbide tool and 6-10 times that of a non-coated carbide tool [67].

### **Workpiece material**

Workpiece material also affects the drilling thrust force and torque. Some of the common composite laminates used for drilling studies are carbon fiber reinforced polymers, glass fiber reinforced polymers and fiber metal laminates. Varatharajan *et al.* [79] compared machining characteristics of glass fiber reinforced thermoplastic (polypropylene resin) and thermosets composites (polyester resin). Unlike the case of rupture associated drilling in the thermoset composites, the thermoplastic composites undergo plastic deformation by thermal induced matrix sliding and removal of material. They also observed higher order of thrust force and torque in drilling thermoset composites. Khashaba *et al.* [58] studied the cutting forces in drilling of chopped composites with different fiber volume fractions. Based on the results, fiber volume fraction is directly proportional with thrust force and torque. They also reported that for the same matrix type (polyester), chopped composite has higher thrust force than woven composite, while it has lower push-out delamination. In contrast, the torque of woven/polyester composites is higher than that of chopped/polyester composites [16].

After presenting several experimental studies to investigate cutting phenomena in drilling of composites, some researchers developed empirical models for thrust force using linear regression analysis. Table 2.3 summarizes the most important empirical models for thrust force in drilling FRP laminates.

*Table 2.3. Empirical models for thrust force in drilling FRPs.*

No.	Reference	Cutting conditions	Model
1	Jain [43, 44]	UD-ply CFRP  t: 4.56 mm f: 0.02-0.12 mm/rev d: 6.35, 12.7 mm  θ: 118°  $H_B$ : 98 kg/mm <sup>2</sup>	Standard twist drill bit (HSS)  $F_T = d^2 H_B \left[ \frac{1.91 f^{0.4}}{d^{1.2}} + \frac{0.101}{d} \right]$ $F_T = 0.136 H_B d^{0.78} f^{0.4}$ (simplified)
2	Mathew [80]	UD-ply GFRP  t: 4 mm $V_f$ : 0.4 $V_c$ : 50 m/min f: 0.01-0.2 mm/rev d: 8,10,14,16 mm	Standard twist drill bit  $F_T = 48.98 d^{0.783} f^{0.41}$ Saw drill  $F_T = 48.98 d^{0.242} f^{0.37}$

---

3	Won [65, 81]	Carbide tipped twist drill $t$ : 8.1 mm $V_f$ : 0.6 $N$ : 300 rpm $f$ : 0.1-1.0 mm/rev $d$ : 6.35, 7.9, 9.5 mm	Woven-ply AFRP $F_T = 35.84(fd)^{0.5} - 0.09d^2$ Woven ply CFRP $F_T = 40.77(fd)^{0.66} - 0.36d^2$
4	Mohan [66]	E-glass chopped fiber mat $t$ : 10 mm $V_f$ : 0.63 $N$ : 400 rpm $f$ : 0.1-0.7 mm/rev $d$ : 6,10 mm	Carbide coated drill bit $F_T = 35.004(fd)^{1.3844} - 0.23d^2$
5	Fernandes [82]	CFRP $t$ : 2, 4, 5.2 mm $N$ : 750-1500 rpm $f$ : 0.03-0.12 mm/rev $d$ : 4.9 mm	Straight-flute drill bit (Carbide) $F_{T1} = (0.003N + 1.0467) \times [76.56(fd)^{0.39} + 1.047d^2]$ $F_{T2} = (0.0036N + 1.2128) \times [76.56(fd)^{0.39} + 1.047d^2]$ $F_{T3} = (0.0035N + 1.5159) \times [76.56(fd)^{0.39} + 1.047d^2]$
6	Tsao [83]	Woven-ply CFRP $t$ : 3.6 mm $N$ : 800-1200 rpm $f$ : 0.0375-0.0625 mm/rev $d$ : 10 mm $W_t$ : 0.8-1.2 mm $G$ : 100-400 #	Core drill bit (diamond grits) $F_T = -23.02 + 54W_t + 0.181G - 224f + 9.575 \times 10^{-2}N$
7	Singh [52]	UD-ply CFRP $t$ : 3mm $N$ : 375-1500 rpm $f$ : 0.075-0.3 mm/rev $d$ : 10 mm $d$ : 10 mm $\theta$ : 90-118°	Standard twist drill bit (HSS) $F_T = 1.4363\theta + 402.8315f - 98.0319$

---

---

8	Tsao [84]	Woven-ply CFRP  t: 6 mm N 800-1200 rpm f: 0.01-0.03 mm/rev d: 10 mm $\xi$ : 0.2-0.6 $\gamma$ : 80-120° $\theta$ : 118°	Step drill bit (HSS)  $F_T = 115.82 - 0.912\gamma - 224.25\xi + 352.778f - 1.028 \times 10^{-3}N$
10	Khashaba [22]	Woven-ply GFRP  t: 8.3 mm $V_c$ : 6.5-50.5 m/min f: 0.056-0.45 mm/rev d: 8 mm $W$ : $0-34 \times 10^{-4}$ g $\gamma$ : 80-120° $\theta$ : 118°	Standard twist drill bit (Carbide)  $F_T = -161 + 3.71V_c + 977.781f + 12.793W$

---

## 2.7 Approaches to prevent delamination

Analytical and empirical models discussed above imply that delamination is likely to occur when the applied drilling thrust force exceeds a threshold value. Therefore, to avoid the drilling induced delamination, the thrust force applied to workpiece should remain below the critical thrust force. On one hand, critical thrust force is a function of workpiece material properties, drill geometry, and uncut plies thickness under drill bit. On the other hand, the critical thrust force is drilling characteristic which depends on some special conditions. Most researches on delamination free drilling of composite laminates highlighted the importance of keeping the thrust force below the critical value and increasing the threshold value. Several methods are used for this purpose which are described in the following sections.

### 2.7.1 Back-up plate

One of the commonly used methods to reduce drilling induced delamination is to increase stiffness of the bottom ply of the laminate. This can be done by either increasing thickness of the bottom ply or using a support plate. A back-up support underneath the workpiece counteracts the downward bending deflection of the laminate caused by the thrust force. At the beginning of drilling operation, the support plate is in full contact with the bottom surface of the workpiece, resulting in a uniform upward reaction load applied to the back side of the workpiece. As drilling proceeds, the laminate starts deflecting slightly. The back-up plate logically has higher stiffness than the laminate; hence, it does not fully conform to the laminate deflection. The internal reaction force with the downward bending of the uncut laminate lifts up the laminate and this changes the back-up force from a uniform load to a peripherally distributed load. Therefore, the deflected specimen is subjected to both concentrated thrust force on the entry side and circular back-up force from bottom side, as shown in Figure 2.12.

The research conducted by Capello [7] when drilling with and without support plate pointed out that the former method can effectively reduce drilling induced delamination. The primary application of using the support plate is to prevent deflection of the composite laminate. Therefore, a significant reduction in delamination can be achieved by limiting the workpiece dynamics. Tsao and Hocheng [85] investigated the influence of back-up plate on drilling induced delamination when using a slot drill bit and a core drill bit. They found that delamination in drilling with support plate is less likely to occur due to increase of critical thrust force.

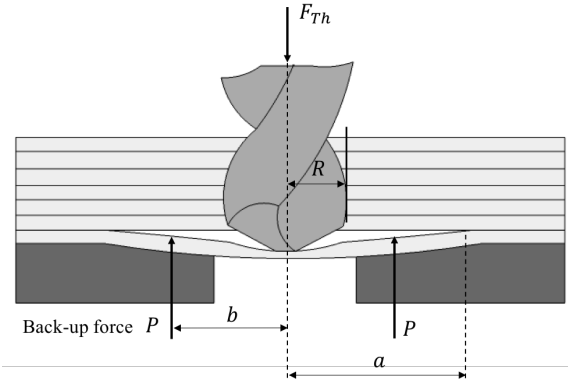
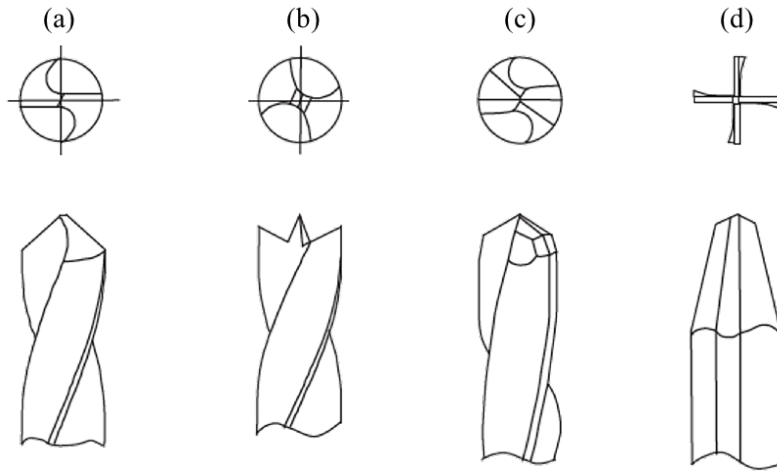


Figure 2.12. forces when drilling composite laminates using a back-up plate.

### 2.7.2 Special drill bits

The drill geometry is also a key element in drilling thrust force. Different tool geometry which reduces the thrust force will result in less delamination. Thus, proper selection of drill bit is of the utmost important to avoid delamination damage. Twist drill bits are by far the most commonly used cutting tool in most drilling operations. The center of the twist drill, called chisel edge, is a major contributor to delamination. The contributions of chisel edge to the thrust force for twist drill is reported to be in the range of 40–60% of the total thrust force [65]. The use of smaller chisel edge has been recommended for minimization of delamination due to lower thrust force.

Several special drill bits designed for this purpose such as candle stick drill [29], straight flute drill bit [56, 82, 86], saw drill [29], step drill bit [9, 33, 50, 84, 87], core drill bit [29, 43, 50, 83], step-core drill bit [28], multifaceted drill bit [88, 89], and split drill [90]. These drill bits are designed in a such way that higher critical thrust force is achieved by reducing the chisel edge length and distributing the forces away from the center of the drill, i.e. avoiding concentrated force. Among the drill bits shown in Figure 2.13, the candle stick drill and the straight flute drill produce the lowest delamination damage, where the style drill works best in thin laminates. This is because both drills have smaller chisel edge width. The success of the eight-facet drill is attributed to the long taper angle at the shoulder, which tends to minimize fiber breakout.



*Figure 2.13. Different drill bits; (a) standard twist drill, (b) candle stick drill, (c) multifaceted drill, (d) straight flute drill.*

### 2.7.3 Pre-drilled pilot holes

When drilling with a twist drill, the efficiency of the cutting action varies along the drill radius, being the most efficient at the outer diameter of the drill and the least efficient at the center. In fact, the relative velocity at the drill point is zero, without cutting action. In other words, the chisel edge of the drill point pushes the material aside at the center as it cut into the workpiece. The chisel edge in such drills is a major contributor to the thrust force that is the primary cause of delamination when drilling composite laminates. This is the reason why it is difficult to obtain delamination-free hole when using conventional twist drills.

Drilling induced delamination can be significantly reduced with a pilot hole as shown schematically in Figure 2.14. A hole is pre-drilled to eliminate the thrust force caused by the chisel edge, thus the threat for delamination is greatly reduced. The diameter of the pre-drilled hole is set equal to the chisel edge width. Smaller diameter of pilot hole cannot counteract the effect of chisel edge, while larger one tends to cause undesired delamination during pre-drilling.

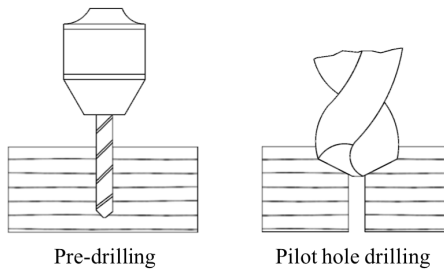


*Figure 2.14. Drilling hole in a pre-drilled laminate.*

### 2.7.4 Variable feed rate strategy

In order to avoid delamination, the laminate can be drilled at a very low feed rate in such a way that the critical thrust force is never exceeded. However, using low feed rates not only reduces the

efficiency and productivity but also may cause thermal damage to the drilled laminate. A more practical strategy is to use variable feed rate to slow the feed rate at entry and exit and to the highest possible feed rates in between. In actual implementation of the strategy, the feed rate upon approach to the entry and exit can be decreased discretely in a staircase manner or in a continuous manner as shown in Figure 2.15. The feed rate for each step is obtained based on the analytical models so that the thrust force always remains below the critical thrust force for delamination at the particular thickness of the step.

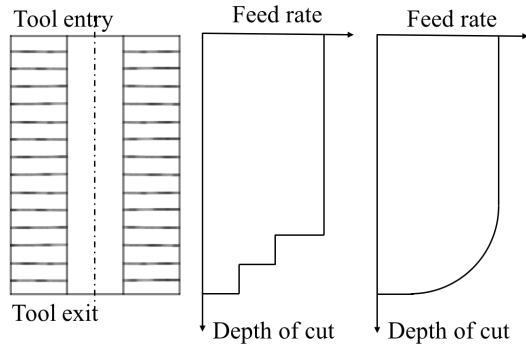


*Figure 2.15. Variable feed rate strategy for delamination free drilling; staircase type and a continuous variation of feed rate along the depth of workpiece.*

### 2.7.5 Two-side drilling

Delamination in thick composite laminates can be avoided by drilling from both sides of the laminate with a diamond tipped hole saw (core drill). The laminate is drilled half way through the thickness from one side then cut through from opposite side. All the cutting forces acted at the center of the laminate and there is no resultant force pushing out the bottom of the hole. This process can be accomplished as an N/C operation and with the use of coolant. Although this practice is not practical for small diameter holes, it is a reasonable solution for large diameter holes. This operation unavoidably leaves a little material at the center of the hole which can be removed with a finishing operation if necessary.

### 2.7.6 High speed drilling

High speed drilling is not only recognized as one of the key manufacturing technologies for higher productivity but also well known as an efficient method to reduce delamination when drilling fiber reinforced composite laminates. The reason behind the enhancement of the drilling process performance with high speed is based on the relationship between the rotational speed and the axial feed of the cutting tool. The increase in rotational speed of the tool for a fixed feed reduces the feed per tooth, which can greatly reduce the drilling thrust force within a certain range, and consequently reduces the delamination damage. Despite this, high speed drilling is associated with unfavorable tool dynamics and friction-induced temperature rise which leads to accelerated tool wear and thermal material damage. Furthermore, reducing the feed per tooth to extremely low values could result in a reversed force trend due to high cutting pressure.

## 2.8 Delamination and residual mechanical properties

The damage generated during the drilling of FRP laminates is detrimental to the residual mechanical properties and significantly reduces the composite performance in use. For this reason, the study of damage tolerance which refers to the experimental determination of the residual properties of the damaged laminates calls for attention.

Some mechanical tests both under static and cyclic load conditions are proposed in the literature to study the residual strength of drilled composite laminates. Tagliaferri *et al.* [38] conducted drilling tests on glass fiber reinforced plastic composites to study the effect of machining parameters on the mechanical behavior of the material. The residual tensile strength was found to be independent of the damage extent. However, the bearing strength was influenced by the damage and a reduction in damage was accompanied by an increase in the bearing strength. Ghasemi *et al.* [91] studied the compression behavior of woven CFRPs with moulded-in and drilled holes and indicated that the strength of the moulded-in hole panels are always greater than those of the drilled hole ones. Persson *et al.* [92] investigated the effect of drilling induced damages on the strength and fatigue life of carbon/epoxy laminates subjected to static and fatigue loads. They observed that drilling induced damages significantly reduced the static and fatigue strengths of pin-loaded laminates; the effects on the strengths of compressively loaded laminates were less pronounced. Capello and Tagliaferri [93, 94] investigated the influence of drilling conditions on the residual mechanical behavior of the glass fiber reinforced composites subjected to a bearing load. They found that in order to improve the static bearing load (SBL) behavior of the drilled holes, lower feed rate should be selected with the use of a support plate. Singh and Bhatnagar [95] investigated the effect of drilling induced damage on the residual tensile strength of unidirectional composite laminates with drilled holes for a diversity of solid carbide drill-point geometries under different drilling conditions and developed a mathematical model correlating the residual strength with the drilling parameters. Kishore *et al.* [96] studied the effect of cutting speed, feed rate, and drill point geometry on residual tensile strength of the drilled unidirectional glass fiber reinforced epoxy composites. They observed that feed rate has the least influence and cutting speed has the maximum influence on residual tensile strength, and it increases substantially with an increase in cutting speed. In contrast, Zarif *et al.* [97] observed that feed rate has the most important effect and cutting speed has the least effect on the residual tensile strength of the drilled woven glass/epoxy composites. They also studied the effects of the drilling parameters on the compression behavior of GFRPs and reported that the residual compressive strength is most affected by feed rate.

# CHAPTER 3

## 3 ANALYTICAL ANALYSIS

Problems related to the drilling of FRP laminates are related to the cutting forces developed during the process. The main cutting force measured during drilling process is thrust force that acts along the direction of the feed rate. Although drilling thrust force has been cited as the main cause of delamination by several researchers and some have reported that the value of thrust force at which delamination occurs, very few attempts have been made to analytically correlate thrust force (and feed rate) with the onset of delamination in composite laminates. In this chapter, analytical models are proposed to correlate feed rate and thrust force with the onset of delamination.

### 3.1 Cutting force models for drilling

The performance of the drilling operation is evaluated based on the quality of the hole, the cycle time, and the cost of the tool per hole drilled. The quality of the hole includes characteristics such as roundness and cylindricity errors, surface finish, burrs, delamination in drilling fiber-reinforced composites, etc. Most of the performance parameters are related to the cutting forces generated in the process. Modeling the cutting forces in drilling, in terms of the tool geometry and machining conditions, is an important step in developing a simulation-based platform for the design and evaluation of new drill point geometry to improve quality and productivity.

A detailed review of dynamic cutting models is provided in Ehmann *et al.* [98]. The early force models developed for the drilling process were purely empirical. As the understanding of the mechanics of metal-cutting processes improved, several theoretical models were developed for the cutting forces [99-101]. Two approaches are widely adopted to analytically model the cutting forces in different machining processes, including drilling. They are the shear-plane method based on an orthogonal cutting model proposed by Merchant [99] which is later extended for oblique cutting by Shaw *et al.* [101], and the plasticity based shear zone model proposed by Oxley [102]. These models have had only limited success in precisely predicting the cutting forces because of difficulties in determining several model parameters from elasticity and plasticity theory or even from machining experiments. Additionally, these models are inappropriate for drilling FRPs since the mechanics of machining composites is very different from that of metals. The chip formation process during machining FRP laminates results from a series of fractures [98].

To overcome these challenges, Chandrasekharan *et al.* [103] adopted a mechanistic approach to develop cutting force models to predict the thrust and torque in drilling with application to fiber-reinforced composite materials. The mechanistic approach uses a different set of fundamentals of the process including the geometry of the process. The geometry of the process (chip load, chip thickness, cutting angles) remains the same whether machining metals or FRPs. This approach combines the analytical models developed for the cutter and the cut geometry with well-established empirical models relating force components to the chip load. The inputs to the model are the

machining conditions and the tool geometry and the model predicts the thrust and torque profile along the cutting lips and the chisel edge of the drill.

In the next section, a standard orthogonal cutting force model which fully describes the force system is described. The approach adopted to model the forces here is similar to Chandrasekharan model in that the cutting lips are divided into elements and the forces at each element are summed up to obtain the total drilling forces.

### 3.1.1 Formulation of cutting force model

In drilling composite materials, the cutting force prediction models can be developed using basic orthogonal and oblique cutting models. The difference between oblique and orthogonal cutting models is the inclination angle which is zero for the latter, as shown in Figure 3.1. In the orthogonal cutting, the tool approaches the workpiece with its cutting edge parallel to the uncut surface and at right angles to the direction of cutting. Thus, tool approach angle and cutting-edge inclination are zero. This type of cutting is also known as a two-dimensional cutting. In the oblique cutting, the cutting edge of the tool is inclined at an acute angle with the direction of tool feed, the chip begins disposed of at a certain angle. This type of cutting is also called three-dimensional cutting. Oblique cutting is more difficult to analyze and, in many cases, orthogonal cutting is assumed for simplifications reasons.

Caprino *et al.* [104, 105] conducted a series of experiments on the orthogonal cutting of fiberglass composites to find empirical models for cutting forces as shown below:

$$F_{hu} = 4.29 + 257.804 \times 10^{-0.019\gamma} t \quad (3.1a)$$

$$F_{vu} = 95.3 \times 10^{-0.02\gamma} \sqrt{t} \quad (3.1b)$$

where  $F_{hu}$  and  $F_{vu}$  are, respectively, the horizontal and vertical forces per unit of the width of the tool, calculated for situations in which the cutting direction is parallel to that of the fibers,  $\gamma$  is the rake angle and  $t$  is the cutting depth.

The relations (3.1a) and (3.1b) are only applicable to orthogonal cutting, a much more simpler process than drilling, and related to a definitively low-speed process in which the cutting lines run parallel to the direction of the reinforcing fibers. These conditions, however, are not met during drilling, a three-dimensional cutting process characterized by ongoing changes in cutting direction and very high cutting speeds varying at different points of the cutting lips.

An experimental study was performed to investigate the specific cutting force in various directions relative to the reinforcement of the FRP. Analysis of the finding has revealed that the horizontal force increases linearly with the depth of cut, that is:

$$F_{hu} = F_{ho} + K(\gamma)t \quad (3.2)$$

where  $F_{ho}$  is the intercept with  $y$  axis,  $K(\gamma)$  is the slope of the interpolating the experimental points and depends on rake angle and can be expressed as  $K(\gamma) = B \times 10^{-b\gamma t}$ .

Observing the percent difference between experimental and theoretical force values, it was found that the obtained formulas diverge from experimental values by a total average error of about 10%. Langella *et al.* [106] extended the scope of these relations as follows:

$$F_{hu} = A + B \times 10^{-b\gamma} t \quad (3.3a)$$

$$F_{vu} = B \times 10^{-a\gamma} \sqrt{t} \quad (3.3b)$$

where  $A$ ,  $B$ ,  $a$  and  $b$  are the coefficients that are to be determined, depend on the geometry of the drill and the cutting parameters. Based on the specific energy, that is activated during the drilling process, it is possible to obtain from Eq. (3.3a) and (3.3b), considering the transformation of rake angle in radiant, that the coefficients  $a = b = 1.089$ .

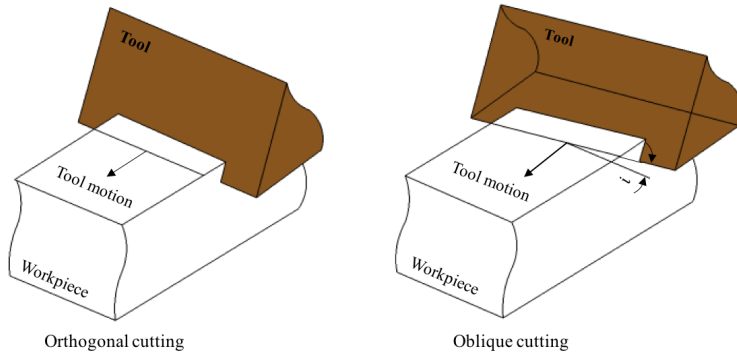


Figure 3.1. Cutting forces in orthogonal and oblique models.

To use these equations in the drilling process, the cutting depth  $t$  which is a function of feed rate  $f$  and drill point angle  $\varepsilon$  needs to be calculated. Regarding the fact that the drill point angle and inclination angle  $i$  vary along the cutting lips of the drill, an integration along the whole length of the cutting lips is required to calculate the total forces.

Figure 3.2 gives a schematic diagram of a twist drill geometry. In this figure,  $R$  is the drill bit radius,  $r_c$  is the chisel edge radius,  $t_c$  is the half the thickness of the chisel edge,  $\psi$  is the helix angle, and  $\varepsilon$  is the drill point angle. The elementary area  $dA$  is equal to the product  $dx(f/2)$ , where  $f$  is the feed rate and  $f/2$  is the cutting depth as there are two cutting lips. From geometry, one can derive:

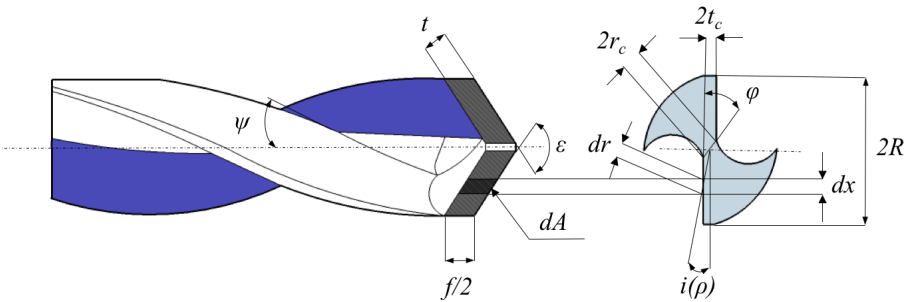


Figure 3.2. The nomenclature of the twist drill features.

$$dx = dr \cos i(\rho) = R d\rho \cos i(\rho) \quad (3.4)$$

where  $\rho$  is the normalized radius ( $\rho = r/R$ ) and  $i$  is inclination angle that varies depending on the radius along the cutting lip of the drill ( $\rho$ ).

From drill geometry,

$$t_c = \frac{r}{\sin(\varepsilon/2)} \sin i(\rho) \quad (3.5)$$

$$i(\rho) = \sin^{-1}\left(\frac{t_c}{\rho R} \sin(\varepsilon/2)\right) \quad (3.6)$$

$\cos i(\rho)$  can be approximated as follows:

$$\cos i(\rho) = \sqrt{1 - \sin^{-1} i(\rho)} = \sqrt{1 - \frac{t_c^2 \sin^2(\varepsilon/2)}{\rho^2 R^2}} \approx 1 - \frac{t_c^2 \sin^2(\varepsilon/2)}{2\rho^2 R^2} \quad (3.7)$$

and, therefore;

$$dx = \left(1 - \frac{t_c^2 \sin^2(\varepsilon/2)}{2\rho^2 R^2}\right) R d\rho \quad (3.8)$$

In order to obtain the resultant of all the tangential and vertical forces that are exerted on each cutting lip, an integration is performed in respect of the whole length of the cutting lip. By substituting the values of  $t$  and  $dx$  shown in Figure 3.2, we can derive:

$$F_h = \int_{\tau}^1 \left[ A + B \times 10^{-1.089\gamma} f / 2 \left(1 - \frac{t_c^2 \sin^2(\varepsilon/2)}{2\rho^2 R^2}\right) \right] R d\rho \quad (3.9a)$$

$$F_v = \int_{\tau}^1 \left[ B \times 10^{-1.089\gamma} \sqrt{f/2} \left(1 - \frac{t_c^2 \sin^2(\varepsilon/2)}{2\rho^2 R^2}\right) \right] R d\rho \quad (3.9b)$$

where the limits of integration are:

$$\text{lower: } \tau = \frac{r_c}{R} = \frac{t_c / \sin \varphi}{R} \quad (3.10a)$$

$$\text{Upper: } \frac{R}{R} = 1 \quad (3.10b)$$

and  $\varphi$  is the chisel edge angle.

The thrust force can be calculated from the resolved components of the vertical force ( $\delta F_r$  and  $\delta F_a$ ), which are perpendicular and parallel to the axis respectively as shown in Figure 3.3. The first component,  $\delta F_r$ , is offset by the equivalent and opposite component generated by the other cutting lip, while the second component,  $\delta F_a$ , generates a resistant thrust force. To obtain the thrust force value, ignoring the chisel edge section, it is enough to project  $\delta F_v$  in the direction of the axis. This mathematically given by:

$$F_{th}^L = 2 \int_{\tau}^1 B \times 10^{-1.089\gamma} \sqrt{f/2} \left( 1 - \frac{t_c^2 \sin^2(\varepsilon/2)}{2\rho^2 R^2} \right) R \sin(\varepsilon/2) d\rho \quad (3.11)$$

In Eq. (3.11) the rake angle  $\gamma$  is the sum of static  $\gamma_s$  and dynamic  $\gamma_d$  sections which vary depending on the radius ( $\rho$ ).

$$\gamma = \gamma_s + \gamma_d = \tan^{-1}\left(\frac{\rho \tan \psi}{\sin(\varepsilon/2)}\right) + \tan^{-1}\left(\frac{f}{2\pi\rho R}\right) \quad (3.12)$$

To simplify integration, an average value of the rake angle  $\gamma_m$  is defined as below:

$$\gamma_m = \frac{\int_{\tau}^1 \left( \tan^{-1}\left(\frac{\rho \tan \psi}{\sin(\varepsilon/2)}\right) + \tan^{-1}\left(\frac{f}{2\pi\rho R}\right) \right) d\rho}{\int_{\tau}^1 d\rho} \quad (3.13)$$

Finally, after simplification, the resultant adjusted thrust force exerted on the cutting lips will be:

$$F_{th}^L = 2B \times 10^{-1.089\gamma_m} \sqrt{f/2} G \quad (3.14)$$

where geometrical parameter  $G$  is defined as follows:

$$G = \int_{\tau}^1 \left( 1 - \frac{t_c^2 \sin^2(\varepsilon/2)}{2\rho^2 R^2} \right) R \sin(\varepsilon/2) d\rho \\ = \frac{\sin(\varepsilon/2) \left( 1 - \frac{r_c}{R} \right) (2r_c R - t_c^2 \sin(\varepsilon/2))}{2r_c} \quad (3.15)$$

and unknown parameter  $B$  is determined as follows:

$$B \times 10^{-1.089\gamma_m} = K_n \quad (3.16)$$

$K_n$  is the specific energy for the vertical force which can be determined by means of a single test as described in [106].

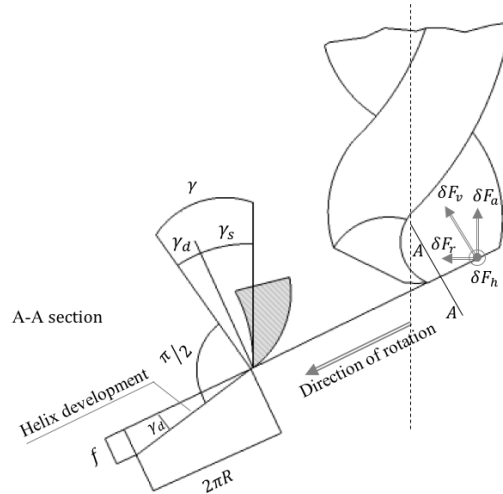


Figure 3.3. The forces exerted on main cutting lip and the drilling rake angle.

The same approach can be used to calculate the resultant thrust force exerted on the chisel edge because the rake angle of the chisel edge  $\gamma_c$  is assumed to be constant.

$$F_{th}^C = 2C \times 10^{-1.089\gamma_c} \sqrt{f} t_c \quad (3.17)$$

where the chisel edge rake angle is obtained as follows:

$$\gamma_c = -\tan^{-1}(\tan(\varepsilon/2) \cos \varphi) \quad (3.18)$$

In order to determine unknown constant  $C$ , the specific energy at the chisel edge  $K_{n,chisel}$  is used:

$$C \times 10^{-1.089\gamma_c} = K_{n,chisel} \quad (3.19)$$

The specific energies can be determined by a single drilling test. In this method, a drilling sample with a pilot hole is prepared. The diameter of the pilot hole is equal to the length of chisel edge and its depth is equal to the half thickness of the specimen. This sample is drilled and the experimental thrust forces in each section are measured. The values of the specific energies are determined as follows:

$$K_n = \frac{T_{exp}}{2G \sqrt{f}} \quad (3.20a)$$

$$K_n = \frac{T_{exp}^{chisel}}{\sqrt{2} t_c \sqrt{f}} \quad (3.20b)$$

The total thrust force will be the sum of the part values generated by cutting lips and the chisel edge.

## 3.2 Analytical model for delamination propagation

### 3.2.1 Physical model

In drilling composite laminates, the uncut thickness withstanding the drilling thrust force decreases as the drill approaches the exit plane. The laminate at the bottom may get separated from the interlaminar bond around the hole. At some points, the loading exceeds the interlaminar bond strength and delamination occurs.

A linear elastic fracture mechanics model for predicting the propagation of exit delamination due to the applied thrust force can be used. Several simplifications need to be made in order to perform the analysis. In this model, the laminate structure has a thickness of  $H$  consists of  $n$  number of plies. The drill has a radius of  $R$  and a circular crack of radius  $a$  pre-exists in the structure ahead of the drill point. It is assumed that the crack growth is coplanar and is confined to the plane of the crack. These are conditions that must be met in order for the LEFM theory to be applicable. When drilling a laminate, a crack initiates and spreads at the binder interface between the plies, which is a plane of symmetry for the material. Thus, the conditions for LEFM are met. The uncut thickness  $h$  ahead of the punch is modeled as an orthotropic circular plate clamped on its contour to the cut portion of the laminate, which is assumed to be rigid. As the drill cuts downwards, this plate is

deformed elastically by the action of the applied load  $F_{th}$  at its center. Crack propagation occurs when the elastic strain at its tip goes beyond a critical value.

The energy balance equation from LEFM is given by:

$$dU_d = dW - dU \quad (3.21)$$

where  $U$  is the stored strain energy,  $W$  is the external work done by the thrust force  $F_{th}$  as it moves a distance  $dw$ , and  $U_d$  is the strain energy absorbed by crack growth as expressed below:

$$dU_d = G_I \cdot dA \quad (3.22)$$

where  $dA$  is the change in the delamination area and  $G_I$  is the strain energy release rate per unit area in Mode I. It should be noted that only Mode I failure is assumed in this model although the actual failure mode induced by the drill cutting edges is in mixed mode situations.

Vaziri *et al.* [107] conducted a sensitivity analysis to evaluate the contribution of different fracture modes on propagation of drilling induced delamination. The results demonstrate that Mode I is the dominant mode while drill tool removes the material. Although Mode III contributes, it has a minor effect which can be neglected when comparing with mode I. Therefore, assumption of delamination crack propagation via mode I is appropriate for the case drilling.

Assuming the crack to be circular gives:

$$dU_d = G_I \cdot 2\pi a da \quad (3.23)$$

When the tool moves a distance  $dw$ , the work done by the tool is used up in deflecting the plate and in propagating the crack. Hence, for calculating the work done and stored strain energy, the deflection of plate  $w$  is to be determined. From classical laminated plate theory, when a circular plate is subjected to rotationally axisymmetric loads and the boundary conditions are also axisymmetric, as shown in Figure 3.4, the governing equation is [49]:

$$\nabla^2 D \nabla^2 w = q(r) \quad (3.24)$$

where  $q(r)$  is the distributed load acting in the same direction as  $w$ , and  $D$  is the bending rigidity of the plate as shown in Fig. If the bending rigidity  $D$  is constant throughout the plate, the plate equation can be simplified to:

$$\nabla^4 w = \frac{q(r)}{D} \quad (3.25)$$

Eq. (3.24) can be used for orthotropic plates by simple changing the isotropic bending rigidity  $D$  to the effective bending rigidity  $D'$  for orthotropic plates:

$$\nabla^4 w = \frac{1}{r} \frac{d}{dr} \left\{ r \frac{d}{dr} \left[ \frac{1}{r} \frac{d}{dr} \left( r \frac{dw}{dr} \right) \right] \right\} = \frac{q(r)}{D'} \quad (3.26)$$

where

$$D' = \frac{1}{8} (3D_{11} + 2D_{12} + 4D_{66} + 3D_{22}) \quad (3.27)$$

Where  $D_{ij}$  are the coefficients of the stiffness matrix of the plate in bending;

$$D_{ij} = \int_{-h/2}^{h/2} (\bar{Q}_{ij})_k z^2 dz = \sum_{k=1}^n (\bar{Q}_{ij})_k \frac{(h_k^3 - h_{k-1}^3)}{3}, \quad i,j = 1,2,6 \quad (3.28)$$

and  $\bar{Q}_{ij}$  are the elements of the transformed reduced stiffness matrix, see appendix A.

Eq. (3.25) has an analytical solution expressed as follows:

$$\begin{aligned} w &= w_h + w_p \\ w_h &= c_1 \ln(r) + c_2 r^2 \ln(r) + c_3 r^2 + c_4 \\ w_p &= \int \frac{1}{r} \int r \int \frac{1}{r} \int \frac{r p(r)}{D'} dr dr dr dr \end{aligned} \quad (3.29)$$

where  $c_1, c_2, c_3$  and  $c_4$  are constant coefficients,  $w_h$  is the general solution and  $w_p$  is the particular solution of Eq. (3.26). Applying the boundary conditions in different regions, the values of the coefficients can be determined.

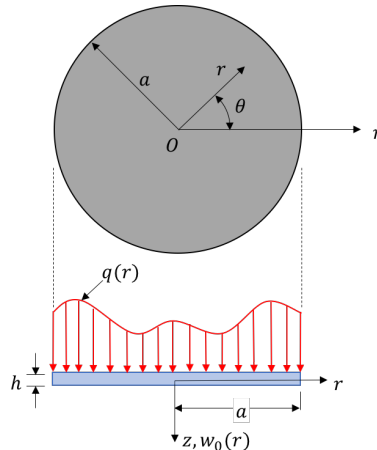


Figure 3.4. Axisymmetric circular plate subjected to rotationally axisymmetric loads.

### 3.2.2 Loading models

Drilling is a three dimensional and oblique cutting process. Geometrically, drilling is one of the most complex machining processes, mainly due to the complex geometry of the drills. Cutting speed, inclination angle, relief angle and rake angle vary along drill radius. All these factors make load function very complex. For simplification, three different profiles are assumed for the thrust force applied by the rotating drill bit to the laminate. A central concentrated force is considered in the first model, which is the sum of forces applied on cutting lips and chisel edge regions. For the second case, this resultant concentrated force is assumed to be distributed uniformly over the entire length of the drill bit. The idea behind considering a distributed load instead of a point load lies in the fact that the downward thrust during drilling does not come through the center of the drill as a concentrated load, rather it is spread out over the whole length of drill bit. And for the last case, different values of uniform load are considered for cutting lips and chisel edge regions based on

the mechanics of cutting described above. This model is anticipated to provide more accurate and rigorous results than the formers.

### 3.2.2.1 Central concentrated load

The schematic of delamination in the last uncut laminae of the workpiece, assuming a concentrated central load model is shown in Figure 3.5. In this figure,  $F_{th}$  is the thrust force exerted by a twist drill at the center of the plate,  $R$  is the drill radius and  $a$  is the radius of crack.

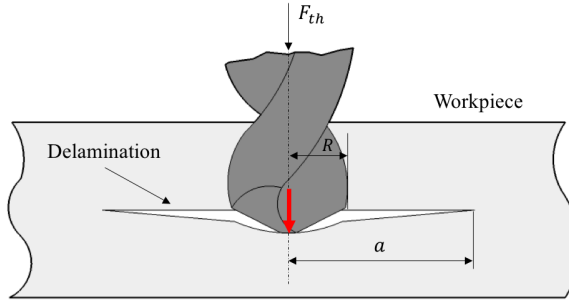


Figure 3.5. Concentrated central load model for delamination analysis.

According to the Eq. (3.26), for a circular plate with clamped edges subjected to a concentrated force at the center, the value of deflection can be obtained as (see Appendix B):

$$w(r) = \frac{F_{th}}{16\pi D'} \left[ 2r^2 \ln\left(\frac{r}{a}\right) + (a^2 - r^2) \right], \quad r \neq 0 \quad (3.30a)$$

$$w_0 = \frac{F_{th} a^2}{16\pi D'} \quad (3.30b)$$

where  $F_{th}$  is the sum of force applied on the cutting lips and chisel edge expressed as below:

$$F_{th} = F_{th}^L + F_{th}^C = k_L e^{-2.51\gamma_m} \sqrt{f} + k_c e^{-2.51\gamma_c} \sqrt{f} \quad (3.31)$$

and the constants  $K_L$  and  $K_C$  are obtained using the following equations:

$$k_L = \sqrt{2}BG \quad (3.32a)$$

$$k_c = 2Ct_c \quad (3.32b)$$

The stored strain energy is given by:

$$U = \pi D' \int_0^a \left[ \left( \frac{d^2 w}{dr^2} + \frac{1}{r} \frac{dw}{dr} \right)^2 - 2(1-\nu) \left( \frac{d^2 w}{dr^2} \times \frac{1}{r} \frac{dw}{dr} \right) \right] r dr \quad (3.33)$$

upon differentiating  $w$ , substituting in the above equation and integrating over crack radius, we obtain:

$$U = \frac{F_{th}^2 a^2}{32\pi D'} \quad dU = \frac{F_{th}^2 a}{16\pi D'} da \quad (3.34)$$

The work done is obtained as follows:

$$W = \int F_{th} dw = F_{th} \cdot w_0 = \frac{F_{th}^2 a^2}{16\pi D'} \quad dW = \frac{F_{th}^2 a}{8\pi D'} da \quad (3.35)$$

Substituting the Eq. (3.34), Eq. (3.35), and Eq. (3.22) in energy balance equation and solving for  $F_{th}$ , we get:

$$F_{cr}^C = \pi \sqrt{32G_{IC}D'} \quad (3.36)$$

Therefore, we have arrived at an expression for critical thrust force below which no delamination occurs. Eq. (3.36) indicates that the critical thrust force is a function of material properties and the uncut thickness alone and is independent of the drill geometry. In this equation, critical energy release rate for delamination in Mode I ( $G_{IC}$ ) is used for  $G_I$  because the crack propagation occurs when  $G$  reaches a critical value. The value of  $G_{IC}$  is assumed to be constant and to be a mild function of strain rate according to Saghizadeh and Dharan [108].

Eq. (3.36) is identical to Eq. (2.13) for a bending rigidity of  $D = Eh^3/12(1 - v^2)$ . This confirms that the delamination model presented here works for Hocheng's model for the special case of isotropic laminate although the expressions have been developed for a multi-directional laminate.

It is noted that, this approach in which the limiting condition for propagation of a single crack is postulated is a simplification of the complex processes occurring during the drilling process. As is typical in drilling of composite laminates, however, multiple fracture modes are usually observed including fiber debonding, microcrack growth, and nonlinear deformation modes such as bulging. Even so, the fracture mechanics approach provides a lower bound for the critical thrust force for damage propagation and is useful for incorporating into algorithms for intelligent manufacturing systems for machining composite materials.

Relating feed rate with thrust force is important because once this relation is established, one can directly program feed rate into machining commands such that delamination is prevented. This will eliminate the need to monitor thrust force. Substituting Eq. (3.31) in critical thrust force equation, i.e. Eq. (3.36), we obtain corresponding critical feed rate, given by the following expression:

$$f_{cr}^C = \frac{32\pi^2 G_{IC} D'}{\chi^2} \quad (3.37)$$

where the constant  $\chi$  is given by:

$$\chi = k_L e^{-2.51\gamma_m} + k_c e^{-2.51\gamma_c} \quad (3.38)$$

In order to produce delamination-free holes in composite laminates, feed rate must be set below the critical value. One approach will be to drill the composite laminate at a very slow feed rate so that the critical feed rate and corresponding thrust is never exceeded. Nevertheless, this will be very inefficient and may cause thermal damage to the drilled laminate. Our goal is to drill in a time-optimal fashion while preventing delamination.

In the expression for critical feed rate, the equivalent bending rigidity is a function of the uncut thickness. Figure 3.6 illustrates the variation of critical feed rate with uncut depth under tool. As the drill nears the exit side, the critical feed decreases to a small finite value. A novel approach, therefore, will be to drill as fast as practically permissible in the beginning and then progressively decrease the feed rate as the drill tool approaches exit. More specifically, if  $F_{cr}^{(1)}$  corresponds to delamination at the first ply from the bottom,  $F_{cr}^{(2)}$  to the second ply,  $F_{cr}^{(3)}$  to the third ply, then the corresponding feed rates are  $f_{cr}^{(1)}$ ,  $f_{cr}^{(2)}$ ,  $f_{cr}^{(3)}$ , respectively. To manufacture holes without delamination in time-optimal manner, it is necessary to reduce the feed rate to  $f_{cr}^{(3)}$  just before reaching the third ply, to  $f_{cr}^{(2)}$  before reaching the second ply, and to  $f_{cr}^{(1)}$  before the bottom-most ply. This will result in a delamination-free hole. In actual implementation of the strategy, the feed rate upon approach to the exit can be decreased discretely in a staircase manner or in a continuous manner.

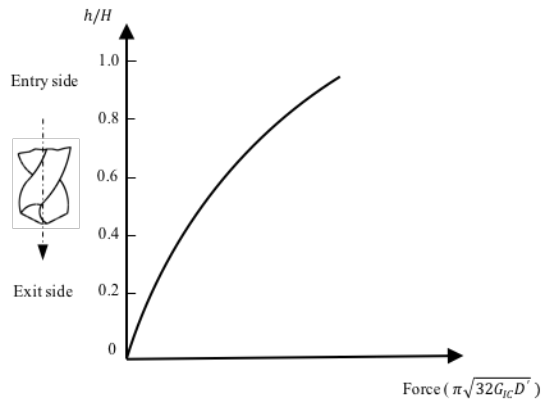


Figure 3.6. Correlation between critical feed rate and uncut depth under drill tool.

### 3.2.2.2 Equivalent uniformly distributed load

The schematic of delamination in the last uncut laminae of the workpiece, assuming an equivalent uniformly distributed load model is shown in Figure 3.7. In this figure,  $F_{th}$  is the total thrust force acting on the laminate and  $q_0 = \frac{F_{th}}{\pi R^2}$  is the equivalent uniform pressure.

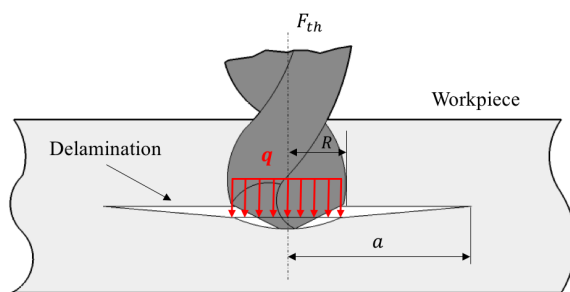


Figure 3.7. Equivalent uniformly distributed load model for delamination analysis.

For a circular laminate with clamped edges subjected to a uniformly distributed load over the central circular area of radius  $R$ , the value of deflection can be calculated as (see Appendix B):

for  $0 < r < R$

$$w_1(r) = \frac{F_{th}}{64\pi D'} \left[ \left( 4a^2 - 3R^2 + 4R^2 \ln\left(\frac{R}{a}\right) \right) - 2r^2 \left( \frac{R^2}{a^2} - 4 \ln\left(\frac{R}{a}\right) \right) + \frac{r^4}{R^2} \right] \quad (3.39a)$$

for  $R < r < a$

$$w_2(r) = \frac{F_{th}}{32\pi D'} \left[ (2a^2 + R^2) - r^2 \left( 2 + \frac{R^2}{a^2} - 4 \ln\left(\frac{r}{a}\right) \right) + 2R^2 \ln\left(\frac{r}{a}\right) \right] \quad (3.39b)$$

The external work done will be:

$$\begin{aligned} W &= \int dW = \int_0^r \int_0^{2\pi} q w_1(r) r dr d\theta = \frac{F_{th}}{\pi R^2} \int_0^r \int_0^{2\pi} w_1(r) r dr d\theta \\ &= \frac{F_{th}^2}{32\pi D'} \left[ 4a^2 - \frac{8R^2}{3} + 4R^2 \ln\left(\frac{R}{a}\right) - \frac{R^4}{a^2} + 4R^2 \ln\left(\frac{R}{a}\right) + \frac{R^2}{3} \right] \end{aligned} \quad (3.40a)$$

$$dW = \frac{F_{th}^2}{64\pi D'} \left[ 8 - 8 \frac{R^2}{a^2} + 2 \frac{R^4}{a^4} \right] \quad (3.40b)$$

and the stored strain energy is:

for  $0 < r < R$

$$\begin{aligned} U_1 &= \pi \int_0^R D' \left[ \left( \frac{d^2 w_1}{dr^2} + \frac{1}{r} \frac{dw_1}{dr} \right)^2 \right] r dr \\ &= \frac{F_{th}^2}{64\pi D'} \left[ \frac{2R^2}{3} - \frac{R^4}{a^2} + \frac{R^6}{2a^4} - \frac{4R^4}{a^2} \ln\left(\frac{R}{a}\right) + 4R^2 \ln\left(\frac{R}{a}\right) + 8R^2 \left( \ln\left(\frac{R}{a}\right) \right)^2 \right] \end{aligned} \quad (3.41a)$$

for  $R < r < a$

$$\begin{aligned} U_2 &= \pi \int_R^a D' \left[ \left( \frac{d^2 w_2}{dr^2} + \frac{1}{r} \frac{dw_2}{dr} \right)^2 \right] r dr \\ &= \frac{F_{th}^2}{64\pi D'} \left[ 2a^2 - 2R^2 + \frac{R^4}{2a^2} - \frac{R^6}{2a^4} - 8R^2 \left( \ln\left(\frac{R}{a}\right) \right)^2 + \frac{4R^4}{a^2} \ln\left(\frac{R}{a}\right) \right] \end{aligned} \quad (3.41b)$$

hence,

$$U = U_1 + U_2 \quad (3.41c)$$

$$dU = \frac{F_{th}^2 a}{64\pi D'} [4 - 4 \frac{R^2}{a^2} + \frac{R^4}{a^4}] \quad (3.41d)$$

Therefore, the critical thrust force and corresponding feed rate at the onset of crack propagation can be calculated as below:

$$F_{cr}^U = \frac{\pi \sqrt{32G_{IC}D'}}{1 - 1/2 s^2} \quad (3.42)$$

$$f_{cr}^U = \frac{32\pi^2 G_{IC} D'}{\chi^2 (1 - 1/2 s^2)^2} \quad (3.43)$$

where  $s = R/a$ .

The comparison of  $f_{cr}^A$  and  $f_{cr}^U$  in Eqs. (3.37) and (3.43) gives:

$$\frac{f_{cr}^U}{f_{cr}^A} = \frac{1}{(1 - 1/2 s^2)^2} \geq 1 \quad (3.44)$$

Eq. (3.44) indicates that higher values of feed rate are allowed when assuming the load is distributed over the whole length of drill bit rather than considering the load as a point load. In other words, by designing drill bits that distribute the load, high productivity can be achieved in delamination-free drilling of composite laminates.

Maximum feed rate in the case of no delamination, ( $a = R$ ), will be:

$$f_{max}^U = \frac{128\pi^2 G_{IC} D'}{\chi^2} \quad (3.45)$$

Which is four times greater than the maximum allowed feed rate for the central concentrated load model.

### 3.2.2.3 Uniformly distributed loads

According to the mechanics of cutting discussed above, the schematic of the thrust load exerted on the last uncut layers is shown in Figure 3.8. In this figure,  $F_{th}^L$  and  $F_{th}^C$  are concentrated forces acting on the cutting lips and chisel edge regions, respectively. Assuming the forces are distributed uniformly in these regions gives:

$$F_{th}^L = q_L \pi (R^2 - r_c^2) \quad (3.46a)$$

$$F_{th}^C = q_c \pi r_c^2 \quad (3.46b)$$

Here it is shown that the chisel edge has a greater contribution to the thrust force than the cutting lips according to the results of Won and Dharam [65]. They observed that the thrust force due to the chisel edge is 40% the total force when feed rate is low and 60% when feed rate is high during drilling of composite laminates.

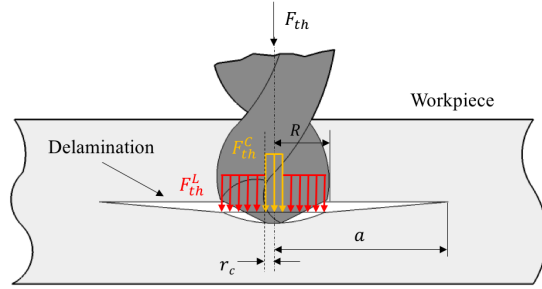


Figure 3.8. Uniformly distributed loads model for delamination analysis.

Defining  $T_1$  and  $T_2$  as concentrated forces associated with  $(q_L)$  and  $(q_c - q_L)$  respectively, yields:

$$T_1 = q_L \pi R^2 \quad (3.47a)$$

$$T_2 = (q_c - q_L) \pi r_c^2 \quad (3.47b)$$

This loading system (Figure 3.9) is statically equivalent to the loading system of Figure 3.8.

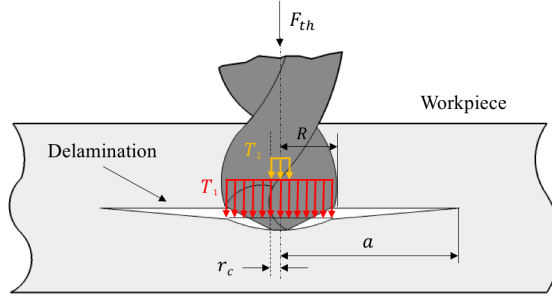


Figure 3.9. Equivalent loading system of Figure 3.8

let:

$$T_c = \alpha T_L \quad (3.48)$$

therefore:

$$T_1 = \frac{1}{(1 + \alpha) + (1 - \tau^2)} T = JT \quad (3.49a)$$

$$T_2 = \left[ 1 - \frac{1}{(1 + \alpha) + (1 - \tau^2)} \right] T = (1 - J)T \quad (3.49b)$$

where  $T$  is the total thrust force,  $J$  is a constant coefficient and  $\tau$  is defined as Eq. (3.10a).

The outer and inner deflection of the plate due to  $T_1$  is given by:

for  $0 < r < R$ :

$$w_{11}(r) = \frac{T_1}{64\pi D'} \left[ \left( 4a^2 - 3R^2 + 4R^2 \ln \left( \frac{R}{a} \right) \right) - 2r^2 \left( \frac{R^2}{a^2} - 4 \ln \left( \frac{R}{a} \right) \right) + \frac{r^4}{R^2} \right] \quad (3.50a)$$

for  $R < r < a$ :

$$w_{12}(r) = \frac{T_1}{32\pi D'} \left[ 2a^2 + R^2 - r^2 \left( 2 + \frac{R^2}{a^2} \right) + 2R^2 \ln\left(\frac{r}{a}\right) + 4r^2 \ln\left(\frac{r}{a}\right) \right] \quad (3.50b)$$

the work done is:

$$\begin{aligned} W_1 &= \int dW_1 = \int_0^r \int_0^{2\pi} q w_{11}(r) r dr d\theta \\ &= \frac{T_1}{\pi R^2} \int_0^r \int_0^{2\pi} w_{11}(r) r dr d\theta \\ &= \frac{T_1^2}{64\pi D'} \left[ 4a^2 - \frac{8R^2}{3} + 4R^2 \ln\left(\frac{R}{a}\right) - \frac{R^4}{a^2} + 4R^2 \ln\left(\frac{R}{a}\right) \right] \end{aligned} \quad (3.51a)$$

$$dW_1 = \frac{T_1^2 a}{64\pi D'} \left[ 8 - \frac{8R^2}{a^2} + \frac{2R^4}{a^4} \right] da \quad (3.51b)$$

and the stored strain energy is:

for  $0 < r < R$

$$\begin{aligned} U_{11} &= \pi \int_0^R D' \left[ \left( \frac{d^2 w_{11}}{dr^2} + \frac{1}{r} \frac{dw_{11}}{dr} \right)^2 \right] r dr \\ &= \frac{T_1^2}{64\pi D'} \left[ \frac{2R^2}{3} - \frac{R^4}{a^2} + \frac{R^6}{2a^4} - \frac{4R^4}{a^2} \ln\left(\frac{R}{a}\right) + 4R^2 \ln\left(\frac{R}{a}\right) + 8R^2 \left( \ln\left(\frac{R}{a}\right) \right)^2 \right] \end{aligned} \quad (3.52a)$$

for  $R < r < a$

$$\begin{aligned} U_{12} &= \pi \int_R^a D' \left[ \left( \frac{d^2 w_{12}}{dr^2} + \frac{1}{r} \frac{dw_{12}}{dr} \right)^2 \right] r dr \\ &= \frac{T_1^2}{64\pi D'} \left[ 2a^2 - 2R^2 + \frac{R^4}{2a^2} - \frac{R^6}{2a^4} - 8R^2 \left( \ln\left(\frac{R}{a}\right) \right)^2 + \frac{4R^4}{a^2} \ln\left(\frac{R}{a}\right) \right] \end{aligned} \quad (3.52b)$$

hence,

$$U_1 = U_{11} + U_{12} \quad (3.53c)$$

$$dU_2 = \frac{T_1^2 a}{64\pi D'} \left[ 4 - 4 \frac{R^2}{a^2} + \frac{R^4}{a^4} \right] da \quad (3.53d)$$

Similarly, the outer and inner deflection of the plate due to  $T_2$  is:

for  $0 < r < R$ :

$$w_{21}(r) = \frac{T_2}{32\pi D'} \left[ 4a^2 - 3r_c^2 - 4r_c^2 \ln\left(\frac{r_c}{a}\right) - 2r^2 \left( \frac{r_c^2}{a^2} - 4 \ln\left(\frac{r_c}{a}\right) \right) + \frac{r^4}{r_c^2} \right] \quad (3.54a)$$

for  $R < r < a$ :

$$w_{22}(r) = \frac{T_2}{32\pi D'} \left[ 2a^2 + r_c^2 - r^2 \left( 2 + \frac{r_c^2}{a^2} \right) + 2r_c^2 \ln\left(\frac{r}{a}\right) + 4r^2 \ln\left(\frac{r}{a}\right) \right] \quad (3.54b)$$

the work done is:

$$\begin{aligned} W_2 &= \int dW_2 = \int_0^r \int_0^{2\pi} q w_{21}(r) r dr d\theta \\ &= \frac{T_2}{\pi R^2} \int_0^r \int_0^{2\pi} w_{21}(r) r dr d\theta \\ &= \frac{T_2^2}{64\pi D'} \left[ 4a^2 - \frac{8r_c^2}{3} + 4r_c^2 \ln\left(\frac{r_c}{a}\right) - \frac{r_c^4}{a^2} + 4r_c^2 \ln\left(\frac{r_c}{a}\right) \right] \end{aligned} \quad (3.55a)$$

$$dW_2 = \frac{T_2^2 a}{64\pi D'} \left[ 8 - \frac{8r_c^2}{a^2} + \frac{2r_c^4}{a^4} \right] da \quad (3.55b)$$

and the stored strain energy is:

for  $0 < r < R$

$$\begin{aligned} U_{21} &= \pi \int_0^{r_c} D' \left[ \left( \frac{d^2 w_{21}}{dr^2} + \frac{1}{r} \frac{dw_{21}}{dr} \right)^2 \right] r dr \\ &= \frac{T_2^2}{64\pi D'} \left[ \frac{2r_c^2}{3} - \frac{r_c^4}{a^2} + \frac{r_c^6}{2a^4} \right. \\ &\quad \left. - \frac{4r_c^4}{a^2} \ln\left(\frac{r_c}{a}\right) + 4r_c^2 \ln\left(\frac{r_c}{a}\right) + 8r_c^2 \left( \ln\left(\frac{r_c}{a}\right) \right)^2 \right] \end{aligned} \quad (3.56a)$$

for  $R < r < a$

$$\begin{aligned} U_{22} &= \pi \int_{r_c}^a D' \left[ \left( \frac{d^2 w_{22}}{dr^2} + \frac{1}{r} \frac{dw_{22}}{dr} \right)^2 \right] r dr \\ &= \frac{T_2^2}{64\pi D'} \left[ 2a^2 - 2r_c^2 + \frac{r_c^4}{2a^2} - \frac{r_c^6}{2a^4} - 8r_c^2 \left( \ln\left(\frac{r_c}{a}\right) \right)^2 \right. \\ &\quad \left. + \frac{4r_c^4}{a^2} \ln\left(\frac{r_c}{a}\right) \right] \end{aligned} \quad (3.56b)$$

hence, the total strain energy is:

$$U_2 = U_{21} + U_{22} \quad (3.56c)$$

$$dU_2 = \frac{T_2^2 a}{64\pi D'} \left[ 4 - 4 \frac{r_c^2}{a^2} + \frac{r_c^4}{a^4} \right] da \quad (3.56d)$$

Using the method of superposition, the energy balance equation can be expressed as follows:

$$G_C 2\pi a da = (dW_1 - dU_1) + (dW_2 - dU_2) \quad (4.57)$$

Finally, the critical thrust force and feed rate at the onset of crack propagation can be calculated as below:

$$F_{cr}^S = \frac{\pi \sqrt{32G_{IC}D'}}{\sqrt{\left(J^2 \left(1 - \frac{1}{2}s^2\right)^2 + (1-J)^2 \left(1 - \frac{1}{2}\tau^2 s^2\right)^2\right)}} \quad (3.58a)$$

$$f_{cr}^S = \frac{32\pi^2 G_{IC} D'}{\chi^2 \left(J^2 \left(1 - \frac{1}{2}s^2\right)^2 + (1-J)^2 \left(1 - \frac{1}{2}\tau^2 s^2\right)^2\right)} \quad (3.58b)$$

To avoid delamination, the thrust force and feed rate should not exceed  $F_{cr}^S$  and  $f_{cr}^S$ , respectively.

Eq. (3.58a) indicates that the critical thrust is a function of chisel edge radius,  $r_c$ . To evaluate the effect of chisel edge radius on the critical thrust force value, the critical thrust force predicted by Eq. (3.58a) is depicted in Figure 3.10 for various drill radius to crack size ratios. As can be seen, for all values of  $s$  and  $\alpha$  (thrust force on chisel edge to thrust force on cutting lips ratio), at about  $\tau = 0.6$  the crack can sustain the largest value of thrust force before propagation. In other words, by controlling drill geometrical parameters such as chisel edge radius, it is possible to use a higher feed rate to drill the composite materials without causing delamination.

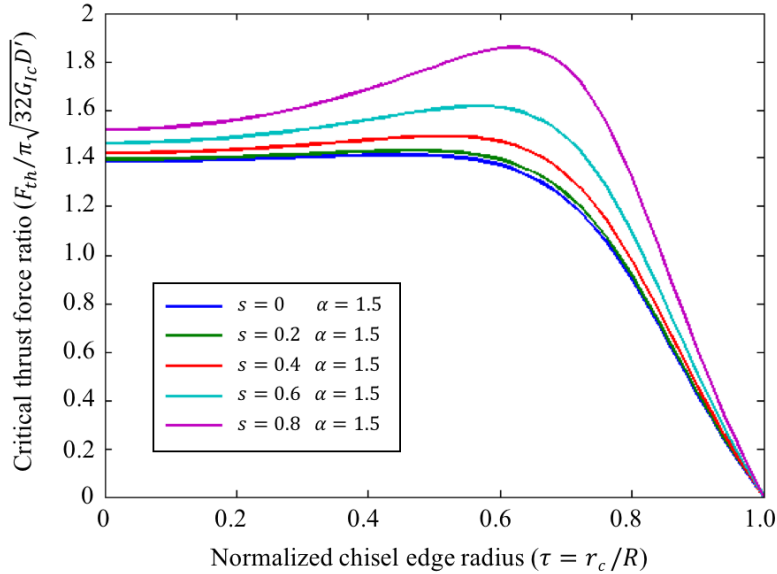


Figure 3.10. Effect of chisel edge radius on critical thrust force predicted by Eq. (3.58a).

### 3.3 Experimental validation and comparison with existing models

To evaluate and verify the models introduced in previous sections, a comparison of the respective predicted thrust forces with experimental data has been conducted. To this end, it is necessary to choose the delamination results cited in a particular article so that the predicted thrust forces from

different delamination models can be compared. In view of the clarity of the results presented in Ref. [46] and based on the fact that other models can be used to predict thrust force for the laminate layup in this article, a symmetric laminate with the layup sequence  $[45, 90, -45, 0]_{6s}$  was used. The material investigated is Fibredex 914/T300 (Hexcel) carbon/epoxy composite laminate, and the material properties are given in Table 3.1. Seven models have been considered for comparison, namely; Hocheng model [42], Upadhyay model [45], Lachaud model [46], Zhang model [47], Gururaja model [48], presented equivalent uniform load model, and presented uniform load models.

*Table 3.1. Material properties of 914/T300 carbon/epoxy composite laminate.*

$E_L$ (GPa)	$E_T$ (GPa)	$G_{LT}$ (GPa)	$v_{LT}$	$G_{IC}$ (J/m <sup>2</sup> )	Ply thickness (mm)
144	8.7	4.14	0.3	150	0.125

Based on the experimental data in Ref [46], the bottom six plies have been chosen to be studied. The values of critical thrust forces for these plies are computed and are listed in Table 3.2 and shown graphically in Figure 3.11. It should be noted that all expressions described in this chapter for critical thrust force and feed rate depend on the lay-up of the uncut laminate underneath the drill bit. As drilling progresses, the layup underneath the drill changes and the analysis needs to be performed again to obtain a predicted critical thrust and feed values corresponding to the uncut thickness of the laminate.

Figure 3.11 illustrates the behavior of the predicted critical thrust forces as the ply number increases. In this figure, the dashed line indicates the experimental observations of the critical thrust. When the number of uncut plies is less than or equal to two, all the analytical models make a fairly good estimate of the critical thrust forces. The predictions made by the models are slightly higher than the experimentally measured values apart from Zhang model which gives conservative estimates. As the ply number increases to three, Hocheng, Upadhyay and Zhang models as well as proposed uniform model are no longer close to the experimental value. The predicted values by Lachaud model is above the experimental measured values, showing the inadequacy of his model in delamination free drilling.

The model formulated by Gururaja *et al.* predicted thrust force satisfactorily well. The results from the proposed uniform loads model are in good agreement with their results. Both models are yielding closest to the experimental values, specifically, for ply number 3, 4 and 6. The predicted values by the proposed uniform loads model when the number of uncut plies are four and six are higher than the experimental values by 13% and 0.4% respectively, whereas, the predicted value is lower than the experimental value for three uncut plies by 20%. Thus, the uniform loads model is proved to be satisfactory.

Table 3.2. Variation of critical thrust force with ply number.

Ply number	Experimental observations	Hocheng model	Upadhyay model	Lachaud model	Zhang model	Gururaja model	Uniform load	Uniform loads
	$P_c$ (N)	$F_{th}$ (N)	$F_{th}$ (N)	$F_{th}$ (N)	$F_{th}$ (N)	$F_{th}$ (N)	$F_{th}^U$ (N)	$F_{th}^S$ (N)
6	1040	513.4	548.82	1190	365.50	1033.87	634	1044
5	835	390.5	417.5	840	223.86	633.19	482	639
4	390	279.5	298.74	640	154.86	437.74	345	442
3	320	181.5	194.04	410	89.33	252.66	224	255
2	80	98.8	105.62	200	51.38	145.30	122	147
1	35	34.93	37.34	80	18.45	52.18	43	53

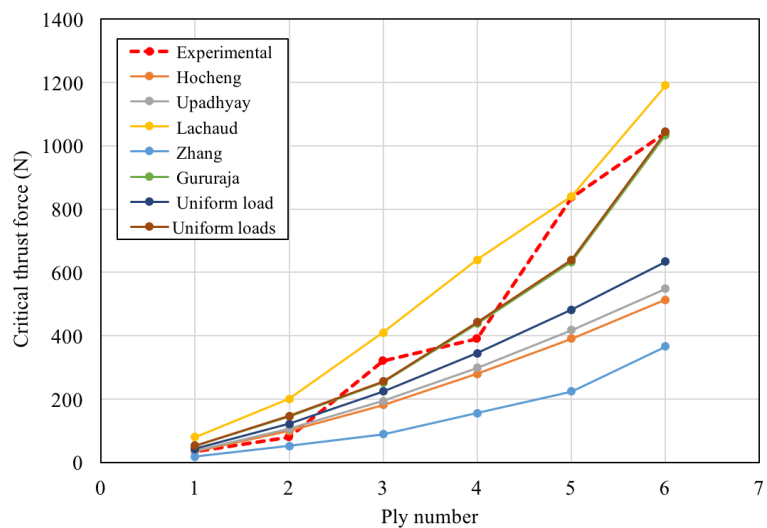


Figure 3.11. Critical thrust force,  $F_{th}$ , varying with the ply number,  $n$ , from the bottom side.

# CHAPTER 4

## 4 EXPERIMENTAL PROCEDURE

To achieve the objectives of the current research, two series of drilling and post-drilling mechanical experiments were designed and carried out; GFRP composites were drilled and then compression tested to evaluate their residual compressive strength, nano filled GFRP composites were drilled and then bending tested to determine their residual bending strength. In this chapter, material preparation, experimental setup, experimental procedure, measurement techniques, damage inspection, and detailed information of statistical methods for data analysis used in this study are presented.

### 4.1 Material preparation

Two materials were studied in the present investigation: (1) E-glass/epoxy composites, (2) E-glass fiber-epoxy composites reinforced with functionalized multi-walled carbon nanotubes.

#### 4.1.1 GFRP composites

The composite specimens for compression tests were manufactured by hand lay-up method from Araldite LY556 epoxy resin reinforced with high strength E-glass woven fibers. Table 4.1 summarizes the properties of the resin and fibers used in the present experiments. The GFRP laminates were approximately 6 mm thick, comprising 12 plies, and had an approximately 50% fiber volume fraction.

*Table 4.1. Properties of matrix and fibers used for GFRP composites.*

	Density (g/cm <sup>3</sup> )	Tensile strength (MPa)	Compressive strength (MPa)	Young's Modulus (GPa)
Epoxy resin	1.20	80	195	2.7
E-glass fiber	2.55	2150	4500	74

#### 4.1.2 Nano filled GFRP composites

The composite specimens used for bending experiments were made using epoxy resin, glass fibers, and carbon nanotubes. The epoxy was a two-part epoxy resin; part A: an epoxy polymer based on bisphenol A/epichlorohydrin derived liquid epoxy resin (Epon resin 828), and part B: cycloaliphatic amine curing agent (F205). High strength E-glass woven fibers with a density of 2.6 g/cm<sup>3</sup> and Young's modulus of 72 GPa were also used as reinforcements in composites. Functionalized multi-walled carbon nanotubes (COOH-MWCNTs) containing 1.2 wt. % carboxyl groups (-COOH) were manufactured using catalytic chemical vapor deposition technique. These CNTs had an average diameter of 10 nm, an average length of several microns and carbon purity of >95%. The properties of carbon nanotubes are given Table 4.2.

The functionalized MWCNTs at four different weight fractions, i.e. 0, 0.1, 0.5 and 1s wt. %, were mixed with epoxy resin using a high-speed mechanical stirrer for 3 h to ensure chemical interaction between the functional groups on the surface of the MWCNTs and the resin chains. In order to obtain a uniform dispersion of the CNTs and prevent the agglomerations, the mixture was then placed in an ultrasound bath at 150 kW/cm<sup>2</sup> intensity and 5 μm amplitude for half an hour. Cycloaliphatic amine curing agent was then added to the modified resin and mixed by a mechanical stirrer at 3000 rpm for 1 h. The mixture was then placed in a vacuum oven at 60 °C for 15 min for degasification to remove entrapped air bubbles.

Nano filled E-glass/epoxy composite laminates were manufactured by using vacuum assisted hand lay-up technique. Twelve layers of E-glass fabric were used to fabricate laminates with a [0,90]<sub>6s</sub> layup. Curing was carried out in the autoclave at 60 °C/1MPa. The fabricated composite plate had an average thickness of 2.6±0.1 mm and a fiber volume fraction of 55%.

*Table 4.2. Properties of functionalized multi-walled carbon nanotubes.*

Diameter	Length	-COOH content	Purity	Ash	Specific surface area	Electrical conductivity
5-50 nm	50~ μm	2.56 wt.%	>95%	<1.5%	233 g/m <sup>2</sup>	10 <sup>2</sup> s/cm

## 4.2 Experimental setup

The experimental setup consists of a machine tool, a force-torque dynamometer, two charge amplifiers, connecting cables, an A/D converter, a PC, a fixture, a vacuum cleaner, drills, specimens, a scanning electron microscope, acoustic emission device, and data acquisition system.

### 4.2.1 Drilling tests

The laboratory equipment layout for dry drilling is shown in Figure 4.1. The machine tools used in the experiments were a Cortini HS 644P vertical machining center equipped with a PC-based controller. The machining center is a 5-axis system and capable of providing spindles with a power of up to 25.8 kW and a maximum speed of 36,000 rpm. The drive train for each axis of X-Y table consists of an AC motor coupled with a ball screw which transmits linear displacement of the bed through the ball screw nut. The system controller has positioning accuracy up to 0.003 mm for the three axes and a programmable feed resolution of 0.1 mm/min in the Z axis.

Equipment and setup validation tests were performed prior to commencement of experiments to ensure proper functioning and calibration of all systems. The holes were drilled at the center of the specimens, and no coolant was used. Tests were run individually and in random order and each test was replicated three times to ensure repeatability. Since the air-borne chips produced during the cutting of composite materials are harmful to humans as well as to the machine tool, a vacuum dust collection system was installed near the table to suck away the dust-like chips.



*Figure 4.1. Experimental setup of drilling.*

#### 4.2.2 Drill tools

In this investigation, high-speed steel twist drill bits were used to conduct the drilling experiments. Twist drill is the most commonly used cutting tool in drilling operations, which has two identical cutting edges designed to produce identical chips. Twist drills have a high length to diameter ratio, and they are composed of three components, shank, body, and drill point. Even though twist drills are composed of many geometric entities, point angle, clearance angle, helix angle, web thickness, and chisel edge angle are mainly considered quantities in the analysis of drilling operation. Basic geometric values of twist drill bits used are given in Table 4.3 and its optical image is shown in Figure 4.2.

High-speed steel drill tools wear quite rapidly when machining FRPs because of the high abrasiveness of the fibers, and their use generally becomes impractical. To avoid the effect of tool wear, each of the five holes was made using a new drill bit, and the tests were run without coolant.

*Table 4.3. Specification of the drill bits used in the experiments.*

Family	Standard	Tool material	Nominal Diameter	Point angle	Helix angle	Flutes	Flute length
2462-Guhring	Din 340	HSS	4-5	130	30	2	87

\* All lengths are in mm and all angles are in degree.



*Figure 4.2. HSS twist drill bit used in the experiments.*

#### 4.2.3 Drilling fixture

A custom modular adjustable fixture was designed and fabricated from aluminum to hold and consistently locate the specimen in the drilling machine. The fixture is adjustable so that a

specimen of various sizes from 20 to 180 mm in width can be accommodated. The fixture has a capacity of accommodating a specimen with a maximum thickness of 40 mm and length of the specimen can vary as needed. Figure 4.3 shows the fixture used for drilling tests.

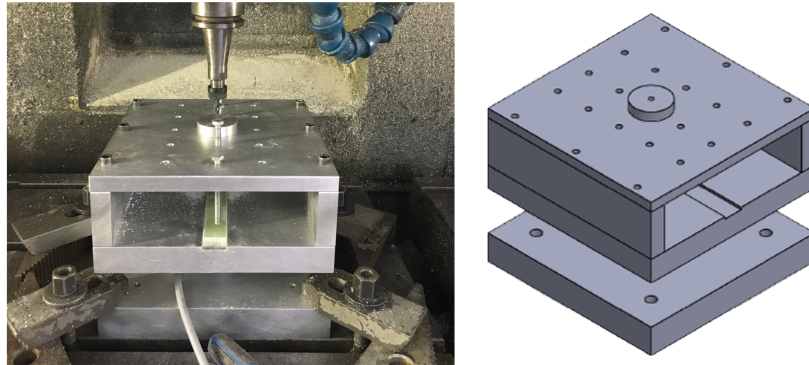


*Figure 4.3. Fixture of experimental drilling tests.*

#### 4.2.4 Drilling force measurement

One of the essential parts of the experiments is to measure the thrust force developed during the drilling process. There are different types of drilling dynamometers which serve the purpose of thrust force measurement, such as strain-gauge and piezoelectric dynamometers. In the current experiments, both types were used.

For drilling tests conducted in Bologna laboratory, a two-channel Kistler 9271A dynamometer was used to measure the thrust force. The dynamometer was fixed on the machine tool table by two clamps at opposite ends. The signals were amplified by two Kistler charge amplifiers. Voltage signals traveled through a commercial analog to digital I/O board, located inside a computer, where the signals were converted to the digital domain. A customized software program was used to control the sampling frequency during the experiments and to view the output signals, as shown in Figure 4.4. Voltage data was recorded from the data acquisition system and post processed for future analysis.

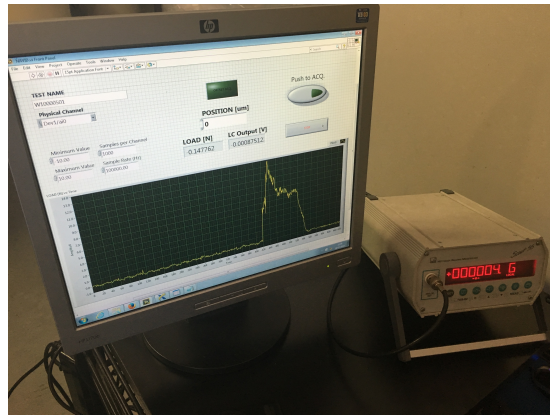


*Figure 4.4. Measurement of drilling thrust force.*

For the drilling tests conducted in the Hanger laboratory, an HBM U2A load cell was clamped to the back side of the drilling fixture to measure the thrust force. A load cell with a maximum capacity of 200 kN was selected to ensure achieving sensible results. The strain gauge load cells measure the deformation as a change in electrical resistance, which is a measure of the strain and hence the applied forces. The electrical signal output was amplified and then fed into an analog to digital i/o board with a sampling rate of 1 kHz and resolution of 16 bit.

#### 4.2.5 Post-drilling mechanical test

After each series of drilling tests is completed, the drilled specimens were subjected to additional testing to determine the impact of drilling induced delamination on their residual mechanical properties. These tests comprise quasi-static compression test and three-point bending test. The objective is to determine the residual strength of composite laminates when drilled under different machining conditions.

##### 4.2.5.1 Compression test

The compression experiments were conducted on an INSTRON 8033 testing machine. Specimens of standard size 100 mm × 150 mm were cut according to the ASTM Standard D7137/D7137M [109]. The instrumentation and loading arrangement of the specimens in buckling test rig is shown in Figure 4.5. The compression fixture composes adjustable retention plates to support the specimen edges and inhibit buckling when the specimen is end-loaded. The side supports are knife edges, which provide no restraint to local out-of-plane rotation. The top and bottom supports provide no clamp-up but provide some rotational restraint due to the fixture geometry. The top plate and slide plate that are not directly attached to the lower portion of the fixture, slip over the top edge of the specimen. The side plates are sufficiently short to ensure that a gap between the side rails and the top plate is maintained during the test. All specimens were loaded at a constant speed of 1.5 mm until failure.

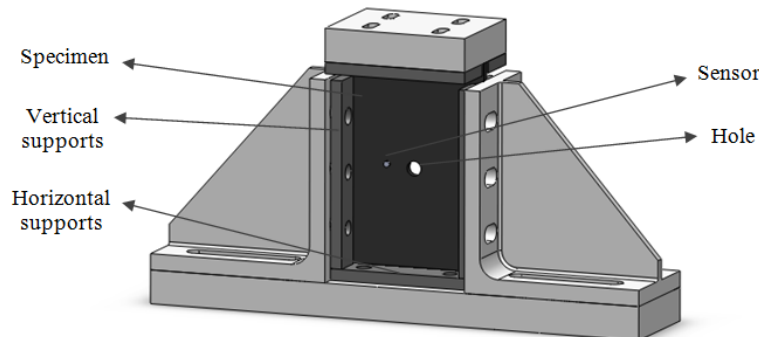


Figure 4.5. Schematic of test specimen and instrumentation for compression test.

##### 4.2.5.2 Bending test

Three-point bending tests were carried out on an INSTRON 8033 testing machine. The setup of these three-point bending tests was in accordance to ASTM D790-2 as illustrated in Figure 4.6.

Specimens with 12.7 mm width and 200 mm length were cut using waterjet cutting machine. For laminated composites, the span length should be chosen such that failure occurs in the outer fibers of the specimen and is due only to bending moment. Hence, a span-to-depth ratio of 60:1 was chosen to eliminate shear effects; i.e. the support span was  $L=156$  mm. To avoid excessive indentation, or failure due to stress concentration directly under the loading nose, the radii of the loading nose and supports were chosen as 5 mm. It should be noted that the specimens were placed on the supports with the drill exit side uppermost, i.e. the compression side. This was done to expose the generally more serious delamination to compressive load, which typically causes the failure. The specimens were loaded at a constant crosshead speed of 1 mm/min until failure.

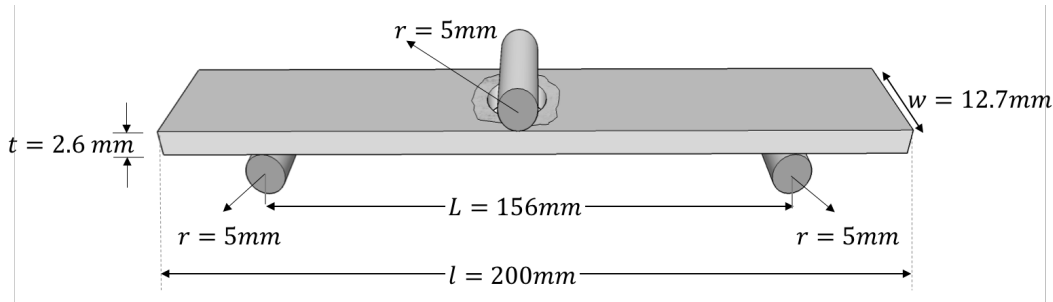


Figure 4.6. Schematic of experimental setup for three-point bending test on dilled specimens.

#### 4.2.6 Microstructure observation

A Carl Zeiss AG-EVO 50 scanning electron microscope was employed to observe the microstructure of the hole surface drilled on the specimens. The specimens were cut along the axis of the drilling hole and SEM images of drilled hole cylindrical wall were obtained. The images were taken at magnifications of 78, 200, 500, and 1000 X.

#### 4.2.7 Acoustic emission measurement

A two-channel data acquisition from Physical Acoustics Corporation (PAC) with a sampling rate of 1 MHz and pre-amplification of 40 dB was used to record AE data. AE measurements were obtained by using a broadband, resonant type, single-crystal piezoelectric transducer, called Pico, as an acoustic emission sensor, with an optimum frequency range of 100 kHz to 1 MHz. The piezoelectric transducer was placed on the specimen with a fixed distance of 40 mm from the center of the hole. Silicon grease was used as an acoustic couplant to improve the signal transmission between specimen and sensor. An amplitude threshold of 30 dB was used to avoid background noise during sampling. The amplitude distribution ranges from 0 to 100 dB in which 0 dB corresponds to 1mV. In order to calibrate AE sensor, the pencil lead break method was implemented according to ASTM E976-10 standard prior to each test. After the calibration step, the AE signals were recorded during the drilling tests. Figure 4.7 shows measurement of acoustic emission events during the drilling process.

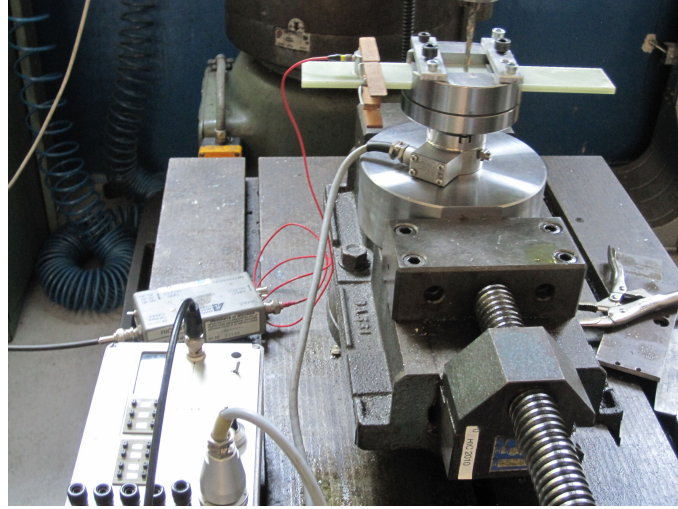


*Figure 4.7. Acoustic emission monitoring during the drilling process.*

### 4.3 Plan of experiments

Two methodologies were used in the present study to perform drilling tests; full factorial design and Taguchi orthogonal array design.

#### 4.3.1 Full factorial design

For compression specimens, the drilling experiments were conducted on the basis of general full factorial design. Full factorial design means that in each complete trial or replication of the experiment, all possible combinations of the levels of the factors are investigated. In some experiments, the difference in response between the levels of one factor is not the same at all levels of the other factors. When this occurs, there is an interaction between the factors. A factorial design is necessary when interactions may be present to avoid misleading conclusions. Furthermore, factorial designs allow the effects of a factor to be estimated at several levels of other factors, yielding conclusions that are valid over a range of experimental conditions. Minitab was used to create the design matrix and analyze the results as statistical analysis software. Two factors, i.e. feed rate and spindle speed, at three levels were used as input factors, and the delamination factor and residual compressive strength were considered as the main response factors. Table 4.4 indicates the drilling test parameters.

*Table 4.4. Factors and levels selected for drilling of compression specimens.*

Symbol	Control factor	Unit	Level 1	Level 2	Level 3
$f$	Feed rate	mm/min	31.5	63	125
$S$	Spindle speed	rpm	315	630	1000

#### 4.3.2 Taguchi method

For bending specimens, the drilling experimental procedure was performed based on the Taguchi method. The Taguchi method is a very robust and powerful method to deal with response (responses) influenced by a large number of variables. Instead of having to test all possible

combinations (like the factorial design), the Taguchi method tests pairs of combinations. This allows for the collection of the necessary data to determine which factors most affect the process with a minimum amount of experimentation, thus saving time and resources.

In this study, four factors, namely feed rate, spindle speed, drill diameter, and nano content, were selected as input factors based on preliminary researches and the thrust force, delamination factor and residual bending strength were considered as the main response factors. Once the factors affecting the process have been determined, the levels at which these factors should be varied must be determined. Determining which levels of a factor to test requires an in-depth understanding of the process. Table 4.5 shows the factors to be studied and the assignment of the corresponding levels. The orthogonal array chosen was  $L_{16}$  ( $2^2 \times 4^2$ ) shown in Table 4.6

*Table 4.5. Factors and levels selected for drilling of bending specimens.*

Symbol	Parameters	Units	Level 1	Level 2	Level 3	Level 4
$N$	Nano content	%	0	0.1	0.5	1
$f$	Feed rate	mm/rev	0.04	0.06	0.08	0.1
$S$	Spindle speed	rpm	315	630	-	-
$D$	Drill diameter	mm	4	5	-	-

*Table 4.6. The  $L_{16}$  orthogonal array layout.*

Test No.	Input factors				$S/N$
	$N$ (%)	$F$ (mm/rev)	$S$ (rpm)	$D$ (mm)	
1	0	0.04	315	4	$S/N_1$
2	0	0.06	315	4	$S/N_2$
3	0	0.08	630	5	$S/N_3$
4	0	0.1	630	5	$S/N_4$
5	0.1	0.04	315	5	$S/N_5$
6	0.1	0.06	315	5	$S/N_6$
7	0.1	0.08	630	4	$S/N_7$
8	0.1	0.1	630	4	$S/N_8$
9	0.5	0.4	630	4	$S/N_9$
10	0.5	0.06	630	4	$S/N_{10}$
11	0.5	0.08	315	5	$S/N_{11}$
12	0.5	0.1	315	5	$S/N_{12}$
13	1	0.04	630	5	$S/N_{13}$
14	1	0.06	630	5	$S/N_{14}$
15	1	0.08	315	4	$S/N_{15}$
16	1	0.1	315	4	$S/N_{16}$

## 4.4 Statistical analysis methods

### 4.4.1 Analysis of variance

Analysis of variance (ANOVA) is a statistical technique for determining the degree of difference or similarity between two or more groups of data. In this study, ANOVA was used with the purpose of investigating which process factors significantly affect the responses. This is accomplished by separating the total variability of the response, which is measured by the sum of the squared deviations from the total mean, into contributions by each of the design parameters and the error. The total sum of the squared deviations from the total mean can be calculated as [110]:

$$SS_T = \sum_{j=1}^p (y_j - y_m)^2 \quad (4.1)$$

where  $y_j$  represents the  $j$ -th observation,  $y_m$  is the total mean, and  $p$  is the total number of observations.

The total sum of squares is split into two sources: the sum of squares due to each input factor  $SS_d$  and that of error  $SS_e$ . The percentage contribution, obtained by calculating the ratio of the individual sum of squares of each factor and the total sum of squares, can be used to evaluate the importance of input factors on the responses. In addition,  $F$  test, named after Fisher, can be used to determine which parameters have a significant effect on the response. Usually, the change of the input parameter has a significant effect on the response when the  $F$  value is large.

### 4.4.2 Taguchi $S/N$ ratio analysis

After conducting the experiments as per orthogonal array, to determine the effect each factor has on the response, the signal-to-noise ratio ( $S/N$ ) is calculated for each experiment conducted. According to the Taguchi method, objective functions are classified into three categories, namely (1) smaller is better, (2) nominal is better, and (3) larger is better. For all categories, the optimum level is the one which gives the highest value of signal-to-noise ratio.

The  $SN$  ratio of the “smaller is better” can be expressed mathematically as follows:

$$S/N_i = -10 \log \left( \sum_{j=1}^{N_i} \frac{y_j^2}{N_i} \right) \quad (4.2)$$

For the case of “larger is better” quality characteristic, the following definition of  $SN$  ration should be used:

$$S/N_i = -10 \log \left( \frac{1}{N_i} \sum_{j=1}^{N_i} \frac{i}{y_j^2} \right) \quad (4.3)$$

Where  $i$  is the experiment number, and  $N_i$  is the number of trials for experiment  $i$ .

#### 4.4.3 Multi-objective optimization: Grey relational analysis

When there are multiple quality characteristics, Taguchi's  $S/N$  analysis provides a different set of optimum operating conditions for each characteristic. For example, in the composite drilling process, the optimum condition for minimizing cutting forces may not be the same as minimizing the delamination factor. When the characteristics are not independent, considering each characteristic separately can give a misleading estimate of overall performance. Proper analysis of data from such processes requires the use of multivariate statistical techniques. In this study, grey relational analysis (GRA) was used to investigate the multiple performance characteristics in the optimization of the composite drilling process. To perform the optimization, data processing was performed as follows [111]:

##### ***Normalization of the experimental results***

In grey relational analysis, data preprocessing is first performed to normalize the raw data. This data preprocessing is usually required since the range and the unit in one data sequence may differ from others. Depending on the characteristics of a data sequence, there are various methodologies of data preprocessing available in grey relational analysis.

When “lower is better” is a characteristic of the original sequence, the original sequence should be normalized as:

$$x_i^*(k) = \frac{\max_{\forall i} x_i^o(k) - x_i^o(k)}{\max_{\forall i} x_i^o(k) - \min_{\forall i} x_i^o(k)} \quad (4.4)$$

and if “larger is better” is a characteristic, the following definition should be adopted:

$$x_i^*(k) = \frac{x_i^o(k) - \min_{\forall i} x_i^o(k)}{\max_{\forall i} x_i^o(k) - \min_{\forall i} x_i^o(k)} \quad (4.5)$$

However, if here is a definite target value (desired value) to be achieved, the original sequence will be normalized as:

$$x_i^*(k) = 1 - \frac{|x_i^o(k) - x^o|}{\max_{\forall i} x_i^o(k) - x^o} \quad (4.6)$$

or the original sequence can be simply normalized by the most basic methodology, i.e. the values of original sequence is divided by the first value of the sequence:

$$x_i^*(k) = \frac{x_i^o(k)}{x_i^o(1)} \quad (4.7)$$

Where  $x_i^o(k)$  denotes the original sequence,  $x^o$  denotes the desired value and  $x_i^*(k)$  is the normalized sequence for the  $i$ -th experimental result of the  $k$ -th response factor.

##### ***Computing the grey relational coefficient***

The grey relational coefficient (GRC) expresses the relationship between the ideal and actual normalized experimental results. The GRC for the  $k$ -th performance characteristics in the  $i$ -th experiment is given by:

$$\xi_i(k) = \frac{\Delta_{\min} + \zeta \Delta_{\max}}{\Delta_{0i}(k) + \zeta \Delta_{\max}} \quad (4.8)$$

Where  $\Delta_{0i}$  is the absolute value of the difference between the reference  $x_0^*(k)$  and the comparability sequence  $x_i^*(k)$  which is known as the deviation sequence.  $\zeta$  is the distinguishing coefficient and can be any value in the range between 0 and 1. If the value of the  $\zeta$  is smaller, the distinguished ability is larger. Generally,  $\zeta=0.5$  is used.

$$\Delta_{0i}(k) = \|x_0^*(k) - x_i^*(k)\| \quad (4.9)$$

$$\Delta_{\min} = \min_{\forall j \in i} \min_{\forall k} \|x_0^*(k) - x_j^*(k)\| \quad (4.10)$$

$$\Delta_{\max} = \max_{\forall j \in i} \max_{\forall k} \|x_0^*(k) - x_j^*(k)\| \quad (4.11)$$

### **Computing the grey relational grade**

The overall evaluation of multiple quality characteristics is based on the grey relational grade, GRG. The GRG is an average sum of the grey relational coefficients which is defined as below:

$$X_i = \frac{1}{n} \sum_{k=1}^n \xi_i(k) \quad (4.12)$$

The grey relational grade indicates the degree of influence by the comparability sequence over the reference sequence. Hence, if a particular comparability sequence is more important than the other comparability sequences to the reference sequence, then it has a higher grade.

# CHAPTER 5

## 5 Analysis, Results and Discussion

This chapter reports on experiments conducted on drilling of composite laminates. A thorough experimental investigation on the drilling thrust force, delamination and residual properties of the drilled specimens are carried out. The material response and cutting conditions are documented and empirical conclusions are made based on the analysis of experimental data.

### 5.1 Thrust force

The main cutting force generated during drilling process is referred to as thrust force, or axial force along the direction of the feed. The two cutting lips and complex point geometries of the drill make the analysis of thrust force during drilling process somewhat difficult. For a better understanding of drilling as a dynamic process, some researchers compare drilling process with quasi-static penetration of composite laminates by an indenter. The typical force generated during the static penetration process in carbon-epoxy laminates subjected to blunt-ended punch is shown in Figure 5.1(a). The force applied by the indenter increases until matrix crack induced by delamination happens (point A), then a sudden drop occurs (point B). The stiffness of the plate is reduced, and as the load reaches its peak value (point C), a plug is formed. The force then drops rapidly (point D). After that, friction between the indenter and the hole provides the only resistance to the motion. Delamination is initiated by matrix cracks, located in the double-ply layers, and extends through the entire plate.

For studying drilling process, it is more realistic to consider the rounded cone indenter rather than blunt-ended punch. The typical force generated during quasi-static impact perforation of Kevlar/polyester laminates by a conical indenter is shown in Figure 5.1(b). From the figure, in the beginning of the process, the force increases due to both indentation and global deflection of the plate and reaches its maximum value (point A), then a plateau is reached related to fiber failure (point B). On complete penetration, the load rapidly drops to a much lower level as friction against the side of the hole provides the only resistance to the motion (point C). Goldsmith *et al.* [112] showed similar results for quasi-static penetration of woven graphite-epoxy laminates by conical indenters. Local deformation (bulging) and fiber failure constituted the major energy absorption mechanism.

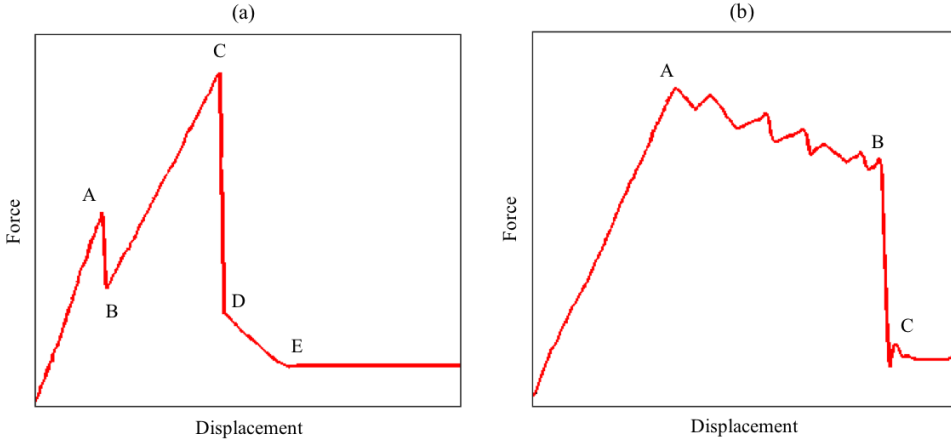


Figure 5.1. Load versus displacement in static test (a) flat cylindrical indenter [113] (b) conical indenter [114, 115].

The thrust force is a critical issue on controlling delamination and the residual mechanical properties of drilled laminates. It is believed that there is a limit value for the thrust force below which no damage occurs. During typical drilling experiments, the thrust force is measured on the time scale from drill entry into the workpiece to full engagement and drill exit from the material. The changes in thrust force during drilling at a feed rate of  $f = 63$  mm/min and spindle speed of  $S = 630$  rpm is illustrated in Figure 5.2. In this figure, the different stages of drilling have been outlined by several checkpoints.

The thrust force increases dramatically as the chisel edge of the twist drill bit approaches the composite surface (point A). The cutting speed ( $V_c$ ) is maximum at the extreme end of the drill radius and is reduced along the drill radius to zero at the center of the chisel edge. Therefore, the material in front of the chisel edge is subjected to an extrusion effect instead of a cutting action, which results in a drastic increase in the force. During drilling, the cutting edges gradually engage and the cutting force increases until the maximum force is obtained (point C). Before reaching the peak value, a sudden drop in force is observed (point B) which could be attributed to the peel-up delamination. The scanning electron microscopy (SEM) images presented in Figure 5.3(a) validate that delamination existed in the specimen at this stage. Further microscopic inspection performed on sections of the specimen suggests that in addition to delamination, there are a number of matrix cracks spreading in the laminate. It can be inferred that peel-up delamination is in fact induced by matrix cracking.

On complete engagement (point C), greater removal of material is performed at a more steadily state, resulting in a plateau in the cutting force plot with small oscillations associated with fiber failure (C-D). From the SEM images, Figure 5.3(b), fiber failure is observed at this stage. As the penetration continues, the thrust force plot shows a slight decrease due to the reduction in material resistance resulted by the successive fiber failure.

As the drill bit approaches the backside of the laminate, the number of uncut plies reduces and the resistance to bending decreases. At a critical thickness, the bending stress exceeds the interlaminar

strength, and the interlaminar crack initiates around the hole. Further penetration by the drilling tool makes the crack propagate until push-out delamination occurs. At this phase, the thrust force decreases stepwise, each step corresponding to the opening or widening of a crack (points E and F).

The exit of the twist drill bit from the backside of the laminate is followed from the G-E section. At this stage, the thrust force decreases catastrophically in a few seconds to a non-zero level because of the friction between the surfaces of the secondary cutting edges of the drill tool and the wall of the hole.

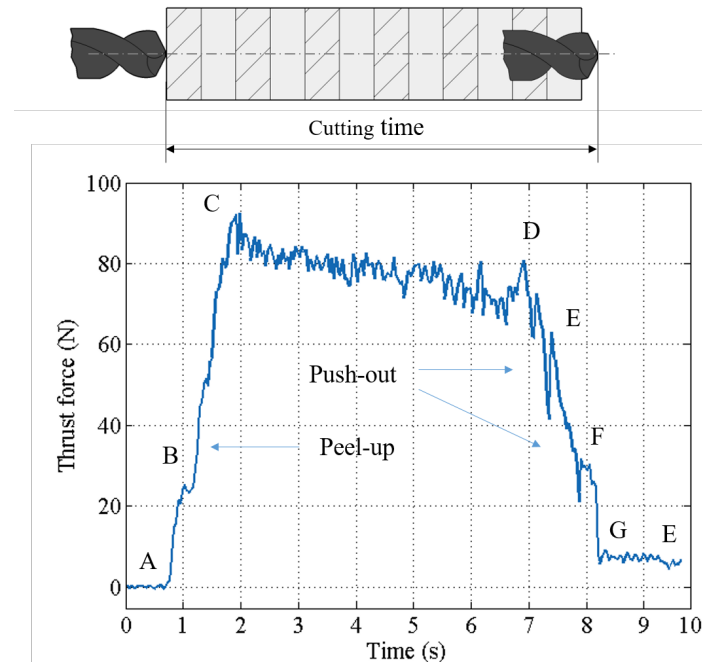


Figure 5.2. The thrust force plot during drilling at feed rate of  $f = 63$  mm/min and spindle speed of  $S = 630$  rpm.

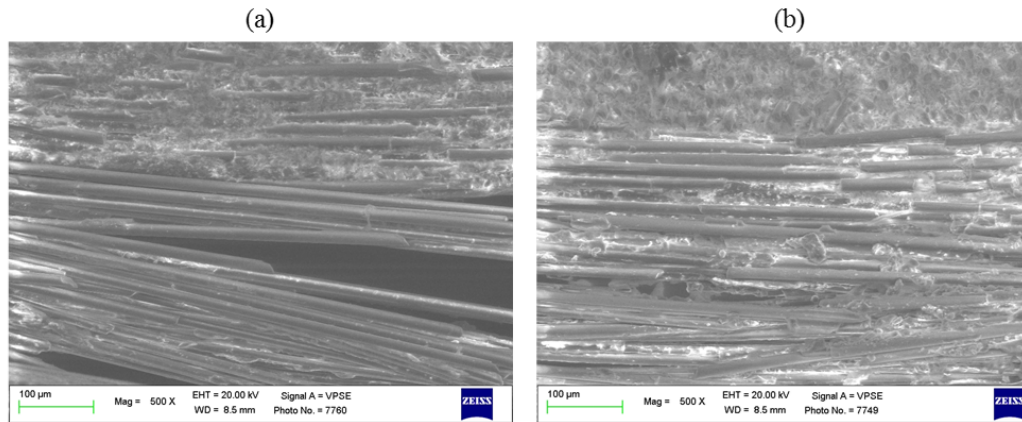


Figure 5.3. SEM images showing (a) matrix cracking and delamination during entry stage and (b) fiber failure during cutting stage.

The thrust force during drilling of composite laminates depend on input variables such as feed rate, cutting speed or spindle speed, drill bit geometry, and the nature of material being drilled. In order to investigate the effect of process parameters on the drilling thrust force, E-glass-epoxy/MWCNT composite laminates were drilled under various drilling conditions as described in chapter four. The measured experimental results of thrust force and the corresponding S/N ratios for experimental trials are summarized in Table 5.1. The results presented for thrust force are the maximum value observed during drilling.

*Table 5.1. Measured experimental results for thrust force*

Trial No.	Parameters				$F_{th}$ (N)		
	Nano content (%)	Feed rate (mm/rev)	Spindle speed (rpm)	Drill diameter (mm)	R <sub>1</sub>	R <sub>2</sub>	S/N
1	0	0.04	315	4	94.1	94.2	-39.48
2	0	0.06	315	4	129.4	128.3	-42.20
3	0	0.08	630	5	129.4	117.7	-41.85
4	0	0.1	630	5	159.4	200	-45.15
5	0.1	0.04	315	5	58.5	58.2	-35.32
6	0.1	0.06	315	5	105.9	82.4	-39.54
7	0.1	0.08	630	4	90.9	94.1	-39.32
8	0.1	0.1	630	4	153	164.8	-44.03
9	0.5	0.04	630	4	45.9	34.1	-32.13
10	0.5	0.06	630	4	60.3	55.2	-35.24
11	0.5	0.08	315	5	141.2	117.8	-42.28
12	0.5	0.1	315	5	200.1	211.8	-46.28
13	1	0.04	630	5	82.6	83.4	-38.38
14	1	0.06	630	5	82.4	85.3	-38.47
15	1	0.08	315	4	206	200.1	-46.15
16	1	0.1	315	4	231.8	234.8	-47.36

After completing the experiments, the next step in data analysis is to estimate the optimum level of each control factor and to perform analysis of variance (ANOVA). The ANOVA predicts the relative significance of the process parameters along with estimating the experimental errors. It gives the percentage contribution of each factor and provides a better feel for the relative effect of the different factors on experimental response. The complete analysis of variance is shown in Table 5.2. The ANOVA of raw data indicates that nano content, feed rate and spindle speed significantly affect the drilling thrust force at the 95% confidence level. The values of percentage contribution of each factor are obtained and plotted in Figure 5.4. From the figure, the drilling thrust force is primarily affected by feed rate (71.2%), followed by spindle speed (13%) and nano content (11.9%), while the effect of drill diameter is negligible (0.3%).

*Table 5.2. Analysis of variance table for thrust force.*

Source	Sum Sq.	DF	Mean Sq.	F	Prob>F
Nano-content	12378.5	3	4126.2	25.54	0
Feed rate	74008.1	3	24669.4	152.67	0
Cutting speed	13452.1	1	13452.1	83.25	0
Drill size	318.2	1	318.2	1.97	0.1739
Error	3716.4	23	161.6		
Total	103873.3	31			

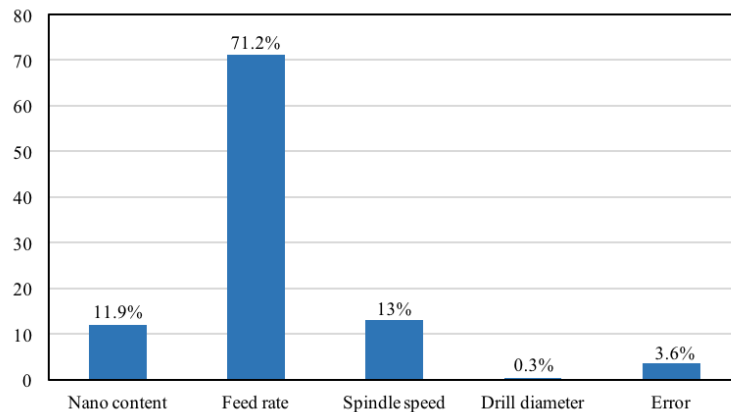


*Figure 5.4. Contribution percent of input variables on thrust force.*

In order to determine the effect of each variable on thrust force, the S/N values are obtained. The concept of Taguchi method and equations for calculating S/N are discussed in previous chapter. Once S/N ratio values are calculated for each factor and level, the delta (delta=high SN/low SN) of the S/N for each factor is calculated. The larger the delta value for a factor, the larger the effect the variable has on the process. This is because the same change in signal causes a larger effect on the output variable being measured.

The values of S/N ratios for thrust force are given in Table 5.3 and plotted in Figure 5.5. It was shown that the size of the delaminated area is related to the thrust force, and there is a critical thrust force below which no delamination initiates. The applied thrust force should not exceed this value to prevent delamination onset; hence, the “smaller is better” quality characteristic was used for thrust force. Table 5.3 and Figure 5.5 show that the feed rate and then the nano content and spindle speed have a great influence on thrust force; drilling thrust force, however, is negligibly influenced by the drill diameter. The size of delamination enlarges with increasing feed rate and decreasing spindle speed. This is mainly attributed to the higher impact of the cutting edges which leads to the increase in the drilling thrust force. In addition, it can be observed that the nano content has a positive effect on thrust force at the beginning and then its effect becomes negative. The optimum process parameters were obtained as nano content at level 3 (0.5 wt. %), feed rate at level 1 (0.04 mm/rev), spindle speed at level 2 (630 rpm) and drill diameter at level 1 (4 mm) for minimizing drilling thrust force.

Table 5.3. Response table for signal to noise ratios for thrust force.

	Nano content	Feed rate	Spindle speed	Drill diameter
Level 1	-42.17	-36.33	-42.33	-40.74
Level 2	-39.55	-38.86	-39.32	-40.91
Level 3	-38.98	-42.40		
Level 4	-42.59	-45.70		
Delta	3.61	9.37	3.01	0.17
Rank	2	1	3	4

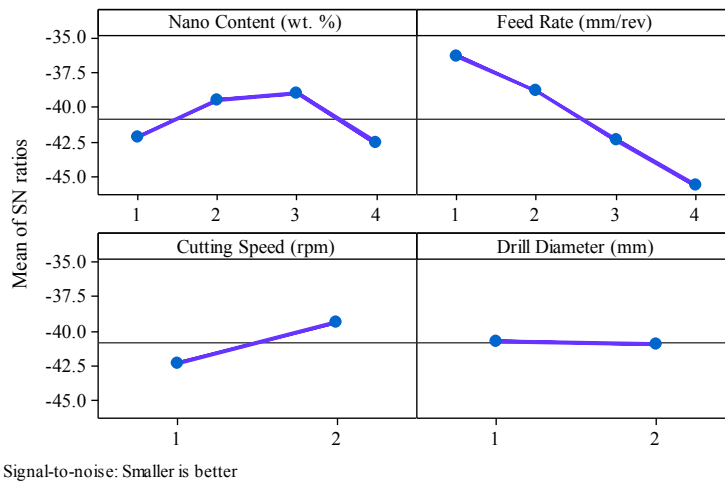


Figure 5.5. Main effects plot for S/N ratios of thrust force.

Achieved results can be compared with previous investigations [11, 39, 53, 58, 116, 117]. In these studies, different optimum conditions for minimizing thrust force were published. This is due to the fact that material characteristics of composite laminates such as fiber fraction, fiber orientation, type of resin, different fiber/matrix bond properties and also manufacturing methods greatly affect the thrust force generated during drilling. Despite this, most of the studies reported that the feed rate is one of the most effective parameters.

## 5.2 Delamination

Composite materials usually present more severe delamination at the drill exit side. After conducting drilling experiments, the images of the holes at the exit side were obtained using a digital scanner. The maximum diameter and the area of the damage were determined using an image processing software. The results obtained from image processing for a typical specimen drilled at 63 mm/min feed rate and 630 rpm spindle speed are presented in Figure 5.6. The values of adjusted delamination factor ( $F_{da}$ ) are calculated from Eq. (2.7) and are shown in Table 5.4.

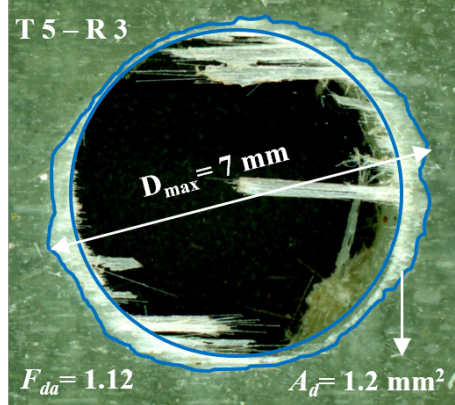


Figure 5.6. Measurement of the delaminated area ( $A_d$ ) of specimens at the exit side.

Table 5.4. Measured experimental results for delamination factor.

Trial No.	Parameters				$F_{da}$		
	Nano content (%)	Feed rate (mm/rev)	Spindle speed (rpm)	Drill diameter (mm)	R <sub>1</sub>	R <sub>2</sub>	S/N
1	0	0.04	315	4	1.17	1.17	-1.364
2	0	0.06	315	4	1.6	1.59	-4.055
3	0	0.08	630	5	1.61	1.55	-3.975
4	0	0.1	630	5	1.81	2.32	-6.364
5	0.1	0.04	315	5	1.09	1.08	-0.709
6	0.1	0.06	315	5	1.37	1.35	-2.671
7	0.1	0.08	630	4	1.15	1.15	-1.214
8	0.1	0.1	630	4	1.62	1.65	-4.271
9	0.5	0.04	630	4	1.08	1.08	-0.668
10	0.5	0.06	630	4	1.09	1.1	-0.788
11	0.5	0.08	315	5	1.71	1.69	-4.609
12	0.5	0.1	315	5	2.21	2.25	-6.966
13	1	0.04	630	5	1.11	1.12	-0.946
14	1	0.06	630	5	1.13	1.15	-1.138
15	1	0.08	315	4	2.33	2.4	-7.478
16	1	0.1	315	4	2.52	2.55	-8.08

The complete analysis of variance for adjusted delamination factor is shown in Table 5.5. In addition, in order to find the contribution of each parameter to the response, a Pareto chart is used. Pareto chart is a type of bar chart in which the horizontal axis shows categories of interest, rather than a continuous scale. By ordering the bars from largest to smallest, a Pareto chart helps to find which of the parameters significantly affect the response. A cumulative percentage line can help to assess the added contribution of each category. Pareto charts are helpful to focus improvement efforts on areas where the largest gains can be made. Pareto chart for process factors is shown in Figure 5.7. According to the results of Table 5.5 and Figure 5.7, adjusted delamination factor is significantly affected by feed rate (62,8%) followed by cutting speed (16.6%) and nano content (12.6 %); while the effect of drill diameter is negligible (0.2%). The error term in the table and

figure shows the influence of all factors not included in the experiments, their interactions, and effects of experimental error.

*Table 5.5. Analysis of variance table for delamination factor.*

Source	Sum Sq.	DF	Mean Sq.	F	Prob>F
Nano-content	0.95178	3	0.31726	12.25	0.0001
Feed rate	4.78217	3	0.59406	61.55	0
Cutting speed	1.26405	1	0.26405	48.81	0
Drill size	0.01531	1	0.01531	0.59	0.4497
Error	0.59564	23	0.0259		
Total	7.60895	31			

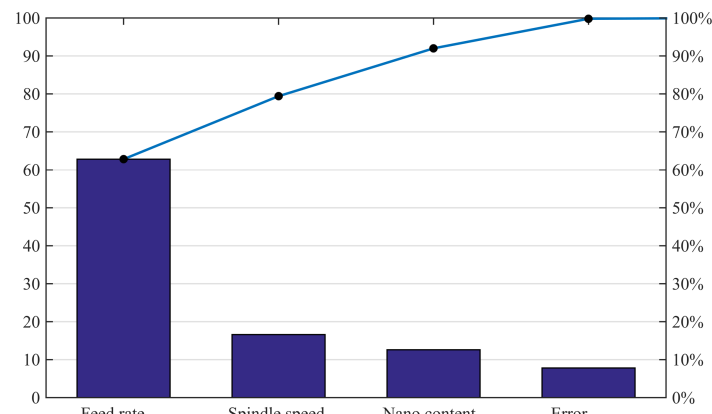


*Figure 5.7. Pareto chart of process parameters for delamination factor.*

The use of both analysis of variance technique and Taguchi's S/N ratio analysis makes it less cumbersome to analyze the results. The obtained values of S/N ratios for delamination factor are shown in Table 5.6 and plotted in Figure 5.8. The "smaller is better" quality characteristic was used since the objective is to minimize delamination size. The slope of the curves in Figure 5.8 is found to be steeper for feed rate, indicating this as the most influential parameter. It is clear that the feed rate has a negative effect; that is, increasing the feed rate moves the average delamination factor downwards. This can be attributed to the penetration action of the chisel edge of the drill bit. When the feed rate increases, the materials under the chisel edge are more likely to be extruded rather than cut. The force for pushing the drill through the workpiece is therefore higher and this produces greater bending responsible for interlaminar crack growth. Unlike feed rate, the spindle speed affects the delamination factor positively. As previously discussed, several conflicting observations regarding the effect of cutting speed on delamination have been reported. Until now, no explanation has been given about the cause of delamination variation due to cutting speed. However, the authors believe that it might be attributed to matrix softening. Higher cutting speed increases tool temperature and softens the workpiece material, which in turn makes the cutting force drops. Therefore, delamination decreases. According to the figure, adding nano content to E-glass-epoxy composites up to 0.1 wt. % reduces delamination size, but additional amounts can diversely affect delamination size. The optimum parameter setting was found to be nano content

at level 2 (0.1 wt. %), feed rate at level 1 (0.04 mm/rev), spindle speed at level 2 (630 rpm) and drill diameter at level 2 (5 mm) for minimizing the delamination size.

*Table 5.6. Response table for signal to noise ratios for delamination factor.*

	Nano content	Feed rate	Spindle speed	Drill diameter
Level 1	-3.9395	-0.9216	-4.4914	-3.4897
Level 2	-2.2161	-2.1633	-2.4205	-3.4223
Level 3	-3.2581	-4.3188		
Level 4	-4.4103	-6.4203		
Delta	2.1942	5.4987	2.0709	0.0675
Rank	2	1	3	4

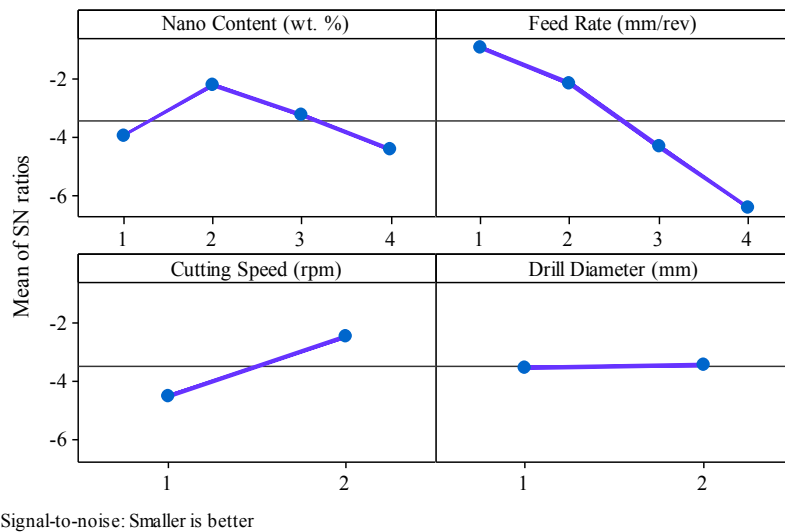


*Figure 5.8. Main effects plot for S/N ratios of delamination factor.*

Interaction effects are important in reaching a more general conclusion in parametric studies. To understand the interaction between factors, the graph of the average responses at each treatment combination is shown in Figure 5.9. The significant interaction is indicated by the lack of parallelism of the lines. From Figure 5.9, the drill diameter shows significant interactions with the cutting speed and nano content. Furthermore, a significant interaction between cutting speed and feed rate can be seen. There is also a fairly small interaction between feed rate and nano content, as shown by the quite similar shape of the curves.

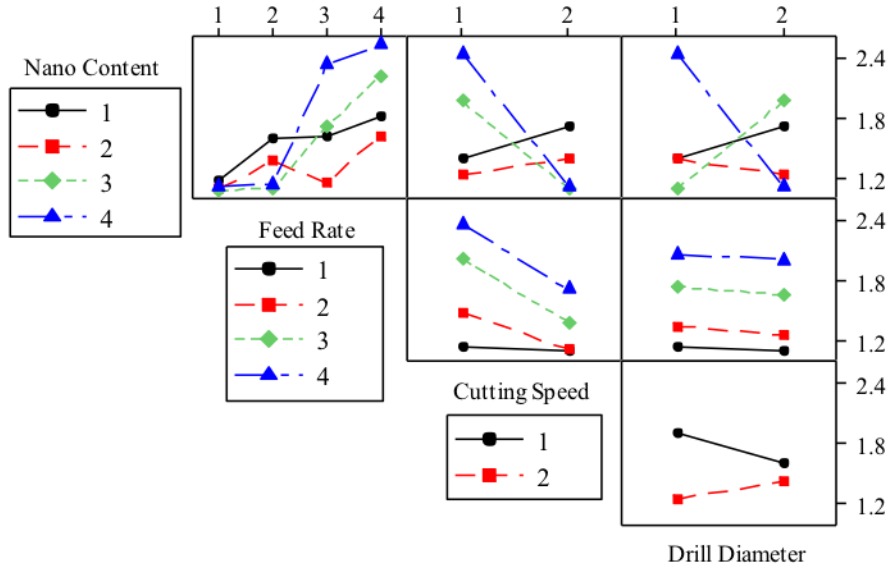


Figure 5.9. The interaction plots for mean values of measured delamination factors.

The variation of thrust force with the adjusted delamination factor is plotted in Figure 5.10. From figure, it appears to be a positive linear relationship between drilling thrust force and the adjusted delamination factor ( $F_{th} = 113.67 F_{da} - 53.983$ ). The thrust force generated during specimen drilling can be controlled by machining parameters, drill geometry and material properties. Selecting suitable parameters leads to the elimination of damage caused by drilling. To achieve the goal of elimination, the thrust force should be kept below the critical value. The critical thrust force can be identified as the intersection of the regression line and the vertical axis ( $F_{th}^c = 59.687$ ).

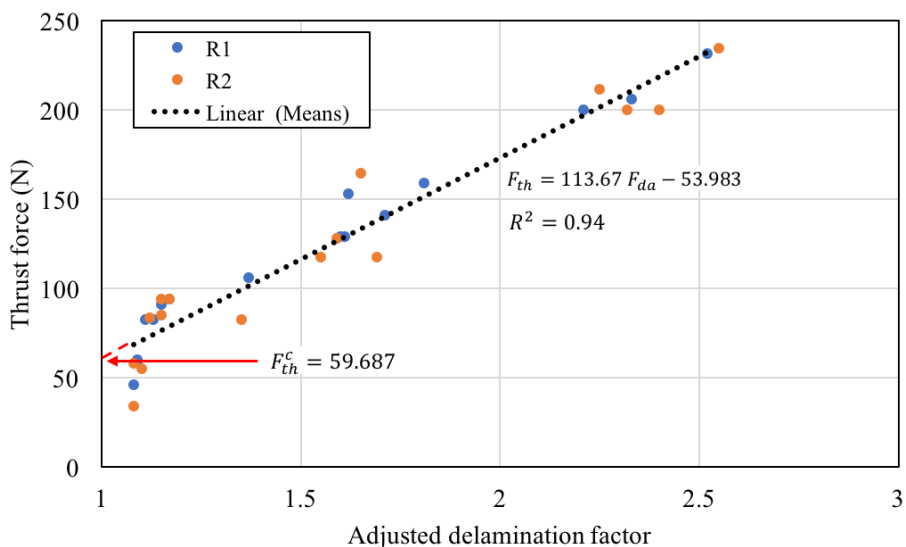


Figure 5.10. Positive linear relationship between thrust force and adjusted delamination factor.

### 5.3 Effects of drilling parameters on mechanical strength

The damage introduced during the drilling of composite laminates is detrimental to the mechanical behavior of the composite structure and significantly reduces the composite performance in use. Degree of damage depends on the composite material characteristics, tool geometry and material, and the process parameters. This section is focused on analyzing the influence of drilling parameters on the residual strength of the GFRP laminates after drilling. To this end, two sets of experiments were designed and carried out; E-glass/epoxy composites were drilled and then comparison tested to evaluate their residual compressive strength, E-glass fiber-epoxy composites reinforced with functionalized multi-walled carbon nanotubes were drilled and then bending tested to determine their residual bending strength. The experimental setup, material preparation, experimental procedure, inspect techniques, and other experimental related information are given in detail in chapter four.

#### 5.3.1 Residual compression strength

One of the most commonly used method for evaluation of the residual mechanical properties is the compression test. Compression is critical for delaminated specimens because under this type of loading, strength reductions are the largest. In order to evaluate the significance of drilling induced delamination on the mechanical behavior of GFRP laminates, drilled glass/epoxy composite specimens are compression tested. Figure 5.11 shows a typical drilled specimen during compression test. The measured experimental results of the delamination factor ( $F_{da}$ ) and residual compressive strength ( $\sigma_c$ ) are reported in Table 5.7. In the table,  $R_1$ ,  $R_2$ , and  $R_3$  represent the replicates for each test. The results presented for the delamination factor were obtained as explained in Section 5.2. The values of residual compressive strength were calculated as the ratio of ultimate force to the remained section area after drilling, which is expressed below as:

$$\sigma_c = \frac{F_U}{(w - d) t} \quad (5.1)$$

where  $F_U$ ,  $d$ ,  $w$ , and  $t$  are the ultimate compression force, the hole diameter, specimen width, and specimen thickness, respectively.

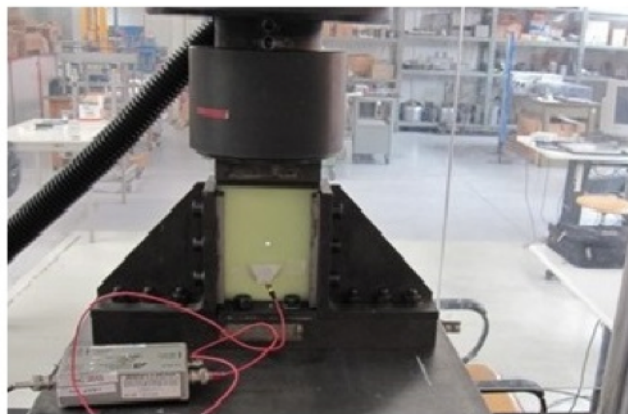


Figure 5.11. A typical specimen during compression test.

Table 5.7. The design matrix and measured experimental results.

Test No.	Parameters		$F_{da}$			$\sigma_c$ (MPa)		
	Feed rate (mm/min)	Spindle speed (rpm)	R <sub>1</sub>	R <sub>2</sub>	R <sub>3</sub>	R <sub>1</sub>	R <sub>2</sub>	R <sub>3</sub>
1	31.5	315	1.09	1.10	1.08	433.3	412.3	408.8
2	31.5	630	1.10	1.07	1.08	366.7	373.7	371.9
3	31.5	1000	1.07	1.04	1.05	450.9	426.3	417.5
4	63	315	1.12	1.13	1.11	359.6	363.2	352.6
5	63	630	1.15	1.15	1.12	338.6	331.6	329.8
6	63	1000	1.10	1.11	1.15	370.2	377.2	387.7
7	125	315	1.18	1.19	1.17	312.3	308.8	312.3
8	125	630	1.15	1.16	1.13	315.8	331.6	321.1
9	125	1000	1.13	1.08	1.11	305.3	298.2	305.3

Figure 5.12(a) shows the stress-apparent displacement plots of GFRP specimens drilled under different machining conditions. The figure shows an initial nonlinear behavior up to about 30 MPa (1 mm), followed by a linear behavior. The nonlinear behavior of the composite is a result of the problem of sample positioning at the test starting and it should not be considered for interpretation. As the load increases, the elastic behavior continues until it reaches its maximum value. At maximum load, fiber microbuckling and matrix cracking happen instantly, resulting in catastrophic fracture of the specimen. The values of residual compressive strength were calculated from the failure loads and were plotted versus the delamination factor in Figure 5.12(b). The figure shows that the residual compressive strength of the drilled GFRP specimens decreases with increasing delamination factor (as an index of damage) although this relation is not linear ( $R^2 = 0.62$ ).

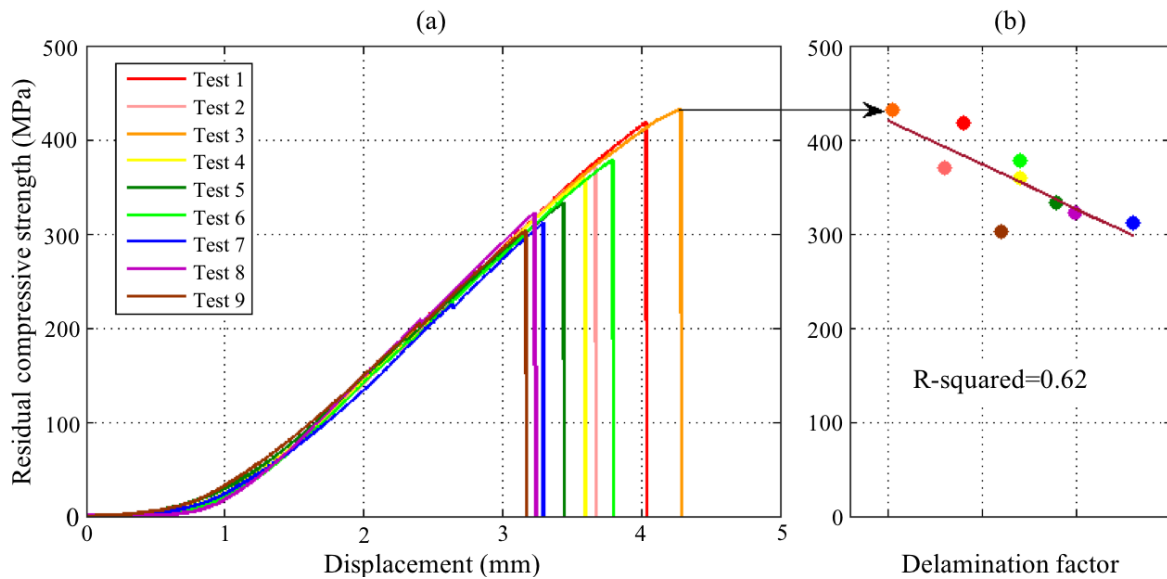
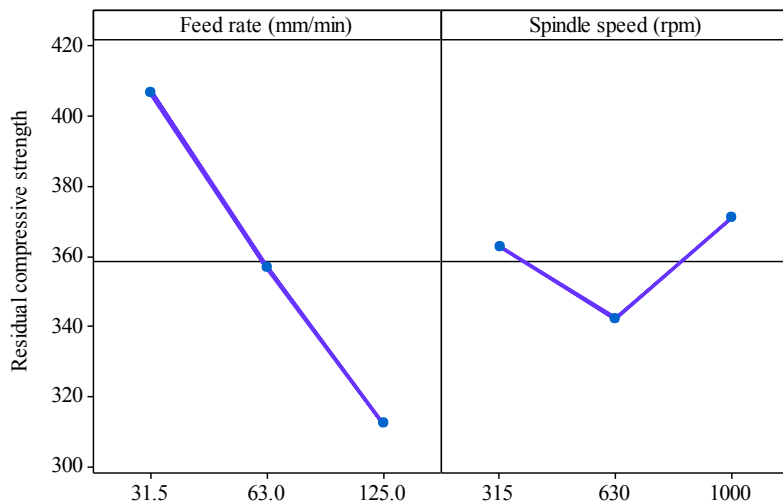


Figure 5.12. Residual compressive strength for different drilling conditions vs. (a) displacement, (b) delamination factor.

The analysis of variance for residual compressive strength is summarized in Table 5.8. According to the P-value column, the feed rate and spindle speed significantly affect the residual compressive strength. The feed rate–spindle speed interaction has a P-value of <0.0001, indicating a significant interaction between these factors. To help with the practical interpretation of the experiments, Figure 5.13 presents plots of the two main effects. It is noticed that the feed rate has a negative effect on residual compressive strength, i.e. increasing the feed rate moves the average response downwards. On the other hand, the spindle speed has a negative effect at the beginning and then its effect changes to positive. Table 5.8 also shows contribution percentage of the factors and their interaction. The feed rate has the highest contribution percentage, indicating it has the greatest effect on the residual compressive strength.

*Table 5.8. Analysis of variance for residual compressive strength.*

Source of Variation	Sum of Squares	Degrees of Freedom	Mean Square	$F_0$	P-Value	Contribution Percentage (%)
Feed rate	40253	2	20126.7	257.93	0.0001	77.9
Spindle Speed	3904	2	1952.1	25.02	0.0001	7.3
Interaction	5872	4	1468.1	18.81	0.0001	10.7
Error	1405	18	78.0			4.1
Total	51434	26				



*Figure 5.13. Main effects plot for residual compressive strength.*

One of the main features of analysis of variance is the adequacy of the underlying model. For this purpose, analysis of residuals is used as the primary diagnostic tool. Through a study of residuals, many types of model adequacies and violations of the underlying assumptions can be discovered. The residuals for the two-factor factorial model are as follows:

$$e_{ijk} = y_{ijk} - \hat{y}_{ijk} \quad (5.2)$$

where  $y_{ijk}$  is the observed response when feed rate is at the  $i$ -th level and spindle speed is at the  $j$ -th level for the  $k$ -th replicate.

The residuals from the compressive strength values are shown in Figure 5.14. A check of normality assumption could be made by plotting a histogram of the residuals, as shown in Figure 5.14(a). It is noticed that this plot looks like a normal distribution centered at zero, indicating that the normality assumption is satisfied. Moreover, the normal probability plot, Figure 5.14(b), shows nothing particularly troublesome. If the model is adequate, the residuals should be structureless, i.e. they should contain no obvious patterns. A simple check is to plot the residuals against the fitted values. From Figure 5.14(c) the usual structure is apparent. Plotting residuals in time order of data collection is helpful in detecting a correlation between the residuals. A plot of these residuals versus time is shown in Figure 5.14(d). There is no reason to suspect any violation of the independence or constant variance assumptions.

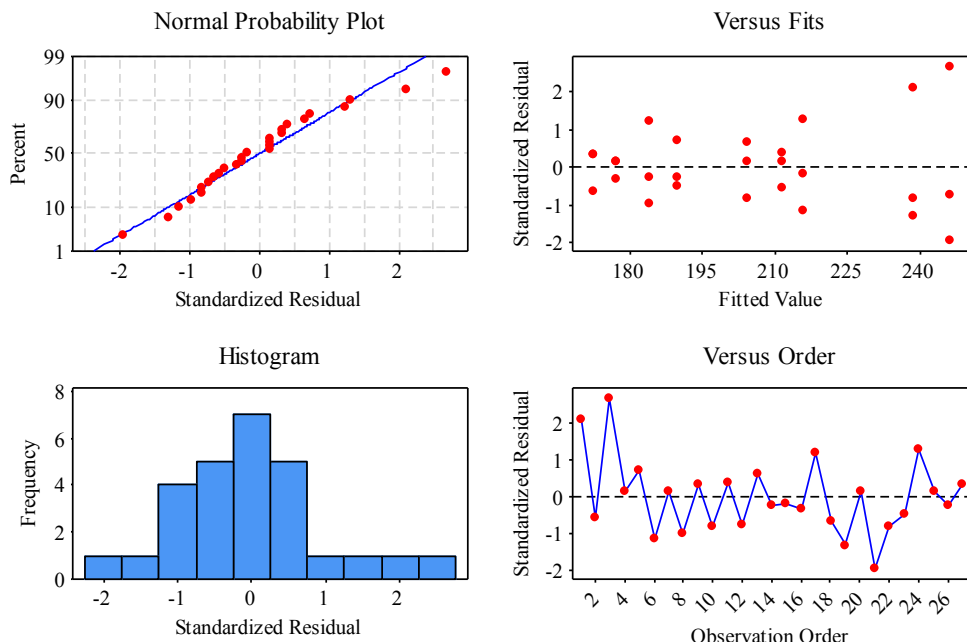


Figure 5.14. Residual plots for residual compressive strength.

Figure 5.15 (a) and (b) plot the residuals against the feed rate and spindle speed, respectively. Both plots indicate mild inequality of variance. Two treatments, i.e. (31.5 mm/min and 315 rpm) and (31.5 mm/min and 1000 rpm), have a larger variance than the others that are responsible for the inequality of the variance. These are the only two positive residuals whose absolute values are greater than 2. However, this problem is not severe enough to have a dramatic impact on the analysis and conclusions.

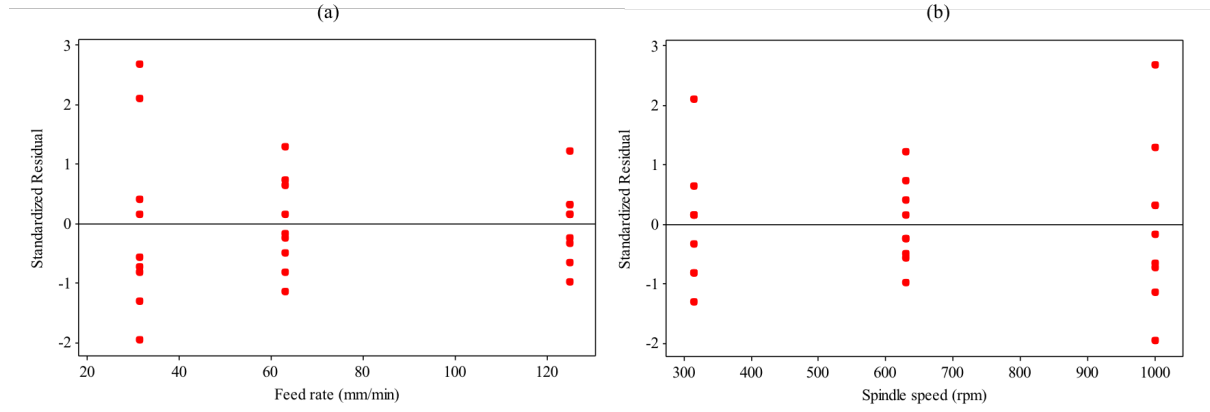


Figure 5.15. Plots of standardized residuals versus (a) feed rate, (b) spindle speed.

To understand the interaction between the factors, the graph of the average responses at each treatment combination is shown in Figure 5.16(a). The significant interaction is indicated by the lack of parallelism of the lines when feed rate is kept high. Notice that at low and medium levels of feed rate, the interaction is small, as shown by the similar shape of the two curves. Figure 5.16(b) presents a contour plot of the surface generated by the prediction model for residual compressive strength. The contour plot indicates that the feed rate of 31.5 mm/min and spindle speed of 1000 rpm are the best choices to achieve maximum residual compressive strength.

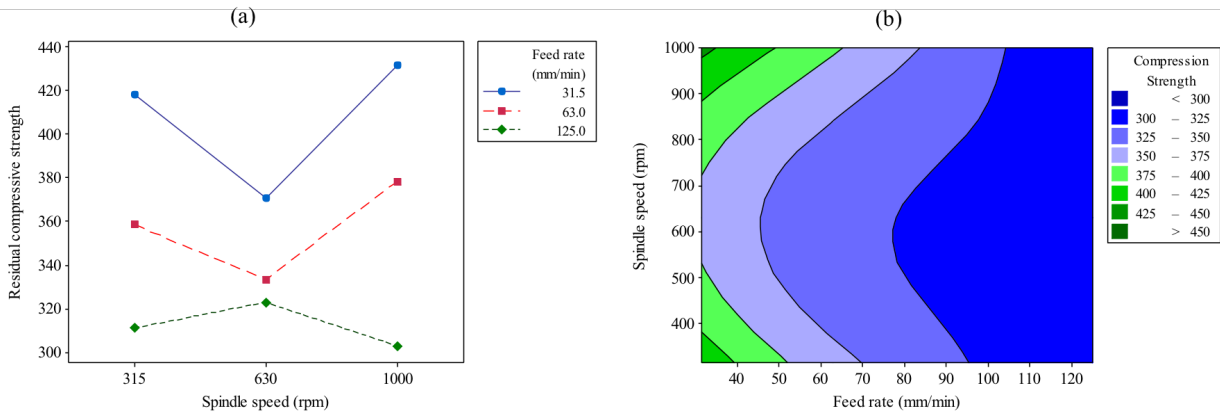


Figure 5.16. (a) The interaction plot and, (b) the contour plot of the residual compressive strength.

In order to make a mathematical model that shows the relationship between the feed rate and spindle speed as input factors and residual compressive strength as the response, a polynomial regression model was adopted. MATLAB software was used to generate the regression model; the result is shown in Eq. (5.7). This equation is useful for interpolation- that is, for predicting the residual compressive strength ( $\sigma_c$ ) at factor levels between those actually used in the experiment. Figure 5.17 shows response surface of the corresponding regression model.

$$\begin{aligned} \sigma_c &= 519.8 - 2.188f - 0.2276S + 0.009347f^2 - 0.0004411fS + 0.0002069S^2 \\ R^2 &= 0.8706 \quad R_{adj}^2 = 0.8398 \end{aligned} \quad (5.3)$$

where  $f$  is the feed rate in mm/min and  $S$  is the spindle speed in rpm.

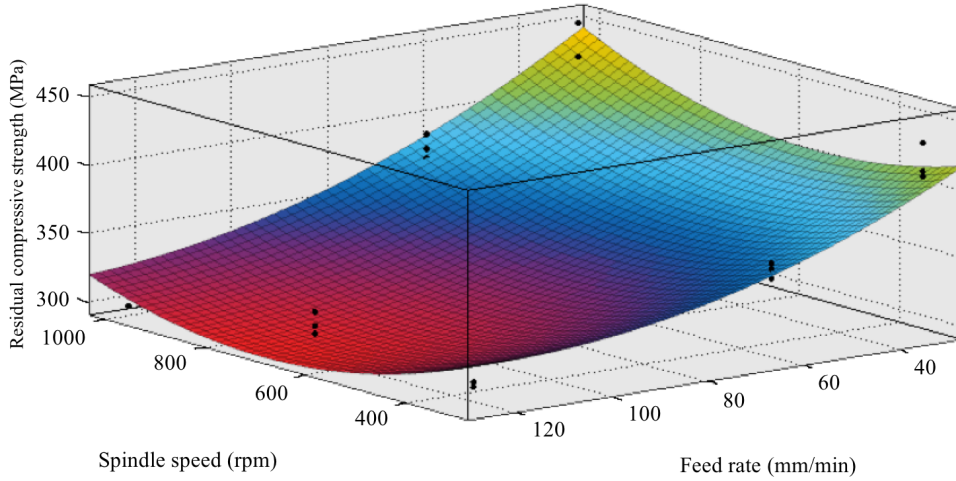


Figure 5.17. The response surface of the polynomial regression model for residual compressive strength.

### 5.3.2 Residual flexural strength

Even though composite materials are often used in applications where they are subjected to bending, the residual flexural strength has received relatively little attention. In this section, we aim to investigate the influence of drilling induced delamination on the residual flexural strength of E-glass-epoxy/MWCNT laminates. To this end, E-glass fiber-epoxy composites reinforced with functionalized multi-walled carbon nanotubes were cut into bending standard dimensions and drilled under various drilling conditions and then subject to quasi-static bending test, as described in chapter four. An approach based on the Taguchi method with grey relational analysis was adopted for optimizing the drilling process with multiple performance characteristics.

A typical specimen during the bending test is shown in Figure 5.18. The L<sub>16</sub> orthogonal array layout and the measured experimental results of the thrust force ( $F_{th}$ ), delamination factor ( $F_{da}$ ) and residual flexural strength ( $\sigma_b$ ) are given in Table 5.9. The results presented for thrust force are the maximum value observed during drilling and the values of delamination factor were obtained as explained in Section 5.2. The residual bending strength was calculated from failure load  $P$ , and the sample and bearing geometry by the following equation [109]:

$$\sigma_b = \frac{3PL}{2(w-d)t^2} \quad (5.4)$$

Where  $L$  is the support span,  $d$  is the hole diameter, and  $w$  and  $t$  are, respectively, the width and thickness of the test specimen as defined in Figure 4.6.



Figure 5.18. A typical drilled specimen during the bending test.

Table 5.9. The  $L_{16}$  orthogonal array layout and measured experimental results.

Trial No.	Parameters				$F_{th}$ (N)		$F_{da}$		$\sigma_b$ (MPa)	
	$N$ (%)	$F$ (mm/rev)	$S$ (rpm)	$D$ (mm)	R <sub>1</sub>	R <sub>2</sub>	R <sub>1</sub>	R <sub>2</sub>	R <sub>1</sub>	R <sub>2</sub>
1	0	0.04	315	4	94.1	94.2	1.17	1.17	261.2	254.3
2	0	0.06	315	4	129.4	128.3	1.6	1.59	238.9	246.2
3	0	0.08	630	5	129.4	117.7	1.61	1.55	218.8	221.1
4	0	0.1	630	5	159.4	200	1.81	2.32	211.2	223.1
5	0.1	0.04	315	5	58.5	58.2	1.09	1.08	285.6	279.6
6	0.1	0.06	315	5	105.9	82.4	1.37	1.35	267	274.4
7	0.1	0.08	630	4	90.9	94.1	1.15	1.15	252	248.4
8	0.1	0.1	630	4	153	164.8	1.62	1.65	241.2	240.9
9	0.5	0.04	630	4	45.9	34.1	1.08	1.08	346.8	343
10	0.5	0.06	630	4	60.3	55.2	1.09	1.1	338.1	343.9
11	0.5	0.08	315	5	141.2	117.8	1.71	1.69	318	324.5
12	0.5	0.1	315	5	200.1	211.8	2.21	2.25	305.7	296.4
13	1	0.04	630	5	82.6	83.4	1.11	1.12	317.3	334.2
14	1	0.06	630	5	82.4	85.3	1.13	1.15	305.9	312.9
15	1	0.08	315	4	206	200.1	2.33	2.4	271.8	258.6
16	1	0.1	315	4	231.8	234.8	2.52	2.55	266.7	261.4

### Analysis of results using statistical analysis of variance

The primary objective of analysis of variance is to investigate the significance of parameters affecting the residual flexural strength characteristics of the composite. The results of the ANOVA analysis are given in Table 5.10. Figure 5.19 shows the percentage contribution of each factor on the total variation indicating how influential the factors are to the results. Based on the results of Table 5.10 and Figure 5.19, Residual flexural strength is mostly affected by nano content (74.2%), followed by feed rate (22.8%), and the effects of spindle speed (0.5%) and drill diameter (0.4%) are insignificant. A remarkable change in the significance of nano content is observed for residual flexural strength compared to what was observed for thrust force, see Section 5.1, and delamination

factor, see Section 5.2. This indicates that the residual properties of composite materials depend on the properties of the constituent materials rather than machining conditions. The error term in the table shows the influence of all factors not included in the experiments, their interactions, and effects of the experimental error.

*Table 5.10. Analysis of variance table for residual flexural strength.*

Source	Sum Sq.	DF	Mean Sq.	F	Prob>F
Nano-content	38132.1	3	12710.7	268.93	0
Feed rate	11697.4	3	3899.1	82.5	0
Cutting speed	244.8	1	244.8	5.18	0.0325
Drill size	211.7	1	211.7	4.48	0.0454
Error	1087.1	23	47.3		
Total	51373	31			

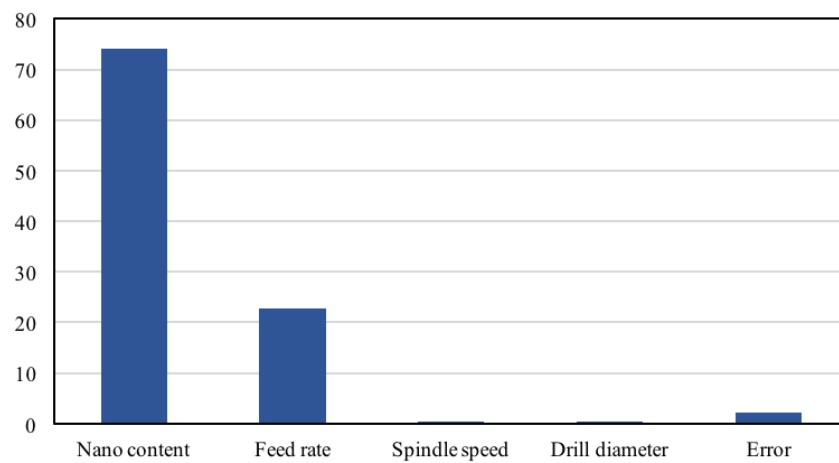


*Figure 5.19. Contribution percent of input variables on residual flexural strength.*

### ***Analysis of results using Taguchi's S/N ratio***

The key feature of the orthogonal design is that it allows the researcher to separate out the effect of each parameter at different levels. To determine the relative effect of each level, the average of S/N ratios within that level needs to be calculated. For example, the mean S/N ratios for nano content at levels 1 and 2 can be obtained by averaging the S/N ratios for the experiments 1-4 and 5-8, respectively. The mean S/N ratio for each level of process parameters is summarized in Table 5.11. Furthermore, the main effects plot for S/N ratios is presented in Figure 5.20. to make the results easier to interpret. This plot shows the variation in the response when the factor goes from one level to another level.

After delamination inspection, three-point bending tests were carried out on the specimens to evaluate their residual flexural strength. The values of S/N ratios for residual flexural strength are shown in Table 5.11 and in Figure 5.20. The objective is to maximize the residual flexural strength to enhance the bending resistance of composite structures. Therefore, the “larger is better” quality characteristic was selected. According to the rank values in the table and slope of the curves in the figure, nano content is found to be the most influential factor followed by feed rate. The effect of

cutting speed and drill diameter is, however, unimportant which is in good agreement with the results obtained using analysis of variance. As expected, residual flexural strength increases with decreasing feed rate. When feed rate is kept at a low level, thrust force becomes smaller; that is, less damage introduces around the hole. Some of the external energy is consumed for crack nucleation and growth; hence, final failure takes place at the higher level of energy. The figure shows that an increase in the nano content from 0 to 0.5 wt. % causes a considerable increase in residual flexural strength. Further increase in nano content, however, shows a relatively high decrease in flexural strength. This demonstrates that incorporation of MWCNTs is an efficient way to reduce delamination size and to enhance the flexural strength of E-glass-epoxy/MWCNT composites, but caution needs to be taken into consideration. The optimum parameter setting was found to be nano content at level 3 (0.5 wt. %), feed rate at level 1 (0.04 mm/rev), spindle speed at level 2 (630 rpm) and drill diameter at level 2 (5 mm) when considering residual flexural strength as a response individually.

*Table 5.11. Response table for signal to noise ratios for residual flexural strength.*

	Nano content	Feed rate	Spindle speed	Drill diameter
Level 1	47.37	49.56	48.77	48.73
Level 2	48.32	49.20	48.83	48.88
Level 3	50.28	48.35		
Level 4	49.24	48.09		
Delta	2.91	1.47	0.06	0.15
Rank	1	2	4	3

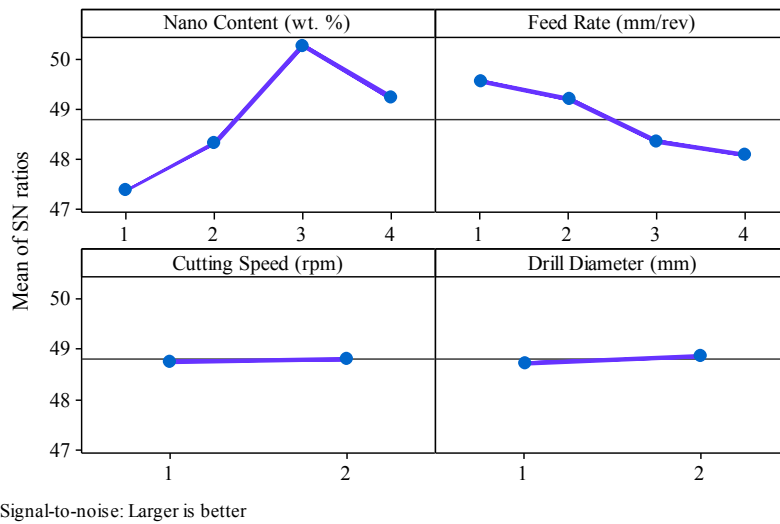


*Figure 5.20. Main effects plot for S/N ratios of residual flexural strength.*

### ***Analysis of results using grey relational analysis***

Analysis of results using Taguchi's S/N ratios revealed that the lower thrust force, as well as the lower delamination size, provides the highest residual strength of the laminate when subjected to bending loads. To achieve low thrust force, low delamination factor and high residual flexural strength at the time, grey relation analysis was used in this work. The experimental data described

in Table 5.9 were used to obtain the grey relational grades as described in Section 4.4.3. In the grey relational data preprocessing, the thrust force and the delamination factor were normalized using the “lower the better” methodology as expressed in Eq. (4.4); and, the residual bending strength was normalized using the “larger is better” quality characteristic, Eq. (4.5). Table 5.12 shows the normalized results for all three performance characteristics.

*Table 5.12. Data preprocessing of the experimental results, the reference sequence is 1.*

Trial No.	Thrust force		Delamination factor		Residual flexural strength	
	R <sub>1</sub>	R <sub>2</sub>	R <sub>1</sub>	R <sub>2</sub>	R <sub>1</sub>	R <sub>2</sub>
1	0.7407	0.7005	0.9375	0.9388	0.3687	0.2704
2	0.5508	0.5306	0.6389	0.6531	0.2043	0.2044
3	0.5508	0.5835	0.6319	0.6803	0.0560	0.0000
4	0.3895	0.1734	0.4931	0.1565	0.0000	0.0163
5	0.9322	0.8799	0.9931	1.0000	0.5487	0.4764
6	0.6772	0.7593	0.7986	0.8163	0.4115	0.4340
7	0.7579	0.7010	0.9514	0.9524	0.3009	0.2223
8	0.4239	0.3488	0.6250	0.6122	0.2212	0.1612
9	1.0000	1.0000	1.000	1.0000	1.0000	0.9927
10	0.9225	0.8949	0.9931	0.9864	0.9358	1.0000
11	0.4874	0.5830	0.5625	0.5850	0.7876	0.8420
12	0.1705	0.1146	0.2153	0.2041	0.6969	0.6132
13	0.8026	0.7544	0.9792	0.9728	0.7824	0.9210
14	0.8037	0.7449	0.9653	0.9524	0.6984	0.7476
15	0.1388	0.1729	0.1319	0.1020	0.4469	0.3054
16	0.0000	0.0000	0.0000	0.0000	0.4093	0.3282

After the data preprocessing, the deviation sequences were determined using Eq. (4.9). The value of the reference sequence,  $x_0^*(k)$ , used for computing deviation sequences was chosen as one. In this study, the distinguishing coefficient  $\zeta = 1$  was substituted in Eq. (4.8) to compute the grey relational coefficients. Table 5.13 gives the grey relational coefficients for all three performance characteristics, the grey relational grade, and its order. The highest value of grey relational grade was found to be 0.9976, indicating that the corresponding experiment, experiment number 9, has the optimum combination of parameters in order to attain multiple performances.

Table 5.13. The calculated grey relational coefficient, grey relational grade, and the corresponding order.

Trial No.	Grey relation coefficient				GRG		Order	
	Thrust force		Delamination factor		Residual flexural strength			
	R <sub>1</sub>	R <sub>2</sub>	R <sub>1</sub>	R <sub>2</sub>	R <sub>1</sub>	R <sub>2</sub>		
1	0.6585	0.6254	0.8889	0.8909	0.4420	0.4066	0.6521	
2	0.5268	0.5158	0.5806	0.5904	0.3859	0.3859	0.4976	
3	0.5268	0.5455	0.5760	0.6100	0.3463	0.3333	0.4896	
4	0.4502	0.3769	0.4966	0.3722	0.3333	0.3370	0.3944	
5	0.8806	0.8063	0.9863	1.0000	0.5256	0.4885	0.7812	
6	0.6077	0.6751	0.7129	0.7313	0.4593	0.4691	0.6092	
7	0.6738	0.6258	0.9114	0.9130	0.4170	0.3913	0.6554	
8	0.4646	0.4343	0.5714	0.5632	0.3910	0.3735	0.4663	
9	1.0000	1.0000	1.0000	1.0000	1.0000	0.9856	0.9976	
10	0.8659	0.8263	0.9863	0.9735	0.8863	1.000	0.9230	
11	0.4938	0.5452	0.5333	0.5465	0.7019	0.7599	0.5968	
12	0.3761	0.3609	0.3892	0.3858	0.6226	0.5638	0.4497	
13	0.7169	0.6706	0.9600	0.9484	0.6968	0.8636	0.8094	
14	0.7180	0.6622	0.9351	0.9130	0.6237	0.6645	0.7528	
15	0.3673	0.3768	0.3655	0.3577	0.4748	0.4185	0.3934	
16	0.3333	0.3333	0.3333	0.3333	0.4584	0.4267	0.3697	

It is also helpful to separate out the effect of each parameter on the grey relational grade at different levels through average analysis. This is obtained by computing the average value of each process parameter, preprocessed data, at its corresponding level. For example, the average grey relational grade for the parameter “feed rate” at level 1 can be calculated as  $\bar{f}_1 = \frac{1}{4}(0.6521+0.7812+0.9976+0.8094)$ . The mean of the grey relational grade for each level of input variables was calculated and the values are given in Table 5.14 and shown graphically in Figure 5.21. The dashed line in the figure is the value of the total mean of the grey relational grade.

In Figure 5.21, the steep slope of the curves indicates the greater influence of the input parameter in the performance characteristics. It is clear that the feed rate is the most influential factor among the four input parameters, followed by nano content and spindle speed. The figure shows that the highest value of grey relational grade is obtained for the lowest level of feed rate, i.e. 0.04 mm/rev. Both thrust force and delamination size increase significantly with increasing feed rate due to the punch effect. In fact, at high feed rates, the drill point acts like a punch on the laminate, instead of cutting through it. As more damage is made around the hole, the residual flexural strength decreases. Unlike feed rate, the spindle speed has a positive effect on the multiple performance characteristics, i.e. the grey relational grade representing the multiple performance characteristics increases with the increase in spindle speed. From the figure (nano content), it can be noted that the presence of MWCNTs significantly improves the multiple performance characteristics. The highest value of grey relational grade is obtained for the third level of nano content, i.e. 0.5 wt. %. As the nano content changes from 0 to 0.5 wt. %, the grey relational grade increases by a large magnitude. With a further increase in the nano content, particle aggregation occurs, thus leading to degradation in multiple performance characteristics. In composite drilling process, drill diameter

has very little influence on the multiple performance characteristics as can be seen from its mild slope. Based on the response graph and response table, the optimum parameter setting to achieve the minimum value of thrust force, the minimum value of delamination factor and the maximum value of residual flexural strength is:

- Nano content at level 3, 0.05 wt. %
- Feed rate at level 1, 0.04 mm/rev
- Spindle speed at level 2, 630 rpm
- Drill diameter at level 1, 4 mm

The accuracy of the results can be further improved by including more number of parameters and levels.

*Table 5.14. Response table for grey relational grade.*

	Nano content	Feed rate	Spindle speed	Drill diameter
Level 1	0.5084	<b>0.8101</b>	0.5437	<b>0.6194</b>
Level 2	0.6280	0.6957	<b>0.6861</b>	0.6104
Level 3	<b>0.7418</b>	0.5338		
Level 4	0.5813	0.4200		
Delta	0.2334	0.3900	0.1423	0.0090
Rank	2	1	3	4
Total mean grey relational grade = 0.6149				

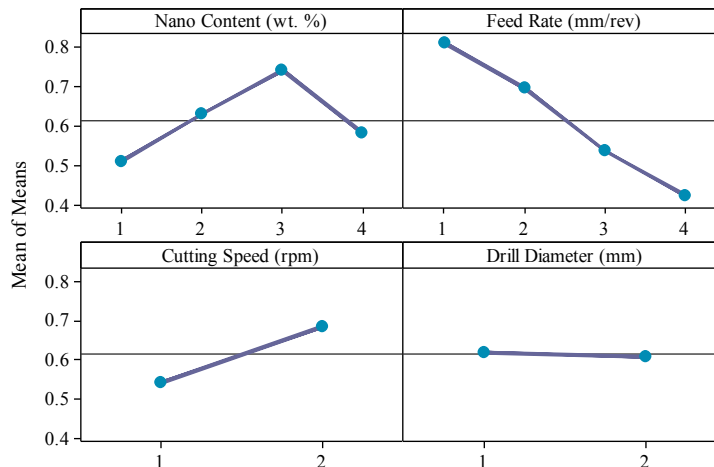


*Figure 5.21. Response graph for the grey relational grade.*

#### **Verification of the optimal parameters through the confirmation experiments**

Once the optimal parameter setting is obtained, the next step is to predict and verify the improvement of performance characteristics using the optimal level of the parameters. The estimated grey relational grade  $\hat{y}$  is defined as below:

$$\hat{\gamma} = \gamma_m + \sum_{i=1}^p (\bar{\gamma} - \gamma_m) \quad (5.5)$$

Where  $\gamma_m$  is the total mean of the grey relational grade,  $\bar{\gamma}$  is the mean of the grey relational grade at the optimal level, and  $p$  is the number of the parameters significantly affecting the multiple performance characteristics. Table 5.15 shows the comparison results of the initial process parameters and the optimal parameters. The experimental results at optimal level show that the thrust force is greatly reduced from 94.15 N to 40 N (-57.5%), delamination factor is decreased from 1.17 to 1.08 (-7.7%), and residual flexural strength is improved from 257.75 MPa to 344.9 MPa (33.8%). In addition, an improvement of 34.55% is observed in the grey relational grade. This clearly indicates that the multiple performance characteristics in the composite drilling process are greatly improved through this approach.

*Table 5.15. Results of drilling performances using the initial and optimal machining parameters.*

	Initial parameter setting	Optimal parameter setting	
		Prediction	Experimental
Setting level	N <sub>1</sub> F <sub>1</sub> S <sub>1</sub> D <sub>1</sub>	N <sub>3</sub> F <sub>1</sub> S <sub>2</sub> D <sub>1</sub>	N <sub>3</sub> F <sub>1</sub> S <sub>2</sub> D <sub>1</sub>
Thrust force (N)	94.15		40
Delamination factor	1.17		1.08
Residual flexural strength (MPa)	257.75		344.9
Grey relational grade	0.6521	1.0000	0.9976
Improvement of the grey relational grade	= 0.3455		

# CHAPTER 6

## 6 ACOUSTIC EMISSION MONITORING

Acoustic emission (AE) refers to the sounds, generated when a material undergoes permanent changes, such as cracking and delamination. Acoustic emissions from composites have been studied over the past forty years, and can provide remarkable information about the state of the material health. It is observed that the failure of a composite component under load is accompanied by a considerable amount of audible and sub-audible noise. In certain circumstances, some audible noise is generated even before ultimate failure. Using very simple equipment including a microphone, an amplifier, and an oscillograph, sub-audible sounds can be detected at stress levels of 50% of the ultimate strength. Sophisticated equipment can be used to detect sound at much lower loads, in some cases below 10% of the ultimate strength. These sounds, both audible and sub-audible, are referred to as acoustic emissions [118].

Acoustic emissions are the transient elastic waves that are generated by the rapid release of energy from localized sources within a material [120]. These waves travel through the material, and their arrival at the surfaces can be detected by AE sensors. In composite materials, acoustic emissions are caused by irreversible changes like crack initiation, delamination propagation, fiber breakage, debonding between continuous and dispersed phases.

In this chapter, a feasibility study of acoustic emission as a tool for monitoring and nondestructive evaluation of drilling of composites is conducted. A procedure for discrimination and identification of different damage mechanisms occurring during drilling based on the analysis of acoustical signals is presented.

### 6.1 Historical background

The first published studies of acoustic emission, in the early 1940s, dealt with the problem of predicting rock bursts in mines. The first significant investigation of acoustic emission from metals was carried out by Kaiser [121]. He observed that AE events occur only if the previous applied stress level is exceeded.

The early studies of acoustic emission in composite materials under stress was conducted by Rüsch [122], who noted that during cycles of loading and unloading below about 70 to 85% of the ultimate failure load, acoustic emissions were generated only when the previous maximum load was reached, the Kaiser effect. In 1965, Robinson [123] employed sensitive equipment to show that AE events occurred at much lower load levels than had been reported earlier, and subsequently, could be used to monitor microcracking. In 1970, Wells [124] used a more sensitive apparatus, with which he could monitor acoustic emissions in the frequency range of [2 -20] kHz. Later, in 1970, Green [125] conducted more extensive series of experiments and recorded acoustic emission frequencies up to 100 kHz. Green demonstrated clearly that AEs from composite

materials are related to failure processes within the material by using source location techniques, he also determines the locations of damages. It was this work that indicated that acoustic emissions could be employed as an early warning of failure. Green also noted that acoustic emission monitoring could be used to determine the previous maximum stress applied to the specimen.

## 6.2 Theoretical considerations

When an acoustic emission event occurs at a source within the material, because of inelastic deformation or cracking, the stress waves propagate through the material and are detected by an AE sensor (vibration to electrical signal conversion elements) placed on the surface. Surface waves then arise from mode conversion. As soon as the stress waves are received by the sensor, the transducer responds to the surface motions occurring. Note that the signal detected by the AE sensors are influenced by the nature of the stress pulse generated by the source, the geometry of the test specimen, and the characteristics of the sensor, which makes it difficult to interpret the recorded waveforms. Figure 6.1 shows two typical types of acoustic emission signals. Continuous emission is a qualitative description of the sustained signal level produced by rapidly occurring acoustic emission events. These are generated by events such as plastic deformations in metals, which occur in a reasonably continuous manner. Burst emission is a qualitative description of the discrete signal related to an individual emission event occurring within the material, such as that which may occur during crack growth or fracture in composite materials. These burst signals are characteristic of the acoustic emission events resulting from the loading of composite materials [119].

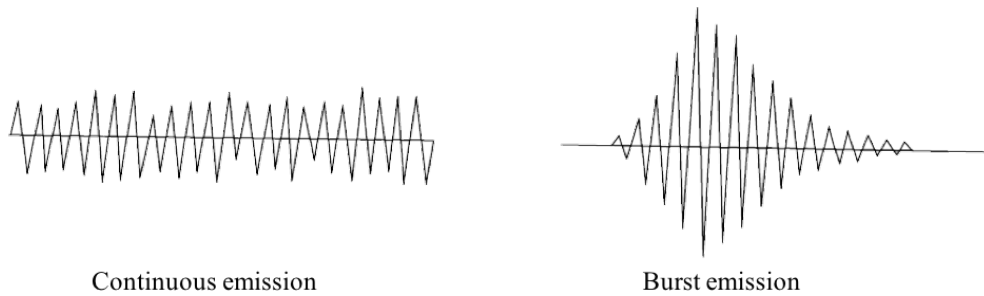
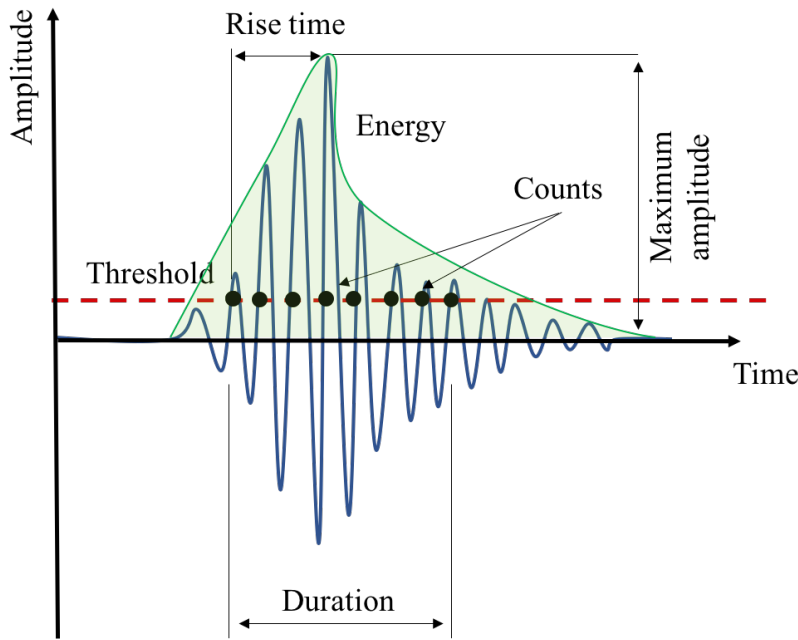


Figure 6.1. The two typical types of acoustic emission signals; Continuous emission and Burst emission.

## 6.3 Evaluation of acoustic emission signals

Figure 6.2 shows a typical acoustic emission signal generated during drilling of composites. As can be seen, the complexity of the signal becomes more apparent when acoustic events are studied in detail. In other words, the scatter in noise makes it difficult to determine exactly the time of arrival of the signal. This indicates that very sensitive and high-quality equipment are needed to get the information from the AE signals. Furthermore, the acoustic emission signals need to be amplified in order to obtain reasonable sensitivity. Some of the most important parameters which can be used to evaluate acoustic emission signals are:



*Figure 6.2. The definitions for a typical acoustic emission signal during drilling process.*

**Acoustic Emission Counting-** The number of times the acoustic emission signal exceeds a preset threshold during any selected portion of a test is called count. The AE count at a given time is divided by the time that has elapsed since the start of the AE signal, and the count result per unit time is called the AE count rate.

**Event counting-** Circuitry is available that counts each acoustic emission event only once, by recognizing the end of each burst emission in terms of a predetermined length of time since the last count (i.e. since the most recent crossing of the threshold).

**Rise time-** The time that elapses between the start of an AE signal and the time corresponding to the AE signal peak amplitude is called the AE signal rise time. Rise time can be used to determine the type of damage mechanism.

**Signal duration-** The time that elapses between the start and end of an AE signal is called the AE signal duration. The signal duration can also be related to the type of damage mechanism.

**Amplitude distribution-** This provides the distribution of peak amplitudes. Amplitude can be used to identify the sources of the emission events that are occurring.

**AE root mean square (RMS)-** This is obtained by calculating the root mean square of an AE signal. The effective value is also called the room mean square value which represents the energy level of the AE signal and also enables evaluation of the rate of occurrence of AE.

**Frequency-** This refers to the frequency spectrum of individual acoustic emission events. Frequency analysis, generally requiring a fast Fourier transformation (FFT) analysis of the acoustic emission waves, can help discriminate between different types of events. Note that, a frequency

analysis may sometimes simply be a function of the response of the transducer, and thus reveal little of the true nature of the pulse.

**Signal Energy-** The AE signal energy is determined as the square of the AE signal amplitude, the integral of the square of the instantaneous amplitude of the AE discriminated signal over a certain duration, or integral of the instantaneous AE signal amplitude determined by envelope detection over a certain duration.

**Event Energy-** This refers to the total energy, AE event energy, released due to an AE event.

#### 6.4 Application to monitor machining of composites

One of the main issues associated with the application of laminated composites in industrial structures is their tendency to delaminate under cutting forces which may cause unexpected failure mechanisms in these materials. Machining-associated damages severely affect the mechanical properties of the part. The problem is complicated by the fact that internal damages cannot be detected by visual inspection. With the purpose of evaluating the effect of damages on composite properties, determining the behavior of the damage during the loading of the component is recommended. Current non-destructive damage assessment techniques include offline and online methods; however, offline methods cannot be used to assess damage under loading. Hence, the damage caused by machining requires the use of online monitoring techniques. In the field of machining, acoustic emission is considered one of the most acceptable and accurate online methods.

As explained previously, when a material is loaded, the strain energy is released because of microstructural changes, resulting in propagation of elastic stress waves known as acoustic emissions. For composite materials, many mechanisms have been confirmed as AE sources including matrix cracking, fiber failure, delamination, and friction. AE deals with the detection of such waves at the materials surface. This technique potentially makes it possible to determine the location of AE source as well as to characterize its nature. The stress waves resulting from the microstructural changes are dependent on the propagation conditions including attenuation, damping and boundary surface interactions in a heterogeneous medium. Hence, the signal delivered by the sensor is a greatly modified representation of the original source. Even so, it is realistic to consider that this signal contains some features representation of the source in such a manner that direct correlation exists between the damage mechanisms and the magnitude of the various AE parameters. Therefore, each signal can be considered as the acoustic signature of particular damage mode.

#### 6.5 Literature review

Ravishankar *et al.* [126] used acoustic emission root mean square (AE-RMS) index to interpret drilling stages from entry to exit. They mentioned that total AE signals gathered from the drilling of composite materials are from four important sources, namely, fiber cutting, matrix cutting, friction, and delamination. They tried to identify signal sources by examining the signal characteristic of each source when drilled separately to quantify the energy level and then compare

them with the total signals, which contains energy due to all sources. In the next stage, they looked for the typical parameters that can characterize the individual sources. In a similar approach [127], they found frequency characteristics of emission from contact friction (rubbing action due to the rotating chisel edge touching the specimen), drilling (generation of microchips) and peripheral friction (rubbing action of the rotating drill body against the hole walls). Velayudham *et al.* [128] used acoustic emission for condition monitoring of composite drilling process. They applied wavelet packet transform (WPT) on AE data and extracted features to monitor tool wear condition with number of holes. The results show that the monitoring index increases with the number of holes due to rubbing of worn drill flank.

The major problem associated with AE signal processing is the discrimination between the different acoustic emission sources. Among numerous processing methods, cluster analysis is a robust tool for investigating and interpreting data. The main objective of cluster analysis is to separate a set of data into several classes reflecting the internal structure of the data. Godin *et al.* [129] classified recorded AE signals collected during tensile tests on cross-ply glass/epoxy composites in order to distinguish damage mechanisms. They used a combination of the self-organizing map (SOM) and the k-means methods to classify recorded AE in three clusters. They chose six time-domain AE parameters: amplitude, duration, rise time, counts, counts to peak, and energy as an input vector for clustering problem. According to their results, amplitude distributions of different damage mechanisms (matrix cracking, interfacial debonding, and delamination) were achieved. In a similar study, Godin *et al.* [130] used two different methods of classification; a supervised and unsupervised classification (Kohonen's map) for AE signals recorded during tensile tests on glass/polyester composites. They combined two techniques; the k-means algorithm, and the k-nearest neighbors. Three different specimens with different damage mechanisms were used, namely pure resin samples, 90 and 45 off-axis unidirectional composite samples. These different specimens were expected to produce different damage modes during tensile tests. Based on the results, the characteristics of signals for each damage mode were identified. These characteristics are duration, rise time, amplitude distribution, and number of hits. Huguet *et al.* [131] used acoustic emission data as input in a Kohonen self-organizing map which automatically clusters the acoustic emission signals, making a correlation with the failure modes possible. Marec *et al.* [132] used multivariable analysis and wavelet transform for clustering acoustic emission data. The clustering methods were fuzzy c-means clustering coupled with a principal component analysis. The continuous wavelet transform and discrete wavelet transform were used on typical matrix cracking and fiber-matrix debonding AE signals. Different frequency distributions of these two kinds of signals were noticeably recognized. Matrix cracking mainly has a frequency range of 50–150 kHz, while the frequency range for debonding is 170–350 kHz. Pappas *et al.* [133] applied a k-mean algorithm on AE recorded data during the quasi-static tensile loading of center-hole carbon/carbon composites. They clustered AE data into five classes related to five damage mechanisms, namely short fiber/matrix debonding, interlaminar matrix cracking, single fiber failure, fiber pullout, and multi fiber failure.

Philippidis *et al.* [134] used neural network techniques on AE signals to characterize damage of carbon/carbon laminates. They used the modified learning vector quantization (M-LVQ) technique which is suitable for types of AE data emitted by composites. Bar *et al.* [135] used PVDF sensors to identify failure modes in glass fiber reinforced plastic (GFRP) based on the artificial neural network (ANN) approach. Their results show that the characteristics of the AE signals are not affected by the stacking sequence of a laminate but are dependent on the failure mechanisms. ANN can also classify the AE signals which are highly overlapping in their parameters. Omkar *et al.* [136] used ant colony optimization to classify acoustic emission (AE) signals to their respective sources. Their experimental results show that this method is able to generate straightforward rules to classify the AE data set accurately. Moevus *et al.* [137] studied damage mechanisms and associated acoustic emission in two SiCf/Si–B–C composites exhibiting different tensile behaviors. They applied the k-mean classification method to find the AE characteristic of different damage mechanisms. They successfully distinguished different types of matrix cracking in the composite by the time domain AE analysis. Liu *et al.* [138] used fuzzy pattern recognition of AE signals for detecting grinding burn. They applied wavelet packet transform to extract features from AE signals and fuzzy pattern recognition for optimizing features and identifying the grinding status.

## 6.6 Clustering methodology

Each AE signal can be associated with a pattern which is composed of multiple relevant descriptors. The patterns can then be divided into clusters representative of damage mechanisms according to their similarity by the use of multivariable data analyses based on pattern recognition algorithms [129]. Since it is not possible to know the exact origin of an emitted event and then to provide a training set of patterns belonging to several composite damage mechanisms, unsupervised pattern recognition is sometimes employed with the problem of labeling the clusters [139-141].

The fuzzy c-means clustering method (FCM) is an effective unsupervised algorithm for the automatic clustering and separating of AE patterns composed of multiple features extracted from the random AE waveforms [142]. The principle component analysis (PCA) is used to give an idea of the relevance the descriptors. If the representation in the projection space shows several clusters with a minimum overlap between them, the features can lead to classification of the damage mechanisms [143].

In this section, unsupervised pattern recognition analysis (fuzzy c-means clustering) associated with a principal component analysis are described as the tools used for the classification of the monitored AE events.

### 6.6.1 Fuzzy c-means clustering

Clustering is a general methodology and a remarkably rich conceptual and algorithmic framework for data analysis and interpretation. Clustering refers to identifying the number of subclasses of  $c$  clusters in a data universe  $X$ , consisting of  $n$  samples, and partitioning  $X$  into  $c$  clusters ( $2 \leq c \leq$

$n$ ). Note that  $c = 1$  denotes rejection of hypothesis that there are clusters in data set and  $c = n$  constitutes the trivial case where each sample is in one cluster by itself. The members in the same group are more similar, in some sense or another, to each other than to those in other groups. There are two kinds of  $c$ -partitions of data, namely hard (or crisp), and soft (or fuzzy).

Hard clustering assigns each data point to one and only one of the clusters, with a degree of membership equal to one, assuming well-defined boundaries between the clusters. This model does not reflect the description of real data, where boundaries between the subgroups may be fuzzy. A family of clustering algorithms is developed based on fuzzy clustering using the least square error criterion. Bezdek [144] developed an extremely powerful classification method to accommodate fuzzy sets, which is an extension of hard  $c$ -means clustering algorithm.

Fuzzy  $c$ -means (FCM) is defined as a data clustering technique in which a data set is grouped into  $c$  clusters with every data point in the dataset belonging to every cluster to a certain degree. This technique was first introduced by Dunn [145] and generalized by Bezdek [142, 144]. To introduce this method, a sample set of  $n$  data samples is defined as:

$$X = \{x_1, x_2, x_3, \dots, x_n\} \quad (6.1)$$

Where each data sample,  $x_i$ , is defined by  $m$  features, that is,

$$x_i = \{x_i^1, x_i^2, x_i^3, \dots, x_i^m\} \quad (6.2)$$

This means that each  $x_i$  in the universe  $X$  is an  $m$ -dimensional vector of  $m$  elements or  $m$  features. Since the features all can have different units, normalization of the features to unified scale before classification is necessary.

Bezdek suggested using an objective function approach for clustering the data. In this approach, each cluster is considered as one hyper spherical shape with hypothetical geometric cluster center. The main aim of the objective function is to minimize the Euclidian distance between each data point in the cluster and its cluster center, and to maximize the Euclidian distance between other cluster centers.

A family of fuzzy sets,  $A_i, i = \{1, 2, \dots, c\}$ , is defined as a fuzzy  $c$ -partition on a universe of data points. As previously mentioned, a single point  $x_k$  can have partial membership value, that is  $k$ -th data point in  $i$ -th class has the membership value expresses as below:

$$\mu_{ik} = \mu_{Ai}(x_k) \in [0,1] \quad (6.3)$$

with the restriction that the sum of all membership values for a single point in all the classes has to be unity:

$$\sum_{i=1}^c \mu_{ik} = 1, \quad \forall k = 1, 2, 3, \dots, n \quad (6.4)$$

There can be no class that contains an empty set and there can be no class that contains all the data points. This is represented as below:

$$0 < \sum_{i=1}^c \mu_{ik} < 1 \quad (6.5)$$

In case of fuzzy classification, each data point can have partial membership in more than one class, that is:

$$\mu_{ik} \wedge \mu_{jk} \neq 0 \quad (6.6)$$

Now we can define a family of fuzzy partition matrices  $M_{fc}$ , for the classification involving  $c$  classes and  $n$  data points:

$$M_{fc} = \{U | \mu_{ik} \in [0,1]\}, \quad \forall i = 1, 2, 3, \dots, c \quad \text{and} \quad k = 1, 2, 3, \dots, n \quad (6.7)$$

Any  $\mu \in M_{fc}$  is a fuzzy  $c$ -partition, and it follows from the overlapping character of the classes and the infinite number of membership values possible for describing the class membership. The objective function used for  $c$ -clustering is:

$$J(u, v) = \sum_{k=1}^n \sum_{i=1}^c (\mu_{ik})^{m'} (d_{ik})^2 \quad (6.8)$$

Where  $d_{ik}$ , the distance between the point  $x_k$  and the center  $v_i$ , is obtained as follows:

$$d_{ik} = d(x_k - v_i) = \left[ \sum_{j=1}^m (x_{kj} - v_{ij}) \right]^{\frac{1}{2}} \quad (6.9)$$

A new parameter is introduced in Eq. (6.8) called a weighting parameter,  $m'$ . This parameter has a range  $m' = [1, \infty)$ , and controls the amount of fuzziness in the classification process.  $V_i$  is the cluster center of  $i$ -th class, obtained as below:

$$v_{ij} = \frac{\sum_{k=1}^n \mu_{ik}^{m'} \cdot x_{kj}}{\sum_{k=1}^n \mu_{ik}^{m'}} \quad j = 1, 2, 3, \dots, m \quad (6.10)$$

The objective of the clustering is to minimize the objective function with respect to the partition matrix and cluster center.

$$J_m^*(U, V) = \min_{M_{fc}} J(u, v) \quad (6.11)$$

As with many optimization processes, the solution to Eq. (6.11) cannot be guaranteed to be a global optimum. In order to achieve global optimum, an effective algorithm called iterative optimization was proposed by Bezdek. As shown in Figure 6.3, the following steps are used to perform the iterative FCM clustering:

1. Fix  $c$  ( $2 \leq c \leq n$ ) and select a value for  $m'$ ,
2. Initialize the partition matrix  $U^{(0)}$ , set  $r=0$ ,
3. Calculate the centers  $v_i^{(0)}$ ,

4. Update the partition matrix.

$$\mu_{ik}^{(r+1)} = \left[ \sum_{j=1}^c \left( \frac{d_{ik}^{(r)}}{d_{jk}^{(r)}} \right)^{\frac{2}{m'-1}} \right]^{-1} \quad (6.12)$$

Steps (2)-(4) are iterated until the improvement over the previous iteration is below a threshold  $\varepsilon$ , with  $r$  repenting the number of iteration steps:

$$\|J^{r+1} - J^r\| \leq \varepsilon \quad (6.13)$$

The main advantage of fuzzy clustering is partition matrix converges fast even with quite poor guess.

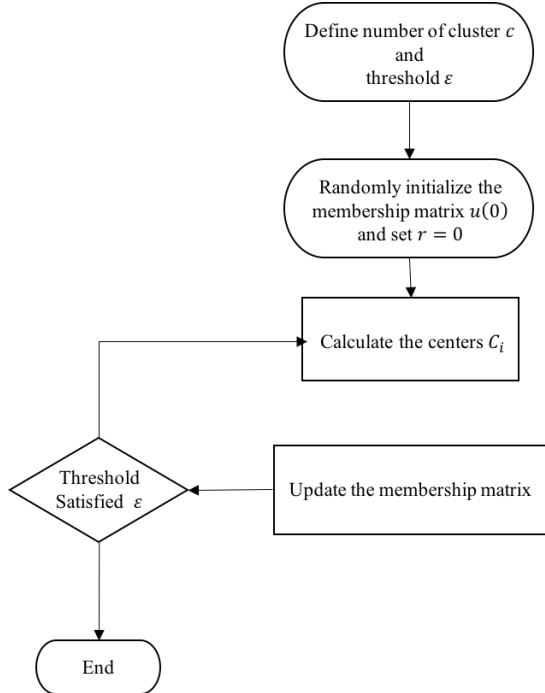


Figure 6.3. Fuzzy  $c$ -means clustering algorithm.

## 6.6.2 Principal component analysis

One of the difficulties inherent in multivariate statistics is the problem of visualizing data that have many variables. The problem can be simplified by replacing a group of variables with one or more new variables. The basic goal of principal component analysis (PCA) is to reduce the dimensionality of a data set consisting of a large number of interrelated variables, while retaining as much as possible of the variation present in the data set. The method generates a new set of variables, called principal components. Each principal component is a linear combination of the original variables. All the principal components are orthogonal to each other, so there is no redundant information. The principal components as a whole form an orthogonal basis for the space of the data [146, 147].

The first and second principal components are two axes in space perpendicular to each other. By projecting each observation on these axes, the resulting values form new variables, and the variances of these variables are the maximum among all possible choices of these two axes. The fundamental and basic equations of PCA are briefly explained in this section.

Consider the matrix population  $X$  composed of the  $n$  objects  $x'_j$ :

$$X = \begin{bmatrix} x_1^t \\ x_2^t \\ \vdots \\ x_n^t \end{bmatrix} = \begin{bmatrix} x_1^1 & x_1^2 & \cdots & x_1^t \\ x_1^1 & x_1^2 & \cdots & x_1^t \\ \vdots & \vdots & \ddots & \vdots \\ x_1^1 & x_1^2 & \cdots & x_1^t \end{bmatrix} \quad (6.14)$$

The data are first centered and reduced (the mean is null and the standard deviation is equal to unity for each column), the covariance matrix is then calculated as follows:

$$C_x = E[XX^t] \quad (6.15)$$

Where  $t$  represents the transpose of the matrix. The components of  $C_x$ , denoted by  $C_{kl}$  ( $k = 1, d$  and  $l = 1, d$ ), represent the covariances between the variables  $x^k$  and  $x^l$ .

$$x^k = \begin{bmatrix} x_1^k \\ x_2^k \\ \vdots \\ x_n^k \end{bmatrix}, \quad x^l = \begin{bmatrix} x_1^l \\ x_2^l \\ \vdots \\ x_n^l \end{bmatrix} \quad (6.16)$$

As the covariance matrix is a symmetric matrix, an orthogonal basis can be calculated by finding its eigenvalues and eigenvectors. The eigenvectors  $e_k$  and the corresponding eigenvalues  $\lambda_k$  are the solutions of the equation:

$$C_{Xek} = \lambda_k e_k \quad k = 1, 2, \dots, d \quad (6.17)$$

An ordered orthogonal basis can be created with the first eigenvectors, having the direction of the largest variances of the data. Therefore, directions in which the data set has the most significant amounts of energy can be found. Instead of using all the eigenvectors of the covariance matrix, we may represent the data in terms of only a few basis vectors of the orthogonal basis. If  $A_k (d \times K)$  is the matrix having the first  $k$  eigenvectors, by transforming the data vector  $X$ , we get:

$$y = XA_k \quad (6.18)$$

which represents the new coordinates of the  $n$  objects in the orthogonal coordinate system defined by the eigenvectors [132].

The PCA is applied on the matrix (with  $n \times d$  dimensions) of the time-based parameters collected from AE waveforms. The PCA projection in a two-dimension space highlights the similarities between the patterns. If the data do not overlap, automatic discrimination between the damage classes can be considered. Thus, the choice of relevant features to compose the pattern can be validated. PCA is also used here to visualize the clusters provided by the automatic classification performed with the FCM. Results using this approach are given in the Section 6.7.1.

### 6.6.3 Wavelet Analysis

The acoustic waves emitted from the composite materials are generally non-stationary and comprise overlapping transients. Therefore, characterization of the AE signals calls for an appropriate method of signal processing technique. The purpose of signal processing is to extract features of the signals that best describe the characteristics of the conditions in monitoring processes. Different processing techniques are used in accordance with the type of signals. Most researchers up to now have used time-domain AE descriptors, such as the amplitude and the energy of the signal, to characterize the development of damage [148-152]. For stationary signals, time domain statistical analysis and spectral analysis like Fourier can be used. But for AEs as transient signals, there are a number of problems in extracting characteristic features, such as loss of the useful information during transformation of a signal from one domain to another. Short-time Fourier transform was introduced to eliminate these problems, but little success was achieved. These problems have been solved by the development of time-frequency distributions.

Among the number of time-frequency distributions, wavelet transform is one of the most promising methods followed in engineering. Wavelet analysis is an appropriate tool for analyzing localized variations of power within a time series. By decomposing a time series into time-frequency space, one is able to determine both the dominant modes of variability and how those modes vary in time. Further elaboration on wavelet analysis is discussed in the following paragraphs.

Wavelet analysis is defined as the breaking up of a signal into shifted and scaled versions of the original (or mother) wavelet. Depending on the mother wavelet function, there are various discrete wavelet transform, such as the binary wavelet transform and wavelet packet transform. In the discrete wavelet decomposition procedure, the generic step splits a signal into two parts: an approximation and a detail. The approximation is the low-frequency part of the signal and the detail is the high-frequency one. In the next level, the obtained approximation itself is split into another vector of approximation coefficients and another vector of detail. This process continues until the desired level is achieved. The information lost between two consecutive approximations is captured in the detail coefficients. In the discrete wavelet process, consecutive details are never re-analyzed. In the corresponding wavelet packet situation, by contrast, each detail coefficient vector is also split into two parts using the same approach as in approximation vector splitting. It offers a better analysis. Figure 6.4 shows the packet wavelet transform tree.

Mathematically, this procedure is described by the wavelet packet transform. The wavelet transform of  $F(t)$  with respect to a wavelet  $\psi$  is expressed as [153, 154]:

$$CWT(f, \tau) = \int_{-\infty}^{+\infty} \frac{1}{\sqrt{f}} F(t) \psi^* \left( \frac{t - \tau}{f} \right) dt \quad (6.19)$$

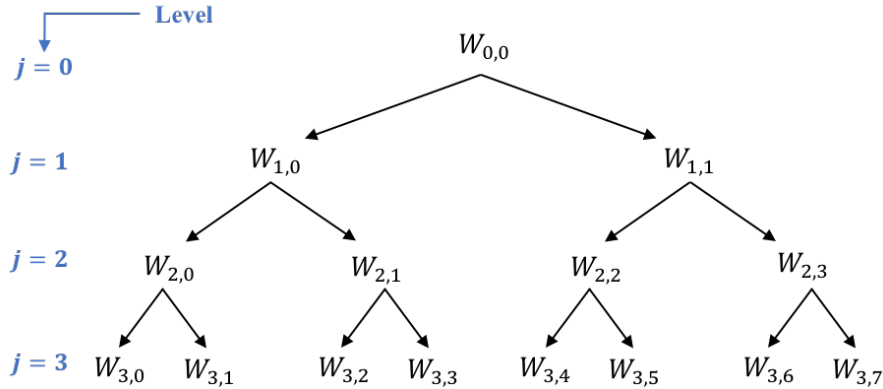


Figure 6.4. Wavelet packet transform tree.

Where  $f$  represents the frequency (or dilation),  $\tau$  the time shift (or translation), and  $*$  the complex conjugation of wavelet. The inverse wavelet transform is defined as:

$$f(t) = \frac{1}{C_\psi} \int_{-\infty}^{+\infty} \int_{-\infty}^{+\infty} \frac{1}{|f|^2} CWT(f, \tau) \psi(t) df d\tau \quad (6.20)$$

$$C_\psi = \int_{-\infty}^{+\infty} \frac{|\psi(\omega)|^2}{\omega} \quad (6.21)$$

Where  $C_\psi$  is a constant depending only on  $\psi$ .

## 6.7 Damage characterization

### 6.7.1 Multivariable analysis of AE data

One of the main problems associated with analysis of AE signals is the discrimination between the various acoustic emission sources. Among different methods of analysis, clustering is considered as a very efficient tool for discrimination and classification of data. The main purpose of data clustering is to group recorded AE data into a limited number of classes. In this section, principal component analysis and unsupervised pattern recognition analysis (fuzzy c-means clustering) are used in order to discriminate different AE sources that each represents a particular damage mechanism.

According to the number of AE parameters in the time domain, using multivariable analysis is inevitable. For this purpose, six time-based AE features are used as the component of the input factor. These are rise time, amplitude, average frequency, energy, count, and duration of the signals. Sometimes it makes sense to compute principal components for raw data. This is appropriate when all the variables are in the same units. Nevertheless, standardizing the data is preferable when the variables are in different units or when the variance of the different columns is substantial (as in this case). The feature values are normalized by dividing each column by its standard deviation. In order to visualize the results, a PCA is used in a two-dimension subspace. The percent of the total variability explained by each principal component is shown in Figure 6.5. It is observed that the first two principal components explain more than 85% of the total variability.

This means that the first two PCA components have a 2D-projection that keeps more than 85% of the variance of the 6D-data. These results indicate the ability of PCA method to reduce the dimensions and computational time of the analysis. All following results were obtained for drilling GFRP specimens at a feed rate of 31.5 mm/min and spindle speed of 315 rpm.

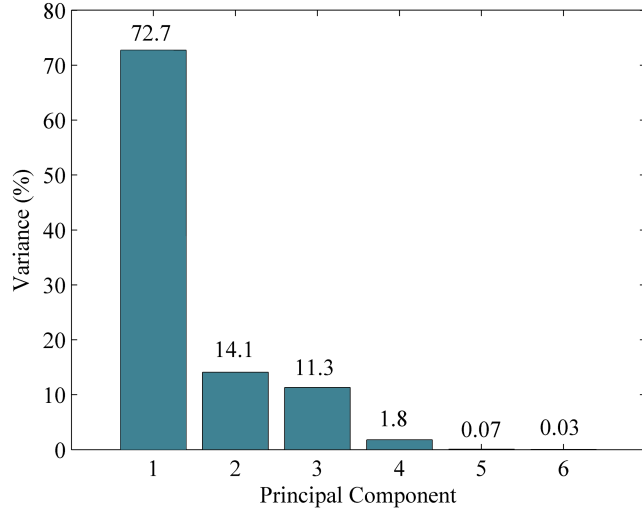


*Figure 6.5. The percent of the total variability explained by each principal component.*

In general, the main sources of acoustic energy in the drilling process are matrix cracking, fiber failure, delamination, and friction. From the fact that there are four AE sources, it appears the classification to be made should be considered as a four-class problem. Nevertheless, according to the analysis made by this classification, good results were not obtained. In another approach, detected AE signals are first classified into 3 classes that each corresponds to one of the main stages of drilling process; namely entry stage, cutting stage, and exit stage. The drilling stages are then classified into different classes according to the number of their most active damage mechanisms. Figure 6.6 illustrates clustering procedure of AE signals collected during drilling process. The most active damage mechanisms in each stage, reported in [112, 114, 155-157], are:

- Entry stage: matrix cracking and peel-up delamination
- Cutting stage: matrix cracking and fiber failure
- Exit stage: fiber failure, push-out delamination, and friction

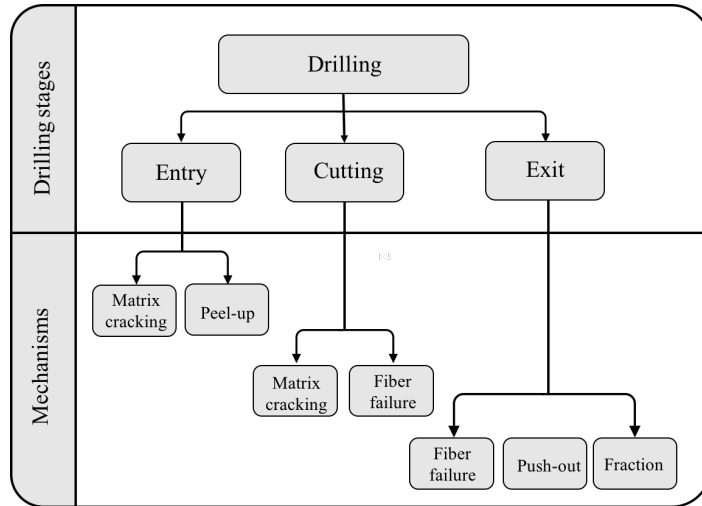


Figure 6.6. Clustering procedure of AE signals collected during drilling process.

### Step 1. Classification of AE data into three classes corresponding to drilling stages

The multivariable analysis is applied in order to discriminate the drilling stages according to their AE patterns. Drilling process is divided into three main stages and thus the FCM is applied with three clusters. A PCA is achieved in order to visualize the results in a two-dimension subspace, as shown in Figure 6.7 PCA projection shows that the distribution of the data does not overlap. Thus, classifying the data and separating the drilling stages seems permissible.

The next step is to assign the resulting clusters to the different drilling stages. For this purpose, time-based features of AE waveforms were obtained and plotted versus time, Figure 6.8. After feature extraction, amplitude distribution was found to be very similar to that of thrust force (see Figure 6.9). Thus, cluster members were colored and the amplitude diagram was regenerated, as shown in Figure 6.10. It can be observed that AE data clustered in the first class, red data, correspond to the drill entry stage, data in the second class, green data, correspond to the cutting stage, and data in the third class, blue data, correspond to the exit stage.

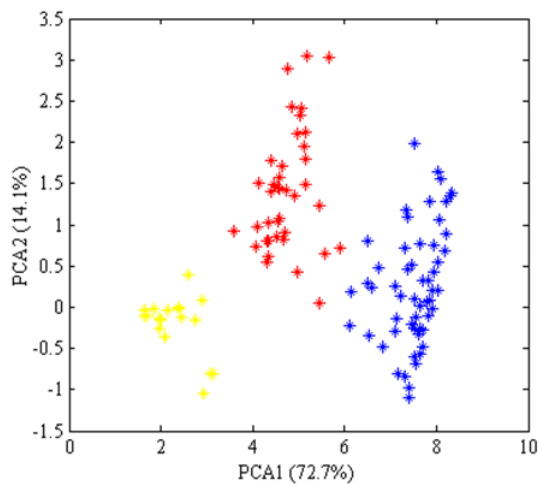
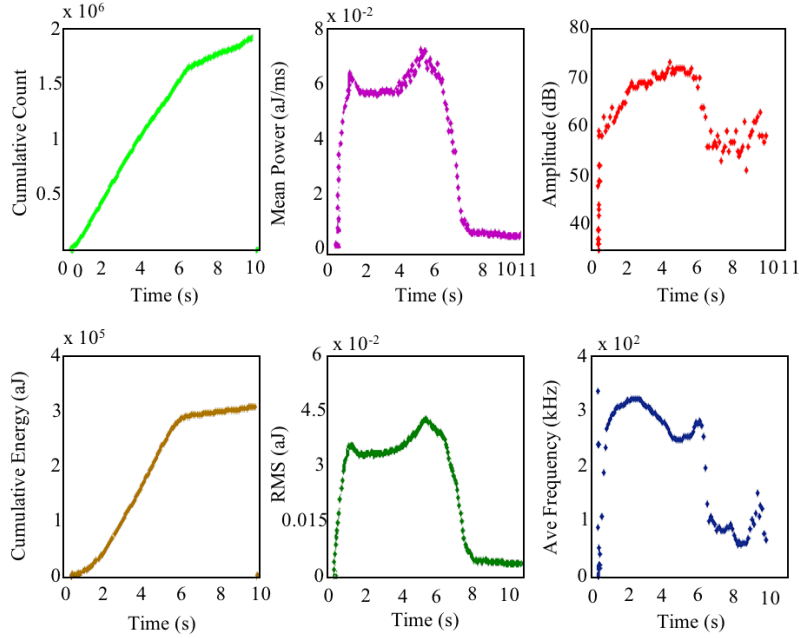
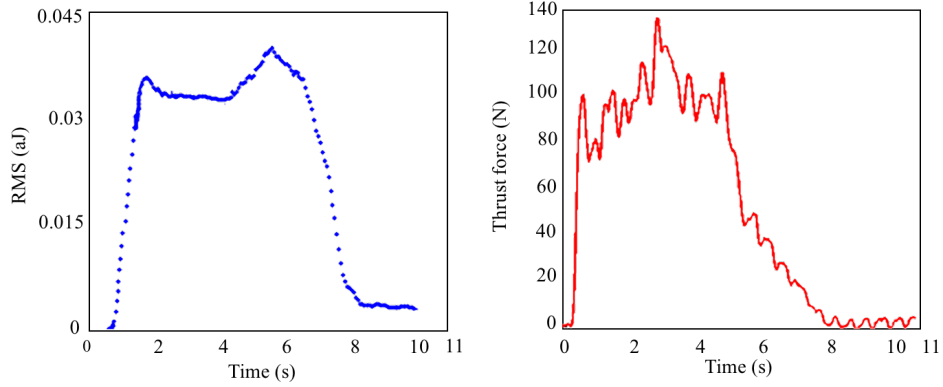


Figure 6.7. PCA visualization of the fuzzy c-means clustering.



*Figure 6.8. Time-based features of AE signals collected during drilling process; Cumulative count, Mean power, amplitude, cumulative energy, RMS, average frequency.*



*Figure 6.9. Thrust force and AE amplitude variation versus time in drilling process.*

### *Step 2. Classification of drilling stages according to their most active damage mechanisms*

After determining the main stages, each of these is classified into different classes according to the number of their most active damage mechanisms shown in Figure 6.11. Figure 6.11(a) illustrates classification of AE signals collected during the entry stage. Matrix cracking and peel-up delamination are the most predominant damage mechanisms occurring in this stage. Considering the fact that these two damage mechanisms occur in chronological order, they can be easily distinguished and discriminated; hence, purple data correspond to matrix cracking and green data correspond to delamination. Figure 6.11(b) shows classification of AE signals in the cutting stage. In this stage, assigning classes to damage mechanisms is challenging and requires the time-frequency domain analysis performed in the next section. Figure 6.11(c) demonstrates that time domain analysis is not sufficient to discriminate different damage mechanisms in the exit stage,

similar to the previous stage. However, it is noteworthy that from second nine onwards, when the tool tip is removed entirely from the laminate, friction is the only active damage mechanism. Hence, green data correspond to friction.

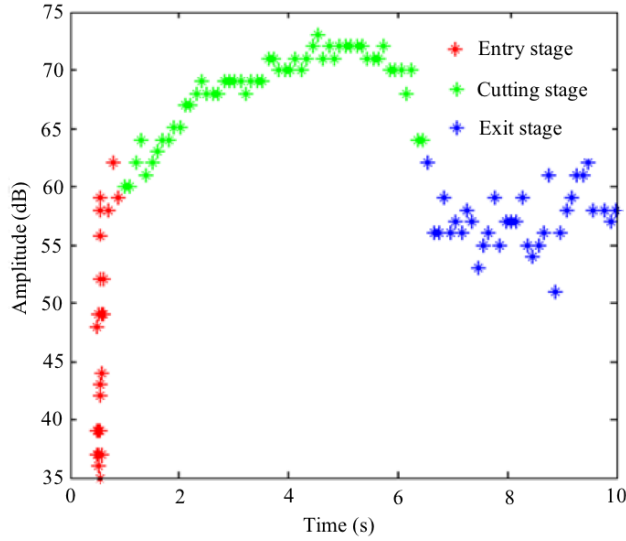


Figure 6.10. Regenerated amplitude distribution after first classification.

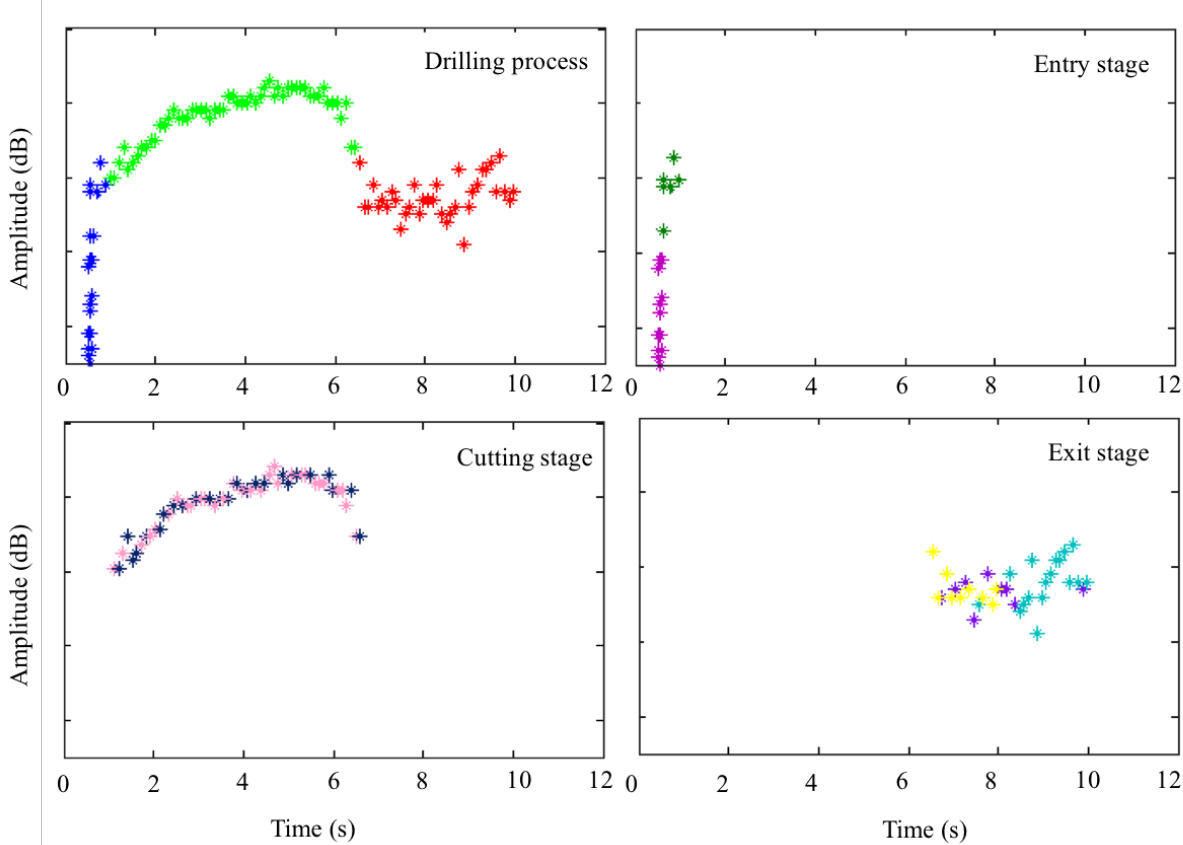


Figure 6.11. Regenerated amplitude distribution after second classification.

### 6.7.2 Wavelet-based methodology for AE analysis

As previously mentioned, in order to discriminate different damage mechanisms occurring during drilling of composite materials time domain analysis is not sufficient and time-frequency analysis is required because of the simultaneous occurrence of damage mechanisms. Considering the fact that each damage mechanism has a specific frequency range, time-frequency analysis of AE signals can be effective. For this purpose, wavelet packet transform, a powerful tool in the time-frequency domain, is used.

The wavelet packet theory was introduced in Section 6.6.3. It was mentioned that a signal can be decomposed into a set of wavelet components and each component has a specific frequency range. In this study, to analyze AE signals, the energy criteria are employed because of the different distribution of energy in each component which can be related to a specific damage mechanism. The energy content of each component is determined after the decomposition of all AE signals. This is mathematically expresses as below:

$$EC_i(t) = \sum_{\tau=t_0}^t (f_i(\tau))^2 \quad (6.22)$$

Where  $EC_i(t)$  represents the energy of component  $i$  at a certain level. The total energy of a given level is defined as the summation of the energy for all the components. In this study, the ration of energy at different components to the total energy is determined to find the energy percentage for each component.

$$EPC_i(t) = \frac{EC_i(t)}{EC_{Total}(t)} \quad i = 1, 2, \dots, 2^j \quad (6.23)$$

Where  $j$  is the level of decomposition and  $i$  the number of components.

Based on the wavelet packet transform theory, two parameters are very important; the number of levels and type of mother wavelet. There are two methods to select the number of levels:

- (a) according to mathematical criterion called entropy
- (b) systematic trials; the number of levels is set to the optimum number as it is evident that less is insufficient and more is redundant.

Here, the second method is chosen and the number of levels is set to three ( $j = 3$ ).

To choose a mother wavelet that well describes the AE signatures, practically all available standard mother wavelets were visually examined. After visual inspection, it was found that db20 wavelet (a member of the Daubechies wavelet family) is most similar to the recorded AE signature.

According to the Nyquist sampling theorem, the signal must be sampled at twice the highest frequency contained in the signal. Therefore, in this case, the sampling frequency is set to 1 MHz and the transformed signals frequency must be up to 500 kHz. As the number of levels is to three ( $j = 3$ ), the number of components will be eight ( $i = 2^3$ ). The frequency ranges for these

components are: [0-62.5], [62.5,125], [125-187.5], [187.5-250], [250-312.5], [312.5-375], [375-437.5], and [437.5-500] kHz.

For the analysis of AE waveforms, MATLAB software was used. The wavelet packet transform was applied to all signals. The details of the results obtained are shown in the plots below. Figure 6.12 shows the component energy percentage,  $EPC_i(t)$ , of the three-level wavelet packet decomposition of AE signals emitted during the exit stage. In this figure, the vertical coordinate is the energy and the horizontal coordinate is the waveform number. The fast Fourier transform (FFT) method was used to obtain the frequency content of the decomposed signals. The frequency contents of each component of the decomposed signals emitted during the exit stage are shown in Figure 6.13, showing that the frequency range of the decomposed components increased from one component to another.

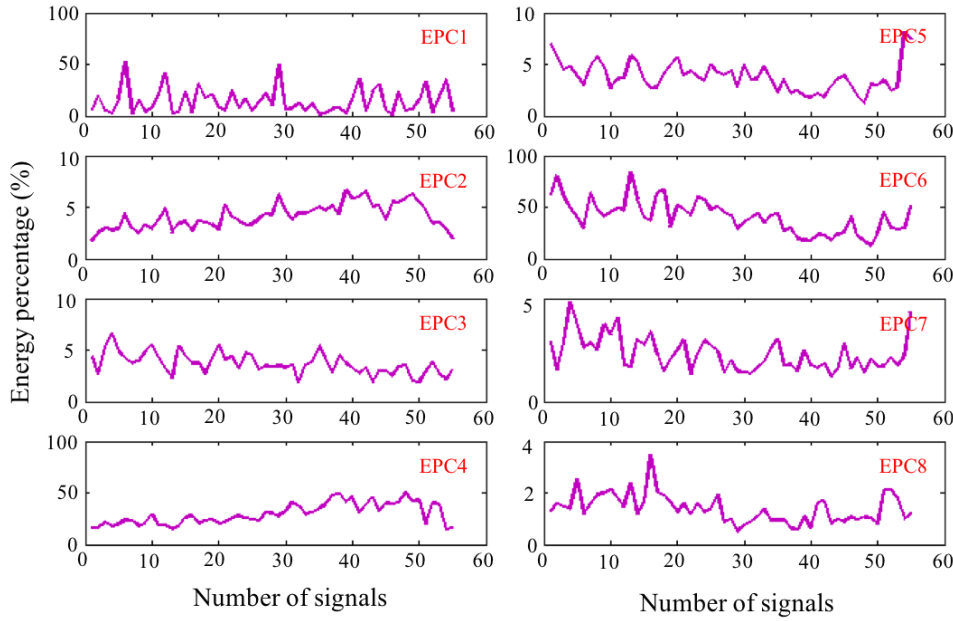


Figure 6.12. Energy percentage of each component of level 3, energy (%) vs. waveform number.

The frequency range and energy percentage for clustered stages are reported in Table 6.1. According to the table, components 1, 2, 4, and 6 have higher content than other components. These components, each of which has a certain frequency range, correspond to four main damage mechanism. The remaining issue is to find this correlation according to the frequency distribution. Different distribution in the dominant frequency range, for dissimilar failures, can be clarified by the fact that elastic acoustic velocities and intrinsic frequencies are related to the density and elastic modulus according to Eq. (6.24) [158]:

$$f \propto C \propto \sqrt{\frac{E}{\rho}} \quad (6.24)$$

Where  $f$  is the frequency,  $C$  the elastic acoustic velocity,  $\rho$  the density, and  $E$  the elastic modulus. In this regard, friction creates the lowest frequency range compared with the other damage mechanisms and the highest frequency range will be achieved during fiber breakage.

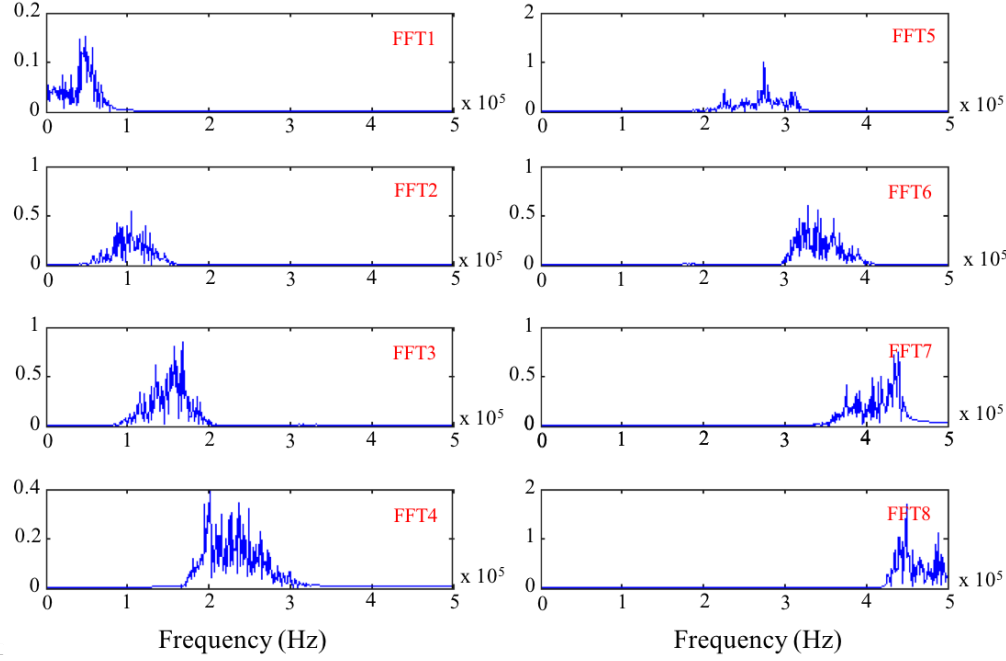
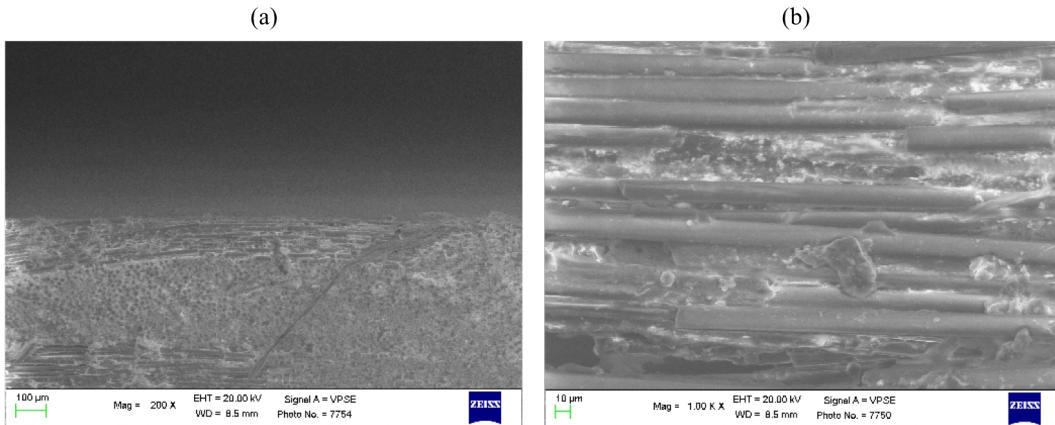


Figure 6.13. FFT of the decomposed components of level 3, FFT amplitude ( $mV^2/Hz$ ) vs. frequency (Hz).

Table 6.1. Frequency range and energy percentage for eight components of level 3.

Stage	EPC1	EPC2	EPC3	EPC4	EPC5	EPC6	EPC7	EPC8
entry	4.2	26.5	7.1	45.9	4.6	6.2	3.8	1.7
cutting	5.2	23.5	5.4	4.6	3.8	51.2	4.2	2.1
exit	14.2	4.2	3.7	29.6	3.9	40.6	2.3	1.4

As shown in Table 6.1, for the entry stage, EPC2 and EPC4 have the highest energy percentages among other components. These two components are attributed to the most active damage mechanisms in this state, i.e. matrix cracking and delamination (see Figure 6.6). For this purpose, two complimentary tests were designed and carried out; the pure epoxy resin drilling test and the delamination test. For the former one, Araldite LY556 epoxy resin sheet with a thickness of 5 mm was drilled and generated AE signals were recorded. After analyzing the signals in time and time-frequency domains, a frequency distribution accordant with component 2 (EPC2) was obtained. Figure 6.14(a) shows the SEM image of matrix cracks during the entry stage. Therefore, component 2 with the frequency distribution of [62.5-125] kHz is associated with matrix cracking.



*Figure 6.14. SEM images showing (a) matrix cracking and delamination during entry stage and (b) fiber failure during cutting stage.*

Drilling induced delamination occurs both at the entrance and exit sides of the workpiece. Delamination on the exit surface, generally referred to as push-out, is as a rule more extensive, and is consequently considered the most dangerous. When the drill bit approaches the hole exit side, the uncut plies beneath the drill bit becomes more susceptible to deformation due to the decrease of their thickness. Eventually, push-out delamination appears at the drilled hole exit periphery if the thrust force applied to the uncut plies exceeds the inter-ply bonding strength. For the delamination test, 4 mm holes were first drilled in GRFP specimens and they were then subjected to quasi-static indentation test. Thus, the behavior of delamination failure at the drilled hole exit was simulated and investigated. After processing of AE signals, a frequency distribution accordant with component 4 (EPC4) was achieved. Therefore, component 4 with the frequency distribution of [187.5-250] kHz is associated with delamination.

The most prominent damage mechanisms during the cutting stage are matrix cracking and fiber breakage, the former being associated with component 2. According to Table 6.1, fiber breakage seems to be attributed to component 6 (EPC6). This hypothesis is supported by the fact that fiber breakage creates a higher frequency range compared with the other damage mechanisms according to Eq. (6.24). Hence, component 6 with the frequency distribution of [312.5-375] kHz is associated with fiber breakage. Figure 6.14(b) shows the SEM image of fiber failure during the cutting stage.

Friction mechanism has a lower frequency distribution than other mechanisms. Although this mechanism is active from the beginning to the end of the process, from second 9 onwards, when the tool tip is completely out of the laminate, friction is the only active mechanism. After discrimination and frequency analysis of these signals, the frequency distribution of the friction mechanism was obtained which is in accordance with component 1 (EPC1). Hence, component 1 with the frequency distribution of [0-62.5] kHz is associated with friction.

The result obtained are in good agreement with the results of other researchers. Marec *et al.* [132] reported a frequency range of 50-150 kHz for matrix cracking during creep tensile test of glass/polyester composite materials. Loutas *et al.* [159] studied damage evolution in center-holed

glass/polyester composites under quasi-static loading using time-frequency analysis of acoustic emission monitored waveforms. They showed a frequency range of 300-400 kHz for fiber failure. Suzuki *et al.* [160] observed the following correlation between failure mechanisms and AE frequency in glass/polyester composites: matrix cracking 30-150 kHz and fiber breakage 300-400 kHz. Groot *et al.* [161] studied on carbon/epoxy material in the form of a unidirectional composite to determine the frequency content of acoustic emission signals. By using different types of specimen, it was concluded that matrix cracking released frequencies between 90 and 180 kHz and fiber failure frequencies above 300 kHz.

# CHAPTER 7

## 7 CONCLUSIONS AND FUTURE WORK

This chapter will summarize the findings and present some recommendations to further the understanding of drilling composites.

### 7.1 Conclusions

Advanced composite materials are characterized by having a combination of high specific strength and stiffness. Due to these distinctive properties, they have been widely used in many different applications, such as automobile, aircraft and sporting goods. With the growing application of composites in different industrial applications, there is a great need to understand the issues associated with the manufacture of composite components. The existing manufacturing technique of fabricating to near-net shape is incomplete unless the component is subjected to secondary machining operations. Among all machining operations, conventional drilling is the most frequently used process in composite structures, as the use of bolts, rivets or screws is required to join the parts. But, drilling is quite difficult and challenging due to high tendency of composite laminates to delamination. This dissertation deals with the characterization, modeling, and monitoring of drilling process of composite materials through various experimental and analytical investigations.

Drilling induced delamination has been recognized as a major problem during drilling of composite materials. The size of the delamination zone has been shown to be related to the thrust force. However, thrust force strongly depends on drilling parameters and it is not possible to control it directly. Thrust force can be correlated with feed rate, the most important parameter affecting thrust force. Analytical models were developed which predicts critical thrust force and critical feed rate above which the delamination crack begins to propagate in the drilling of multi-directional laminated composites. The delamination zone was modeled as a circular plate, with clamped edge and subjected to different load profiles for cutting lips and chisel edge regions. Based on fracture mechanics, classical laminate theory and orthogonal cutting mechanics, expressions were obtained for critical thrusts and critical feed rates at different ply locations. A variable feed rate strategy was then suggested with the aim of avoiding delamination while drilling in a time-optimal fashion. The proposed models have been verified by experiments and compared with the existing models. Based on the results, the predicted values by the proposed models show satisfactory agreement with the experimentally measured values. It was found that the new developed models provide more accurate and rigorous results than the formers.

Quality of holes and drilling induced damage when drilling fiber reinforced composite laminates were experimentally studied. The influence of drilling parameters, tool geometry, and workpiece

material on the resulting quality of the produced hole and damage were studied through qualitative measurements and examinations. Several quality responses were measured as indices of drilling performance, including thrust force, delamination size, residual compression strength, and residual flexural strength. Two sets of experiments were designed and carried out; E-glass/epoxy composites were drilled and then comparison tested to evaluate their residual compressive strength, E-glass fiber-epoxy composites reinforced with functionalized multi-walled carbon nanotubes were drilled and then bending tested to determine their residual bending strength.

First, drilling thrust force was comprehensively studied from drill entry into the workpiece to full engagement and drill exit from the material. The behavior of drilled specimens under compression test was described. The results show a meaningful relation between delamination factor as an index of damage size and residual compressive strength. Two drilling parameters, namely feed rate and spindle speed, at three levels based on general full factorial design were studied. The effect of feed rate on residual compressive strength was found to be greater than that of the cutting speed. In addition, the relationship between feed rate, spindle speed and residual compressive strength was presented in a polynomial regression model.

Secondly, experiments were conducted to analyze the thrust force, delamination factor and residual flexural strength in the drilling of woven E-glass fiber-epoxy composites reinforced with functionalized multi-walled carbon nanotubes. Analysis of variance and Taguchi *S/N* ratio analysis were performed to investigate the influence of input parameters on each individual drilling characteristic. In addition, the orthogonal array with grey relational analysis was employed to simultaneously optimize the multiple performance characteristics of the drilling process. The Taguchi based grey relational analysis proved that this approach can be successfully applied to optimize the composite drilling process with multiple performance characteristics.

An experimental study of acoustic emission as a tool for in-process monitoring and nondestructive evaluation of drilling of composites was conducted. Acoustic emission was used to examine the relationship between signal response and drilling induced damages. A procedure for identification and discrimination of different damage mechanisms based on the analysis of AE signals was presented. Principal component analysis and fuzzy C-means clustering were used to divide the drilling process into three main stages, namely entry stage, cutting stage, and exit stage. Assignment of the classes to different drilling stages was done based on different amplitude ranges. The main sources of acoustic energy in the drilling process were identified as matrix cracking, fiber failure, delamination, and friction. After determining the main stages, each drilling stage was classified into different classes according to the number of their most active damage mechanisms. Considering the facts that acoustic emission signals in composite materials are not stationary and the temporal descriptors are not always relevant, wavelet analysis of AE signals was applied in order to improve the discrimination procedure. The fast Fourier transform method was also employed to obtain the frequency content of the decomposed signals. Based on the results, frequency distribution and energy percentage of most important damage mechanisms occurring during drilling were determined. Finally, it was concluded that acoustic emission has a great

potential for the application of online monitoring and damage characterization in the drilling of composite structures.

## 7.2 Recommendations for future works

Analytical and experimental investigations presented throughout the present study suggest the following areas for further research on machining of composite materials;

- (1) The current study attempted to address and solve the delamination problem associated with conventional drilling of composites. Delamination is a concern in other hole-making processes such as water-jet drilling. The approach used in this study can be extended to other machining processes.
- (2) Drilling tests are performed using standard drill geometries. Cutting mechanisms depend on not only workpiece materials but also tool property. The various geometry types of drills can be used to examine the drill geometry effect on the composite drilling. Special drill bits should be designed to reduce cutting forces and associated damage.
- (3) Drilling laminated composites typically causes multiple fracture modes including fiber debonding, microcrack growth, and nonlinear deformation such as bulging. This observation indicates that more sophisticated modeling of the drilling process is required to predict the critical thrust force more accurately.
- (4) The cutting temperature generated during any machining process is usually high enough to affect some of material properties. Therefore, a parametric study which assesses the effects of elevated temperature and moisture absorption on the performance of composites should be characterized and incorporated into the process model.
- (5) It is recommended that a study be conducted which assesses the effect of drilling induced damage on the performance of drilled specimens subjected to fatigue loads. This is needed since many applications involving mechanically fastened joints are loaded in fatigue rather than subjected to static loading conditions.
- (6) More analysis should be carried out in the analysis and processing of acoustic emission signals to correlate signal signature to drilling induced damage towards developing in process monitoring when drilling composite laminates.

## Bibliography

- [1] Chung DDL. Composite materials: Science and applications: Springer London, 2010.
- [2] Campbell FC. Structural composite materials: ASM international, 2010.
- [3] Sheikh-Ahmad JY. Machining of polymer composites: Springer, 2009.
- [4] Hocheng H. Machining technology for composite materials: principles and practice: Elsevier, 2011.
- [5] Liu D, Tang Y, Cong WL. A review of mechanical drilling for composite laminates. *Composite Structures*. 2012;94:1265-79.
- [6] El-Sonbaty I, Khashaba UA, Machaly T. Factors affecting the machinability of GFR/epoxy composites. *Composite Structures*. 2004;63:329-38.
- [7] Capello E. Workpiece damping and its effect on delamination damage in drilling thin composite laminates. *Journal of Materials Processing Technology*. 2004;148:186-95.
- [8] Davim JP, Reis P, António CC. Experimental study of drilling glass fiber reinforced plastics (GFRP) manufactured by hand lay-up. *Composites Science and Technology*. 2004;64:289-97.
- [9] Tsao CC, Hocheng H. Computerized tomography and C-Scan for measuring delamination in the drilling of composite materials using various drills. *International Journal of Machine Tools and Manufacture*. 2005;45:1282-7.
- [10] Arul S, Vijayaraghavan L, Malhotra SK, Krishnamurthy R. The effect of vibratory drilling on hole quality in polymeric composites. *International Journal of Machine Tools and Manufacture*. 2006;46:252-9.
- [11] Gaitonde VN, Karnik SR, Rubio JC, Correia AE, Abrão AM, Davim JP. Analysis of parametric influence on delamination in high-speed drilling of carbon fiber reinforced plastic composites. *Journal of Materials Processing Technology*. 2008;203:431-8.
- [12] Rawat S, Attia H. Characterization of the dry high speed drilling process of woven composites using Machinability Maps approach. *CIRP Annals - Manufacturing Technology*. 2009;58:105-8.
- [13] Khashaba UA, El-Sonbaty IA, Selmy AI, Megahed AA. Machinability analysis in drilling woven GFR/epoxy composites: Part I – Effect of machining parameters. *Composites Part A: Applied Science and Manufacturing*. 2010;41:391-400.
- [14] Davim JP, Reis P. Drilling carbon fiber reinforced plastics manufactured by autoclave—experimental and statistical study. *Materials & Design*. 2003;24:315-24.
- [15] Sardiñas RQ, Reis P, Davim JP. Multi-objective optimization of cutting parameters for drilling laminate composite materials by using genetic algorithms. *Composites Science and Technology*. 2006;66:3083-8.
- [16] Khashaba UA. Delamination in drilling GFR-thermoset composites. *Composite Structures*. 2004;63:313-27.
- [17] Karnik SR, Gaitonde VN, Rubio JC, Correia AE, Abrão AM, Davim JP. Delamination analysis in high speed drilling of carbon fiber reinforced plastics (CFRP) using artificial neural network model. *Materials & Design*. 2008;29:1768-76.
- [18] Campos Rubio J, Abrao AM, Faria PE, Correia AE, Davim JP. Effects of high speed in the drilling of glass fibre reinforced plastic: Evaluation of the delamination factor. *International Journal of Machine Tools and Manufacture*. 2008;48:715-20.

- [19] Kilickap E. Optimization of cutting parameters on delamination based on Taguchi method during drilling of GFRP composite. *Expert Systems with Applications*. 2010;37:6116-22.
- [20] Tsao CC, Hocheng H. Taguchi analysis of delamination associated with various drill bits in drilling of composite material. *International Journal of Machine Tools and Manufacture*. 2004;44:1085-90.
- [21] Davim JP, Reis P. Study of delamination in drilling carbon fiber reinforced plastics (CFRP) using design experiments. *Composite Structures*. 2003;59:481-7.
- [22] Khashaba UA, El-Sonbaty IA, Selmy AI, Megahed AA. Machinability analysis in drilling woven GFR/epoxy composites: Part II – Effect of drill wear. *Composites Part A: Applied Science and Manufacturing*. 2010;41:1130-7.
- [23] Alagusundaramoorthy P, Veera Sudarsana Reddy R. Testing and evaluation of GFRP composite deck panels. *Ocean Engineering*. 2008;35:287-93.
- [24] Kim D, Ramulu M. Drilling process optimization for graphite/bismaleimide–titanium alloy stacks. *Composite Structures*. 2004;63:101-14.
- [25] Paulo Davim J, Reis P, Conceição António C. Drilling fiber reinforced plastics (FRPs) manufactured by hand lay-up: influence of matrix (Viapal VUP 9731 and ATLAC 382-05). *Journal of Materials Processing Technology*. 2004;155–156:1828-33.
- [26] Faraz A, Biermann D, Weinert K. Cutting edge rounding: An innovative tool wear criterion in drilling CFRP composite laminates. *International Journal of Machine Tools and Manufacture*. 2009;49:1185-96.
- [27] Tsao CC, Hocheng H. Effect of tool wear on delamination in drilling composite materials. *International Journal of Mechanical Sciences*. 2007;49:983-8.
- [28] Tsao CC. Experimental study of drilling composite materials with step-core drill. *Materials & Design*. 2008;29:1740-4.
- [29] Hocheng H, Tsao CC. Effects of special drill bits on drilling-induced delamination of composite materials. *International Journal of Machine Tools and Manufacture*. 2006;46:1403-16.
- [30] Velayudham A, Krishnamurthy R. Effect of point geometry and their influence on thrust and delamination in drilling of polymeric composites. *Journal of Materials Processing Technology*. 2007;185:204-9.
- [31] Seif M, Khashaba U, Rojas-Oviedo R. Measuring delamination in carbon/epoxy composites using a shadow moiré laser based imaging technique. *Composite Structures*. 2007;79:113-8.
- [32] Durão LMP, de Moura MFSF, Marques AT. Numerical prediction of delamination onset in carbon/epoxy composites drilling. *Engineering Fracture Mechanics*. 2008;75:2767-78.
- [33] Durão LMP, Gonçalves DJS, Tavares JMRS, de Albuquerque VHC, Aguiar Vieira A, Torres Marques A. Drilling tool geometry evaluation for reinforced composite laminates. *Composite Structures*. 2010;92:1545-50.
- [34] Chen W-C. Some experimental investigations in the drilling of carbon fiber-reinforced plastic (CFRP) composite laminates. *International Journal of Machine Tools and Manufacture*. 1997;37:1097-108.

- [35] Davim JP, Rubio JC, Abrao AM. A novel approach based on digital image analysis to evaluate the delamination factor after drilling composite laminates. Composites Science and Technology. 2007;67:1939-45.
- [36] Hocheng H, Tsao CC. The path towards delamination-free drilling of composite materials. Journal of Materials Processing Technology. 2005;167:251-64.
- [37] Stone R, Krishnamurthy K. A neural network thrust force controller to minimize delamination during drilling of graphite-epoxy laminates. International Journal of Machine Tools and Manufacture. 1996;36:985-1003.
- [38] Tagliaferri V, Caprino G, Diterlizzi A. Effect of drilling parameters on the finish and mechanical properties of GFRP composites. International Journal of Machine Tools and Manufacture. 1990;30:77-84.
- [39] Ramulu M, Branson T, Kim D. A study on the drilling of composite and titanium stacks. Composite Structures. 2001;54:67-77.
- [40] Krishnaraj V, Zitoune R, Davim JP. Drilling of polymer-matrix composites: Springer, 2013.
- [41] Dharan CKH, Won MS. Machining parameters for an intelligent machining system for composite laminates. International Journal of Machine Tools and Manufacture. 2000;40:415-26.
- [42] Hocheng H, Dharan CKH. Delamination during drilling in composite laminates. Journal of Manufacturing Science and Engineering. 1990;112:236-9.
- [43] Jain S, Yang DC. Delamination-free drilling of composite laminates. Journal of Engineering for Industry. 1994;116:475-81.
- [44] Jain S, Yang DC. Effects of feedrate and chisel edge on delamination in composites drilling. TRANSACTIONS-AMERICAN SOCIETY OF MECHANICAL ENGINEERS JOURNAL OF ENGINEERING FOR INDUSTRY. 1993;115:398-.
- [45] Upadhyay PC, Lyons JS. On the evaluation of critical thrust for delamination-free drilling of composite laminates. Journal of Reinforced Plastics and Composites. 1999;18:1287-303.
- [46] Lachaud F, Piquet R, Collombet F, Surcin L. Drilling of composite structures. Composite Structures. 2001;52:511-6.
- [47] Zhang LB, Wang LJ, Liu XY. A mechanical model for predicting critical thrust forces in drilling composite laminates. Proceedings of the Institution of Mechanical Engineers, Part B: Journal of Engineering Manufacture. 2001;215:135-46.
- [48] Gururaja S, Ramulu M. Modified Exit-ply Delamination Model for Drilling FRPs. Journal of composite materials. 2009;43:483-500.
- [49] Timoshenko S, Woinowsky-Krieger S. Theory of plates and shells: McGraw-Hill, 1959.
- [50] Hocheng H, Tsao CC. Comprehensive analysis of delamination in drilling of composite materials with various drill bits. Journal of Materials Processing Technology. 2003;140:335-9.
- [51] Velayudham A, Krishnamurthy R, Soundarapandian T. Evaluation of drilling characteristics of high volume fraction fibre glass reinforced polymeric composite. International Journal of Machine Tools and Manufacture. 2005;45:399-406.
- [52] Singh I, Bhatnagar N, Viswanath P. Drilling of uni-directional glass fiber reinforced plastics: Experimental and finite element study. Materials & Design. 2008;29:546-53.

- [53] Abrão AM, Rubio JCC, Faria PE, Davim JP. The effect of cutting tool geometry on thrust force and delamination when drilling glass fibre reinforced plastic composite. *Materials & Design*. 2008;29:508-13.
- [54] Liu D, Xu HH, Zhang CY, Yan HJ. Drilling force in high speed drilling carbon fibre reinforced plastics (CFRP) using half core drill. *Advanced Materials Research: Trans Tech Publ*; 2010. p. 729-32.
- [55] Mohan NS, Ramachandra A, Kulkarni SM. Influence of process parameters on cutting force and torque during drilling of glass-fiber polyester reinforced composites. *Composite Structures*. 2005;71:407-13.
- [56] Murphy C, Byrne G, Gilchrist MD. The performance of coated tungsten carbide drills when machining carbon fibre-reinforced epoxy composite materials. *Proceedings of the Institution of Mechanical Engineers, Part B: Journal of Engineering Manufacture*. 2002;216:143-52.
- [57] Rawat S, Attia H. Wear mechanisms and tool life management of WC-Co drills during dry high speed drilling of woven carbon fibre composites. *Wear*. 2009;267:1022-30.
- [58] Khashaba UA, Seif MA, Elhamid MA. Drilling analysis of chopped composites. *Composites Part A: Applied Science and Manufacturing*. 2007;38:61-70.
- [59] Zitoune R, Krishnaraj V, Collombet F. Study of drilling of composite material and aluminium stack. *Composite Structures*. 2010;92:1246-55.
- [60] Khashaba U. Drilling of polymer matrix composites: A review. *Journal of composite materials*. 2013;47:1817-32.
- [61] Kavad BV, Pandey AB, Tadavi MV, Jakharia HC. A review paper on effects of drilling on glass fiber reinforced plastic. *Procedia Technology*. 2014;14:457-64.
- [62] Bandhu D, Sangwan SS, Verma M. A review of drilling of carbon fiber reinforced plastic composite materials. 2014.
- [63] Abrão AM, Faria PE, Rubio JCC, Reis P, Davim JP. Drilling of fiber reinforced plastics: A review. *Journal of Materials Processing Technology*. 2007;186:1-7.
- [64] Tsao CC, Hocheng H. The effect of chisel length and associated pilot hole on delamination when drilling composite materials. *International Journal of Machine Tools and Manufacture*. 2003;43:1087-92.
- [65] Won MS, Dharan CKH. Chisel edge and pilot hole effects in drilling composite laminates. *Journal of Manufacturing Science and Engineering*. 2002;124:242-7.
- [66] Mohan NS, Ramachandra A, Kulkarni SM. Machining of fiber-reinforced thermoplastics: Influence of feed and drill size on thrust force and torque during drilling. *Journal of Reinforced Plastics and Composites*. 2005;24:1247-57.
- [67] Che D, Saxena I, Han P, Guo P, Ehmann KF. Machining of carbon fiber reinforced plastics/polymers: A literature review. *Journal of Manufacturing Science and Engineering*. 2014;136:034001.
- [68] Latha B, Senthilkumar VS, Palanikumar K. Influence of drill geometry on thrust force in drilling GFRP composites. *Journal of Reinforced Plastics and Composites*. 2011;30:463-72.
- [69] Grilo TJ, Paulo RMF, Silva CRM, Davim JP. Experimental delamination analyses of CFRPs using different drill geometries. *Composites Part B: Engineering*. 2013;45:1344-50.

- [70] Piquet R, Ferret B, Lachaud F, Swider P. Experimental analysis of drilling damage in thin carbon/epoxy plate using special drills. Composites Part A: Applied Science and Manufacturing. 2000;31:1107-15.
- [71] Marques AT, Durão LM, Magalhães AG, Silva JF, Tavares JMRS. Delamination analysis of carbon fibre reinforced laminates: Evaluation of a special step drill. Composites Science and Technology. 2009;69:2376-82.
- [72] Hocheng H, Tsao CC, Chen HT. Utilizing internal icing force to reduce delamination in drilling composite tubes. Composite Structures. 2016;139:36-41.
- [73] Rajamurugan TV, Shanmugam K, Palanikumar K. Analysis of delamination in drilling glass fiber reinforced polyester composites. Materials & Design. 2013;45:80-7.
- [74] Palanikumar K, Muniaraj A. Experimental investigation and analysis of thrust force in drilling cast hybrid metal matrix (Al-15%SiC-4%graphite) composites. Measurement. 2014;53:240-50.
- [75] Park K-H, Beal A, Kim D, Kwon P, Lantrip J. Tool wear in drilling of composite/titanium stacks using carbide and polycrystalline diamond tools. Wear. 2011;271:2826-35.
- [76] Arul S, Vijayaraghavan L, Malhotra SK, Krishnamurthy R. Influence of tool material on dynamics of drilling of GFRP composites. The International Journal of Advanced Manufacturing Technology. 2006;29:655-62.
- [77] Ramesh M, Palanikumar K, Reddy KH. Influence of tool materials on thrust force and delamination in drilling sisal-glass fiber reinforced polymer (S-GFRP) composites. Procedia Materials Science. 2014;5:1915-21.
- [78] Spur G, Wunsch U. Turning of fiber-reinforced plastics. Manuf Rev. 1988;1:124-9.
- [79] Varatharajan R, Malhotra SK, Vijayaraghavan L, Krishnamurthy R. Mechanical and machining characteristics of GF/PP and GF/Polyester composites. Materials Science and Engineering: B. 2006;132:134-7.
- [80] Mathew J, Ramakrishnan N, Naik NK. Trepanning on unidirectional composites: delamination studies. Composites Part A: Applied Science and Manufacturing. 1999;30:951-9.
- [81] Won MS, Dharan CKH. Drilling of aramid and carbon fiber polymer composites. Journal of Manufacturing Science and Engineering. 2002;124:778-83.
- [82] Fernandes M, Cook C. Drilling of carbon composites using a one shot drill bit. Part II: empirical modeling of maximum thrust force. International Journal of Machine Tools and Manufacture. 2006;46:76-9.
- [83] Tsao CC, Hocheng H. Parametric study on thrust force of core drill. Journal of Materials Processing Technology. 2007;192–193:37-40.
- [84] Tsao C. Prediction of thrust force of step drill in drilling composite material by Taguchi method and radial basis function network. The International Journal of Advanced Manufacturing Technology. 2008;36:11-8.
- [85] Tsao C, Hocheng H. Effects of exit back-up on delamination in drilling composite materials using a saw drill and a core drill. International Journal of Machine Tools and Manufacture. 2005;45:1261-70.
- [86] Fernandes M, Cook C. Drilling of carbon composites using a one shot drill bit. Part I: Five stage representation of drilling and factors affecting maximum force and torque. International Journal of Machine Tools and Manufacture. 2006;46:70-5.

- [87] Shyha I, Soo SL, Aspinwall D, Bradley S. Effect of laminate configuration and feed rate on cutting performance when drilling holes in carbon fibre reinforced plastic composites. *Journal of Materials Processing Technology*. 2010;210:1023-34.
- [88] Wu S. Multifacet drills. *Handbook of High-Speed Machining Technology*: Springer; 1985. p. 305-16.
- [89] Wu SM, Shen JM. Mathematical model for multifacet drills. *Journal of Engineering for Industry*. 1983;105:173-82.
- [90] Friedrich M, Burant R, McGinty M. Cutting tools/drills. V.point styles and applications. *Mfg Eng*. 1979;83:29.
- [91] Ghasemi Nejhad MN, Chou TW. Compression behaviour of woven carbon fibre-reinforced epoxy composites with moulded-in and drilled holes. *Composites*. 1990;21:33-40.
- [92] Persson E, Eriksson I, Zackrisson L. Effects of hole machining defects on strength and fatigue life of composite laminates. *Composites Part A: Applied Science and Manufacturing*. 1997;28:141-51.
- [93] Capello E, Tagliaferri V. Drilling damage of GFRP and residual mechanical behavior-part I: drilling damage generation. *Journal of composites technology & research*. 2001;23:122-30.
- [94] Capello E, Tagliaferri V. Drilling damage of GFRP and residual mechanical behavior-part II: static and cyclic bearing loads. *Journal of composites technology & research*. 2001;23:131-7.
- [95] Singh I, Bhatnagar N. Drilling-induced damage in uni-directional glass fiber reinforced plastic (UD-GFRP) composite laminates. *The International Journal of Advanced Manufacturing Technology*. 2006;27:877-82.
- [96] Kishore RA, Tiwari R, Dvivedi A, Singh I. Taguchi analysis of the residual tensile strength after drilling in glass fiber reinforced epoxy composites. *Materials & Design*. 2009;30:2186-90.
- [97] Zarif Karimi N, Heidary H, Ahmadi M. Residual tensile strength monitoring of drilled composite materials by acoustic emission. *Materials & Design*. 2012;40:229-36.
- [98] Ehmann KF, Kapoor SG, DeVor RE, Lazoglu I. Machining process modeling: A review. *Journal of Manufacturing Science and Engineering*. 1997;119:655-63.
- [99] Merchant ME. Mechanics of the metal cutting process. I. Orthogonal cutting and a type 2 chip. *Journal of applied physics*. 1945;16:267-75.
- [100] Oxford Jr C. On the drilling of metals 1: basic mechanics of the process. *Trans ASME*. 1955;77:103-11.
- [101] Shaw MC. The mechanics of three-dimensional cutting operations: MIT, 1951.
- [102] Oxley PLB. The mechanics of machining: An analytical approach to assesing machinability: Ellis Horwood, 1989.
- [103] Chandrasekharan V, Kapoor SG, DeVor RE. A mechanistic approach to predicting the cutting forces in drilling: With application to fiber-reinforced composite materials. *Journal of Engineering for Industry*. 1995;117:559-70.
- [104] Caprino G, Nele L. Cutting forces in orthogonal cutting of unidirectional GFRP composites. *Journal of Engineering Materials and Technology*. 1996;118:419-25.
- [105] Caprino G, Santo L, Nele L. On the origin of cutting forces in machining unidirectional composite materials. *ASME International Reprinted from: PD*. 1996;75:83-9.

- [106] Langella A, Nele L, Maio A. A torque and thrust prediction model for drilling of composite materials. Composites Part A: Applied Science and Manufacturing. 2005;36:83-93.
- [107] Reza Vaziri Sereshk M, Mohammadi Bidhendi H. The Contribution of Different Fracture Modes on Drilling Delamination Crack Propagation. Journal of Manufacturing Science and Engineering. 2016;139:011013--8.
- [108] Saghizadeh H, Dharan CKH. Delamination fracture toughness of graphite and aramid epoxy composites. Journal of Engineering Materials and Technology. 1986;108:290-5.
- [109] ASTM D7137 / D7137M-12, Standard Test Method for Compressive Residual Strength Properties of Damaged Polymer Matrix Composite Plates, ASTM International, West Conshohocken, PA, 2012.,
- [110] Montgomery DC. Design and analysis of experiments. 1991.
- [111] Julong D. Introduction to grey system theory. The Journal of Grey System. 1989;1:1-24.
- [112] Goldsmith W, Dharan CKH, Chang H. Quasi-static and ballistic perforation of carbon fiber laminates. International Journal of Solids and Structures. 1995;32:89-103.
- [113] Govekar E, Gradišek J, Grabec I. Analysis of acoustic emission signals and monitoring of machining processes. Ultrasonics. 2000;38:598-603.
- [114] Guoqi Z, Goldsmith W, Dharan CKH. Penetration of laminated Kevlar by projectiles—I. Experimental investigation. International Journal of Solids and Structures. 1992;29:399-420.
- [115] Guoqi Z, Goldsmith W, Dharan C. Penetration of laminated Kevlar by projectiles—II. Analytical model. International Journal of Solids and Structures. 1992;29:421-36.
- [116] Enemuoh EU, El-Gizawy AS, Chukwujekwu Okafor A. An approach for development of damage-free drilling of carbon fiber reinforced thermosets. International Journal of Machine Tools and Manufacture. 2001;41:1795-814.
- [117] Mohan NS, Kulkarni SM, Ramachandra A. Delamination analysis in drilling process of glass fiber reinforced plastic (GFRP) composite materials. Journal of Materials Processing Technology. 2007;186:265-71.
- [118] Miller RK, McIntire P. Nondestructive testing handbook: Acoustic Emission Testing. American Society for Nondestructive Testing, 4153 Arlingate Plaza, Caller# 28518, Columbus, Ohio 43228, USA, 1987 603. 1987; Vol. 5.
- [119] Mordfin L. Handbook of reference data for nondestructive testing. ASTM; 2002.
- [120] ASTM E. 1316, Standard terminology for nondestructive examinations. Annual Book of ASTM Standards. 1997;3.
- [121] Holcomb DJ. General theory of the Kaiser effect. International Journal of Rock Mechanics and Mining Sciences & Geomechanics Abstracts: Elsevier; 1993. p. 929-35.
- [122] Rüsch H, Van Amerongen C. Physical problems in the testing of concrete: Cement and Concrete Association, 1960.
- [123] Robinson GS. Methods of detecting the formation and propagation of microcracks in concrete. 1968.
- [124] Wells D. An acoustic apparatus to record emissions from concrete under strain. Nuclear engineering and design. 1970;12:80-8.

- [125] Green A. Stress wave emission and fracture prestressed concrete reactor vessel materials. Aerojet-General Corp., Sacramento, Calif.; 1969.
- [126] Ravishankar SR, Murthy CRL. Application of acoustic emission in drilling of composite laminates. *NDT & E International*. 2000;33:429-35.
- [127] Ravishankar SR, Murthy CRL. Characteristics of AE signals obtained during drilling composite laminates. *NDT & E International*. 2000;33:341-8.
- [128] Velayudham A, Krishnamurthy R, Soundarapandian T. Acoustic emission based drill condition monitoring during drilling of glass/phenolic polymeric composite using wavelet packet transform. *Materials Science and Engineering: A*. 2005;412:141-5.
- [129] Godin N, Huguet S, Gaertner R, Salmon L. Clustering of acoustic emission signals collected during tensile tests on unidirectional glass/polyester composite using supervised and unsupervised classifiers. *NDT & E International*. 2004;37:253-64.
- [130] Godin N, Huguet S, Gaertner R. Integration of the Kohonen's self-organising map and k-means algorithm for the segmentation of the AE data collected during tensile tests on cross-ply composites. *NDT & E International*. 2005;38:299-309.
- [131] Huguet S, Godin N, Gaertner R, Salmon L, Villard D. Use of acoustic emission to identify damage modes in glass fibre reinforced polyester. *Composites Science and Technology*. 2002;62:1433-44.
- [132] Marec A, Thomas JH, El Guerjouma R. Damage characterization of polymer-based composite materials: Multivariable analysis and wavelet transform for clustering acoustic emission data. *Mechanical Systems and Signal Processing*. 2008;22:1441-64.
- [133] Pappas YZ, Markopoulos YP, Kostopoulos V. Failure mechanisms analysis of 2D carbon/carbon using acoustic emission monitoring. *NDT & E International*. 1998;31:157-63.
- [134] Philippidis T, Nikolaidis V, Anastassopoulos A. Damage characterization of carbon/carbon laminates using neural network techniques on AE signals. *NDT & E International*. 1998;31:329-40.
- [135] Bar H, Bhat M, Murthy C. Parametric analysis of acoustic emission signals for evaluating damage in composites using a PVDF film sensor. *Journal of Nondestructive Evaluation*. 2005;24:121-34.
- [136] Omkar SN, Karanth U R. Rule extraction for classification of acoustic emission signals using Ant Colony Optimisation. *Engineering Applications of Artificial Intelligence*. 2008;21:1381-8.
- [137] Moevus M, Godin N, R'Mili M, Rouby D, Reynaud P, Fantozzi G, et al. Analysis of damage mechanisms and associated acoustic emission in two SiCf/[Si-B-C] composites exhibiting different tensile behaviours. Part II: Unsupervised acoustic emission data clustering. *Composites Science and Technology*. 2008;68:1258-65.
- [138] Liu Q, Chen X, Gindy N. Fuzzy pattern recognition of AE signals for grinding burn. *International Journal of Machine Tools and Manufacture*. 2005;45:811-8.
- [139] Johnson M. Waveform based clustering and classification of AE transients in composite laminates using principal component analysis. *NDT & E International*. 2002;35:367-76.
- [140] Kostopoulos V, Loutas T, Kontsos A, Sotiriadis G, Pappas Y. On the identification of the failure mechanisms in oxide/oxide composites using acoustic emission. *NDT & E International*. 2003;36:571-80.

- [141] Loutas TH, Kostopoulos V. Health monitoring of carbon/carbon, woven reinforced composites. Damage assessment by using advanced signal processing techniques. Part I: Acoustic emission monitoring and damage mechanisms evolution. Composites Science and Technology. 2009;69:265-72.
- [142] Bezdek JC, Ehrlich R, Full W. FCM: The fuzzy c-means clustering algorithm. Computers & Geosciences. 1984;10:191-203.
- [143] Refahi Oskouei A, Heidary H, Ahmadi M, Farajpur M. Unsupervised acoustic emission data clustering for the analysis of damage mechanisms in glass/polyester composites. Materials & Design. 2012;37:416-22.
- [144] Bezdek JC. Pattern recognition with fuzzy objective function algorithms: Kluwer Academic Publishers, 1981.
- [145] Dunn JC. A fuzzy relative of the ISODATA process and its use in detecting compact well-separated clusters. 1973.
- [146] Jolliffe I. Principal component analysis: Wiley Online Library, 2005.
- [147] Oja E. Neural networks, principal components, and subspaces. International journal of neural systems. 1989;1:61-8.
- [148] Barré S, Benzeggagh ML. On the use of acoustic emission to investigate damage mechanisms in glass-fibre-reinforced polypropylene. Composites Science and Technology. 1994;52:369-76.
- [149] Calabro A, Esposito C, Lizza A, Giordano M, D'amore A, Nicolais L. Analysis of the acoustic emission signals associated to failure modes in CFRP laminates. ECCM-8 European Conference on Composite Materials: Science, Technologies and Applications, 3-6 June 1998, Naples: Woodhead Publishing; 1998. p. 425.
- [150] Zarif Karimi N, Heidary H, Minak G, Ahmadi M. Effect of the drilling process on the compression behavior of glass/epoxy laminates. Composite Structures. 2013;98:59-68.
- [151] de Oliveira R, Marques AT. Health monitoring of FRP using acoustic emission and artificial neural networks. Computers & Structures. 2008;86:367-73.
- [152] El Guerjouma R, Baboux J-C, Ducret D, Godin N, Guy P, Huguet S, et al. Non-destructive evaluation of damage and failure of fibre reinforced polymer composites using ultrasonic waves and acoustic emission. Advanced engineering materials. 2001;3.
- [153] Graps A. An introduction to wavelets. Computational Science & Engineering, IEEE. 1995;2:50-61.
- [154] Stark H-G. Wavelets and signal processing: Springer, 2005.
- [155] Zhu G, Goldsmith W, Dharan C. Penetration of laminated Kevlar by projectiles. II: Analytical model. International Journal of Solids and Structures. 1992;29:421-36.
- [156] Lee SR, Sun C. A quasi-static penetration model for composite laminates. Journal of composite materials. 1993;27:251-71.
- [157] Heidary H, Karimi NZ, Ahmadi M, Rahimi A, Zucchelli A. Clustering of acoustic emission signals collected during drilling process of composite materials using unsupervised classifiers. Journal of composite materials. 2014;0021998314521258.
- [158] Bohse J. Acoustic emission characteristics of micro-failure processes in polymer blends and composites. Composites Science and Technology. 2000;60:1213-26.

- [159] Loutas T, Kostopoulos V, Ramirez-Jimenez C, Pharaoh M. Damage evolution in center-holed glass/polyester composites under quasi-static loading using time/frequency analysis of acoustic emission monitored waveforms. Composites Science and Technology. 2006;66:1366-75.
- [160] Suzuki M, Nakanishi H, Iwamoto M, Jinen E. Application of static fracture mechanisms to fatigue fracture behavior of class A-SMC composite. Japan-U S Conference on Composite Materials, 4 th, Washington, DC1989. p. 297-306.
- [161] de Groot PJ, Wijnen PAM, Janssen RBF. Real-time frequency determination of acoustic emission for different fracture mechanisms in carbon/epoxy composites. Composites Science and Technology. 1995;55:405-12.

# List of Publications

## International Journals

1. H. Heidary, **N. Zarif Karimi**, G. Minak, Investigation on delamination and flexural properties in drilling of carbon nanotube/polymer composites, under review.
2. **N. Zarif Karimi**, H. Heidary, J. Yousefi, S. Sadeghi, G. Minak, Experimental investigation on delamination in nanocomposite drilling, *FME Transactions* (2018) 46, 62-69.
3. **N. Zarif Karimi**, H. Heidary, M. Fotouhi, G. Minak, Experimental analysis of GFRP laminates subjected to compression after drilling, *Journal of Composite Materials*, 169 (2017) 144-152.
4. Mahdian, J. Yousefi, M. Nazmdar, **N. Zarif Karimi**, M. Ahmadi, G. Minak, Damage evaluation of laminated composites under low-velocity impact tests using acoustic emission method, *Journal of Composite Materials*, 51 (2017) 479-490.
5. **N. Zarif Karimi**, H. Heidary, G. Minak, Critical thrust and feed prediction models in drilling of composite laminates, *Composite Structures*, 148 (2016) 19-26.
6. **N. Zarif Karimi**, H. Heidary, P. Kianfar, M. Hasani, G. Minak, The effect of support plate on drilling-induced delamination, *Acta Polytechnica CTU Proceedings*, 3 (2016) 19-24.
7. **N. Zarif Karimi**, G. Minak, P. Kianfar, Analysis of damage mechanisms in drilling of composite materials by acoustic emission, *Composite Structures*, 131 (2015) 107-114.

## Conferences

1. **N. Zarif Karimi**, M. Fotouhi, H. Hosseini, G. Minak, Effect of hole machining damages on bending strength of composite laminates, 20th International Conference on Composite Structures (ICCS20), Paris, France, 2017.
2. M. Saeedifar, H. Saghfai, **N. Zarif Karimi**, H. Hosseini, M. Ahmadi, G. Minak, Investigation of the effects of loading rate on interlaminar fracture toughness of fiber metal laminates using acoustic emission, 20th International Conference on Composite Structures (ICCS20), Paris, France, 2017.
3. **N. Zarif Karimi**, G. Minak, A thrust and feed prediction model for drilling of composite materials, 3rd International Conference on Mechanics of Composites (MECHCOMP3), Bologna, Italy, 2017.
4. J. Yousefi, **N. Zarif Karimi**, M. Ahmadi, G. Minak, Evaluation of mode II delamination growth using a new acoustic emission Lamb-based technique, 3rd International Conference on Mechanics of Composites (MECHCOMP3), Bologna, Italy, 4-7 July 2017.
5. **N. Zarif Karimi**, G. Minak, Multiple performance optimization of machining parameters in drilling of CNT-based fiber reinforced composites, Convegno AIAS, Pisa, Italy, 2017.
6. **N. Zarif Karimi**, G. Minak, Analytical analysis of drilling-associated damage in composites, IX Triennial International Conference Heavy Machinery (HM 2017), Zlatibor, Serbia, 2017.

7. **N. Zarif Karimi**, G. Minak, S. Sadeghi, M. Ahmadi, Residual compressive strength of drilled glass fiber reinforced Composites, 2nd International Conference on Mechanics of Composites, Porto, Portugal, 2016.
8. M. Saeedifar, M. Fotouhi, **N. Zarif Karimi**, M. Ahmadi, H. Hosseini, G. Minak, Prediction of delamination growth in glass/epoxy composites using acoustic emission, 2nd International Conference on Mechanics of Composites, Porto, Portugal, 2016.
9. Mahdian, J. Yousefi, **N. Zarif Karimi**, G. Minak, Damage extension characterization of low velocity impacted plate using acoustic emission, 2nd International Conference on Mechanics of Composites, Porto, Portugal, 2016.
10. **N. Zarif Karimi**, H. Heidary, J. Yousefi, G. Minak, An analytical model for predicting critical feed rate in drilling of composite laminates, 17th European Conference on Composite Materials (ECCM17), Munich, Germany, 2016.
11. **N. Zarif Karimi**, H. Heidary, J. Yousefi, G. Minak, Experimental investigation on delamination in nanocomposite drilling, 15th Youth Symposium on Experimental Solid Mechanics (YSESM) Rimini, Italy, 2016.
12. S. Sadeghi, M. Fotouhi, **N. Zarif Karimi**, M. Ahmadi, G. Minak, Residual stress evaluation in friction stir welding of aluminum plates by means of acoustic emission and ultrasonic waves, 15th Youth Symposium on Experimental Solid Mechanics (YSESM), Rimini, Italy, 2016.
13. H. Heidary, M. Sadri, **N. Zarif Karimi**, F. Zandi, G. Minak, Numerical study of plasticity effects in uniform residual stresses measurement by ring-core technique, 15th Youth Symposium on Experimental Solid Mechanics (YSESM), Rimini, Italy, 2016.
14. **N. Zarif Karimi**, P. Kianfar, H. Heidary, G. Minak, The effect of chisel edge on drilling-induced delamination, 18th International Conference on Composite Structures (ICCS18), Lisbon, Portugal, 2015.
15. **N. Zarif Karimi**, P. Kianfar, G. Minak, Analysis of damage mechanisms in drilling of composite materials by acoustic emission, 18th International Conference on Composite Structures (ICCS18), Lisbon, Portugal, 2015.
16. **N. Zarif Karimi**, M. Fotouhi, M. Saeedifar, G. Minak, M. Ahmadi, Inter-laminar fracture toughness measurement of the mixed-mode delamination using acoustic emission technique, 18th International Conference on Composite Structures (ICCS18), Lisbon, Portugal, 2015.
17. **N. Zarif Karimi**, H. Heidary, P. Kianfar, G. Minak, The effect support plate on drilling-induced delamination, 14th Youth Symposium on Experimental Solid Mechanics (YSESM), Traunkirchen Monastery, Austria, 2015.
18. **N. Zarif Karimi**, P. Kianfar, G. Minak, Delamination analysis of laminated composite in drilling and quasi-static penetration, 20th International Conference on Composite Materials (ICCM20), Copenhagen, Denmark, 2015.

## Appendix A: Calculating reduced bending stiffness matrix

1. Calculate reduced stiffness matrix  $Q_{ij}$  for each material used in the laminate (if a laminate uses only one type of composite material, there will be only one stiffness matrix). The stiffness matrix describes the elastic behavior of the ply in plane loading:

$$Q_{ij} = \begin{bmatrix} Q_{11} & Q_{12} & 0 \\ Q_{12} & Q_{22} & 0 \\ 0 & 0 & Q_{66} \end{bmatrix} \quad i,j = 1,2,6$$

where

$$\begin{aligned} Q_{11} &= \frac{E_{11}^2}{(E_{11} - v_{12} \cdot E_{22})}, & Q_{12} &= \frac{v_{12} E_{11} E_{22}}{E_{11} - v_{12}^2 \cdot E_{22}} \\ Q_{22} &= \frac{E_{11} E_{22}}{E_{11} - v_{12}^2 \cdot E_{22}}, & Q_{66} &= G_{12} \end{aligned}$$

2. Calculate the transformed reduced stiffness matrix  $\bar{Q}_{ij}$  for each ply based on the reduced stiffness matrix and fiber angle.

$$Q_{ij} = \begin{bmatrix} \bar{Q}_{11} & \bar{Q}_{12} & \bar{Q}_{16} \\ \bar{Q}_{12} & \bar{Q}_{22} & \bar{Q}_{26} \\ \bar{Q}_{16} & \bar{Q}_{26} & \bar{Q}_{66} \end{bmatrix} \quad i,j = 1,2,6$$

where:

$$\begin{aligned} \bar{Q}_{11} &= Q_{11} \cos^4 \theta + 2(Q_{12} + 2Q_{66}) \cos^2 \theta \sin^2 \theta + Q_{22} \sin^4 \theta \\ \bar{Q}_{12} &= \bar{Q}_{21} = Q_{12}(\cos^4 \theta + \sin^4 \theta) + (Q_{11} + Q_{22} - 4Q_{66}) \cos^2 \theta \sin^2 \theta \\ \bar{Q}_{16} &= \bar{Q}_{61} = (Q_{11} - Q_{12} - 2Q_{66}) \cos^3 \theta \sin \theta - (Q_{22} - Q_{12} - 2Q_{66}) \cos \theta \sin^3 \theta \\ \bar{Q}_{22} &= Q_{11} \sin^4 \theta + 2(Q_{12} + 2Q_{66}) \cos^2 \theta \sin^2 \theta + Q_{22} \cos^4 \theta \\ \bar{Q}_{26} &= \bar{Q}_{62} = (Q_{11} - Q_{12} - 2Q_{66}) \cos \theta \sin^3 \theta - (Q_{22} - Q_{12} - 2Q_{66}) \cos^3 \theta \sin \theta \\ \bar{Q}_{66} &= (Q_{11} + Q_{22} - 2Q_{12} - 2Q_{66}) \cos^2 \theta \sin^2 \theta + Q_{66}(\cos^4 \theta + \sin^4 \theta) \end{aligned}$$

3. Calculate the reduced bending stiffness matrix:

$$D_{ij} = \sum_{k=1}^n (\bar{Q}_{ij})_k \frac{(h_k^3 - h_{k-1}^3)}{3}, \quad i,j = 1,2,6$$

For an orthotropic plate:

$$\begin{bmatrix} D_{11} & D_{12} & D_{16} \\ D_{12} & D_{22} & D_{26} \\ D_{16} & D_{26} & D_{66} \end{bmatrix} = \frac{h^3}{12(1 - v_{12}v_{21})} \begin{bmatrix} E_1 & v_{12}E_2 & 0 \\ v_{21}E_1 & E_2 & 0 \\ 0 & 0 & 2G_{12}(1 - v_{12}v_{21}) \end{bmatrix}$$

## Appendix B: Solution of the governing equation for circular plates

### 1. Clamped circular plate under central point load

In any particular case of a symmetrically loaded circular plate the shearing force  $Q_r$  can be used to determine the deflection of the plate using the following expression:

$$\frac{d}{dr} \left[ \frac{1}{r} \frac{d}{dr} \left( r \frac{dw}{dr} \right) \right] = -\frac{Q_r}{D}$$

For this case, dividing the plate into two parts as shown in Figure 1, it can be seen that the inner portion of the plate is in the condition of pure bending produced by the uniformly distributed moments  $M$  and that the outer part is bent by the moments  $M$  and the shearing forces  $Q_r$ . Denoting by  $P$  the total load applied, we find that:

$$Q_r = -\frac{P}{2\pi r}$$

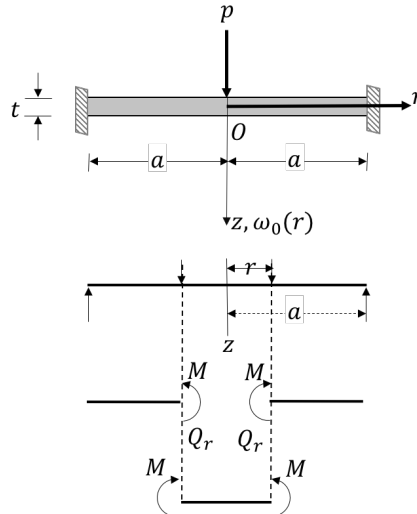


Figure 1. Clamped circular plate under central point load.

Substituting this in the above equation and after three integration, we obtain:

$$w = \frac{P}{8\pi D} (r^2 \ln r - r^2) + c_1 \frac{r^2}{4} + c_2 \ln r + c_3$$

The support conditions are:

1. At  $r = 0$ ,  $w \neq \infty$ , so  $c_2 = 0$
2. At  $r = a$ ,  $\frac{dw}{dr} = 0$ , so  $c_1 = \frac{P}{4\pi D} (1 - 2 \ln a)$
3. At  $r = a$ ,  $w = 0$ , so  $c_3 = \frac{Pa^2}{16\pi D}$

Hence, the solution becomes:

$$w = w(r) = \frac{P}{16\pi D} \left[ 2r^2 \ln \left( \frac{r}{a} \right) + (a^2 - r^2) \right], \quad r \neq 0$$

and the maximum deflection occurring at the center of the plate ( $r = 0$ ) is then:

$$w_{max} = \frac{Pa^2}{16\pi D}$$

## 2. Clamped circular plate under uniformly distributed load

For this case, dividing the plate into two parts as shown in Figure 2, the magnitude of the shearing forces at a distance  $r$  from the center of the plate is determined from the equation:

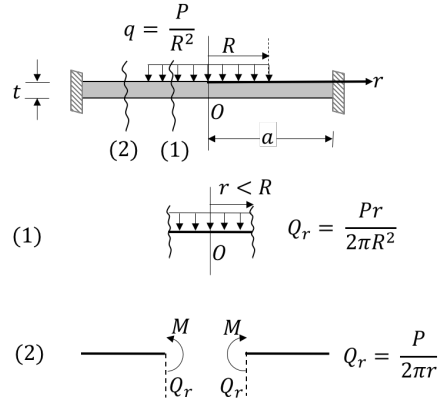


Figure 2. Clamped circular plate under uniformly distributed load

$$2\pi r Q_{r1} = -\pi r^2 \frac{P}{\pi R^2}$$

$$2\pi r Q_{r2} = -P$$

from which:

$$Q_{r1} = -\frac{Pr}{2\pi R^2}$$

$$Q_{r2} = -\frac{P}{2\pi r}$$

Where  $P = qa^2$  denotes the total load applied to the inner boundary of the plate.

Substituting these in  $\frac{d}{dr} \left[ \frac{1}{r} \frac{d}{dr} \left( r \frac{dw}{dr} \right) \right] = \frac{Q_r}{D}$  and integrating, we obtain:

$$w_1 = \frac{Pr^4}{64\pi R^2 D} + c_1 \frac{r^2}{4} + c_2 \ln r + c_3$$

$$w_2 = \frac{P}{8\pi D} (r^2 \ln r - r^2) + \frac{c_4}{4} r^2 + c_5 \ln r + c_6$$

The boundary conditions are:

1. At  $r = 0$ ,  $w_1 \neq \infty$ , so  $c_2 = 0$

$$2. \text{ At } r = a, \frac{dw_2}{dr} = 0 \quad \text{so } \frac{Pa^2}{8\pi D} (2 \ln a - 1) + c_4 \frac{a^2}{2} + c_5 = 0$$

$$3. \text{ At } r = a, w_2 = 0 \quad \text{so } \frac{Pa^2}{8\pi D} (2 \ln a - 1) + c_4 \frac{a^2}{4} + c_5 \ln a + c_6 = 0$$

$$4. \text{ At } r = R, w_2 = w_1$$

$$5. \text{ At } r = R, \frac{dw_2}{dr} = \frac{dw_1}{dr}$$

$$6. \text{ At } r = R, M_{r2} = M_{r1}, Q_{r2} = Q_{r1}$$

$$c_1 = \frac{P}{8\pi D} \left( 4 \ln \frac{R}{a} - \frac{R^2}{a^2} \right)$$

$$c_2 = 0$$

$$c_3 = \frac{Pa^2}{64\pi D} \left( 4 - 3 \frac{R^2}{a^2} + 4 \frac{R^2}{a^2} \ln \frac{R}{a} \right)$$

$$c_4 = -\frac{P}{8\pi D} \left( 6 + \frac{R^2}{a^2} \right)$$

$$c_5 = \frac{PR^2}{16\pi D}$$

$$c_6 = \frac{Pa^2}{32\pi D} \left( 2 - 2 \ln a + \frac{R^2}{a^2} \right)$$

Hence, the solution becomes:

$$w_1 = \frac{P}{64\pi D} \left[ \left( 4a^2 - 3R^2 + 4R^2 \ln \left( \frac{R}{a} \right) \right) - 2r^2 \left( \frac{R^2}{a^2} - 4 \ln \left( \frac{R}{a} \right) \right) + \frac{r^4}{R^2} \right]$$

$$w_2 = \frac{P}{32\pi D} \left[ (2a^2 + R^2) - r^2 \left( 2 + \frac{R^2}{a^2} - 4 \ln \left( \frac{r}{a} \right) \right) + 2R^2 \ln \left( \frac{r}{a} \right) \right]$$

